UNIVERSITAT POLITÈCNICA
DE CATALUNYA
BARCELONATECH

Control of power converter in modern power systems

Ngoc Bao Lai

PhD Thesis

Control of Power Converter in Modern Power Systems

Ngoc Bao Lai

Barcelona, February 2022

Control of Power Converter in Modern Power Systems

Ngoc Bao Lai

Dissertation submitted to the Doctorate Office of the Universitat Politècnica de Catalunya in partial fulfilment of the requirements for the degree of Doctor of Philosophy by the

UNIVERSIDAD DE MÁLAGA

UNIVERSIDAD DE SEVILLA

UNIVERSIDAD DEL PAÍS VASCO/EUSKAL ERRIKO UNIBERTSITATEA

UNIVERSITAT POLITÈCNICA DE CATALUNYA

Joint Doctoral Programme in

Electric Energy Systems

Barcelona, February 2022

Control of Power Converter in Modern Power Systems

Printed by the UPC
Barcelona, February 2022

ISBN:–.
Research Project: This work was supported in part by the European Commission under Project FLEXITRANSTORE-H2020-LCE-2016-2017-SGS-774407.

UNIVERSITAT POLITÈCNICA DE CATALUNYA
Escola de Doctorat
Edifici Vertex. Pl. Eusebi Güell, 6
08034 Barcelona.
Web: http://www.upc.edu

UNIVERSIDAD DE MALAGA
Escuela de Doctorado
Pabellón de Gobierno - Plaza el Ejido s/n
(29013) Málaga.
Web: http://www.uma.es

UNIVERSIDAD DE SEVILLA
Escuela Internacional de Doctorado
Pabellón de México - Paseo de las Delicias, s/n
41013 Sevilla.
Web: http://www.us.es

UNIVERSIDAD DEL PAÍS VASCO/EUSKAL ERRIKO UNIBERTSITATEA
Escuela de Master y Doctorado
Edificio Aulario II - Barrio Sarriena, s/n
48940- Leioa (Bizkaia) Spain.
Web: http://www.ehu.eus/es

To my wife Quyen

and my little son Bach

ACKNOWLEDGEMENTS

I would like first to thank my supervisor, Prof. Pedro Rodriguez, for the continuous support and guidance during my PhD studies. His inspiration and feedback push my research to a higher level. I am deeply grateful for the opportunities he provided to work on cutting-edge projects with a highly-skilled team.

My sincere thanks also go to Dr Alvaro Luna, Dr Joan Rocabert, and Dr Ignacio Candela for helping me with many aspects during the last 4 years from solving technical problems to administration.

I am also grateful for the collaboration with my talented colleagues and friends, Dr Nicolas-Gregory Baltas, Andres Tarraso, and Leonardo Marin. The research conducted in this PhD thesis would not be possible without your support in modelling and experiments.

I would also like to thank my colleagues at LUA, UPC, and LIST, especially Dr Carlos Sabillón, Isabel Moriña, David Cambronero, and Borja Garcia for their kind support in project tasks, lab work, and administrative issues.

I would also like to thank the Universidad Loyola and Luxembourg Institute of Science and Technology (LIST) for hosting my stays during my PhD studies.

I would also like to thank the European Commission for financially supporting my studies through the H2020 FlexiTranstore project.

Last but not least, I would like to thank my family: my parents and brother for always being there for me, my wife and son for their understanding and spiritual support throughout this challenging journey.

Ngoc Bao Lai
Barcelona, Spain
February 2022

Abstract

Power system is undergoing an unpreceded paradigm shift: from centralized to distributed generation. Conventionally, the control and regulation of power systems depend solely on some large-scale generations. As the renewable-based generations and battery storage systems are increasingly displacing conventional generations, it becomes more and more difficult to maintain the stability and reliability of the grid by using only conventional generation units. There has been growing concerns about the potential instability-driven blackouts in power systems dominated by renewable sources. Such concerns have become even more pressing after the infamous renewable-related cascading failures in the electrical networks of South Australia, Great Britain, and the United State. In addition to the considerable financial loss, millions of people were put into darkness.

One of the main factors contributing to the degradation of grid stability is the rapid penetration of renewable energy and storage systems. These new generations interface with the grids mainly through power electronics converters or power converters for short. Conventionally, power converters are designed to maximize conversion efficiency and resource utilization. In fact, tracking maximum power points has been the ultimate objective of most PV plants and wind farms. Consequently, power converters only focus on their internal operation despite the grid conditions. Actually, power converters may even worsen the grid operation during transient events. This design philosophy was preferable in the past because the share of renewables in the total generation was considerably low such that their impact on the grid was unnoticeable. However, as renewables are currently supplying more than half of the total demand in many power networks during certain periods, such a self-centric operation of power converters are undesirable.

To remedy such a situation, the grid-forming (GFM) concept has been proposed for power converters to replace the conventional control strategies which are often referred to as grid-following (GFL) control. The GFM concept aims to redesign the control system of the power converter to enforce more grid-friendly behaviours. In addition to the basic

functionalities required to deal with electromagnetic issues such as harmonic compensation and unbalanced voltage among others, GFM converters also offer grid-supporting capabilities such as inertia response, power oscillation damping, and islanding operation to name a few. Despite the rich literature on GFM implementations, the actual adaptation of GFM control in real-world applications is still rare. The main reasons for such a reluctance by the industry are twofold: firstly, incentives for renewable power plants to provide services based on such advanced grid-forming functions were at best scarce. In the last years, however, several system operators have imposed new requirements and markets for grid-supporting services such as fast frequency reserves which require inertial response from power converters. Secondly, the current GFM implementation required modification to low-level control firmware of power converter in mass scale. This requirement is, in many cases, unrealistic due to the hardware control limitations in existing systems, as well as the additional testing and certification such modification entails.

This PhD thesis aims to bridge the research gaps in the control and implementation of GFM converter. That is, the thesis focuses on three main aspects: (i) improving internal stability of the GFM converter via robust control techniques to ensure the system stability for a wider range of grid perturbation, (ii) implementation of GFM converter through communication such that modification of power converter firmware can be avoided, (iii) extending the capability of GFM converter to enhance the small-signal stability of power systems with low damping.

While the power controllers are often designed towards supporting the grid, the current controller is, on the other hand, responsible for the internal workings of the power converter. To ensure a stable operation of the GFM converter under adverse operating conditions, a robust voltage sensorless current (RVSC) controller is developed in this PhD thesis. Unlike the existing controllers, the RVSC is able to handle simultaneously most of the possible abnormal conditions of the grid such as impedance variations, unbalanced voltage, harmonics distortion. These undesired operating conditions of the grid are mathematically represented using equivalent linear models such that they can be used for calculating the controller gains. Linear matrix inequality (LMI) techniques are also used to facilitate parameter tuning. In fact, the performance and stability of the current control loop can be determined through only 2 tuning parameters instead of 8 parameters for a controller of a similar structure.

The existing GFM implementations are designed under the consideration that the digital controller of the power converter can be easily upgraded at will. This is true in the case of smart power converters where more and more new functions are being incorporated. These types of power converters are still under development and not yet cost-competitive. Indeed,

most power converters employed in renewable power plants and storage systems are equipped with GFL control schemes and produced in mass quantities. As a result, modification of the control firmware is not straightforward and cost-effective considering the enormous number of existing converters. To overcome such a limitation, an external synchronous controller (ESC) will be presented in this PhD thesis. The ESC uses measurements such as frequency and power, which are either provided by the power converter or a dedicated measurement unit, to calculate the actual active and reactive power that should be injected by the power converters in a way that the power plant acts as an aggregated GFM converter. By doing so, any conventional power converter, equipped with an available fast-fieldbus communication, can be utilized for providing grid-supporting services with minimal modification to the existing infrastructure.

Evidently, most of the GFM strategies have not yet fully exploited the potential of power converters. In fact, most of the GFM implementations only focus on mimicking exactly the operation of a synchronous generator (SG). However, it is worth pointing out that power converters can provide even better performance if a proper control scheme is used. In this regard, the final chapter of this PhD thesis presents the multi-rotor virtual machine (MRVM) implementation for GFM converter to boost the performance of power converters in damping power oscillations. The MRVM implements several virtual rotors instead of only one rotor as in typical GFM strategies. Since each of the virtual rotors is tuned to target a specific critical mode, the damping participation to such a mode can be increased and adjusted individually. As a result, the MRVM-GFM can damp multiple modes simultaneously in a controlled manner.

The controllers presented in this PhD thesis are validated through simulations and experiments. The experimental results come from laboratory prototypes as well as actual demonstrations of the H2020 FlexiTranstore project. The results are throughout analysed to assess the control performance as well as to highlight possible implications.

CONTENTS

FIGURES

TABLES

Nomenclature

CVCC	Cascaded voltage-current controller
eIEC	External inertia emulation controller
ENTSO-E	European Network of Transmission System Operators for Electricity
ESC	External synchronous controller
GCC	Grid-connected converter
GFL	Grid-following
GFM	Grid-forming
MRVM	Multi-rotor virtual machine
NREL	National Renewable Energy Laboratory
PCC	Point of common coupling
PI	Proportional integral
PLC	Power loop controller
PLL	Phase-locked loop
PSL	Power synchronization loop
RVSC	Robust voltage-sensorless controller
SG	Synchronous generator
SPC	Synchronous power controller
SRF	Synchronous reference frame
VISMA	Virtual synchronous machine
VSG	Virtual synchronous generator
VSM	Virtual synchronous machine

CHAPTER 1.

Introduction

This chapter introduces the overview of the dissertation. In particular, Section 1.1 reviews the development trends in the control of power converters with a special focus on power system stability under the presence of abundant non-synchronous generations. Section 1.2 formulate the problems in the control of power converters in modern power systems. Section 1.3 presents the research objectives of this PhD thesis. Then, Section 1.4 shows the organization of this PhD thesis. Finally, Section 1.5 summarizes the publications which report the findings and results of the research works conducted in this PhD project.

1.1 Background

The power system landscape has been undergoing profound transformations over the last decade. That is, power generation is shifting from centralised systems relying on a few large-scale power plants towards mixed systems with a large number of distributed generations of various sizes. Such structural changes have brought about paramount benefits to the environment such as the reduction of carbon dioxide emitted by fossil-based power plants, helping many nations to reach their environmental targets. On a global scale, such paradigm shift is consistent with energy plans set out following the Paris Agreement [1].

The vast majority of the newly integrated generations are based on power electronic converters of some forms. Despite the difference in their internal energy conversion structure, power converters are usually connected to the grid through a voltage source converter which is controlled by a digital controller. The control system of these grid-connected converters also varied based on the applications. Yet, their common objective is

to maximize energy conversion efficiency. This common objective has been in fact forcefully followed to a point that the grid-connected power converters do not consider the stability of the grid but only their internal operations.

With the number of conventional generations being replaced by distributed ones increasing significantly over the last years, the structure of power systems has also changed considerably. One of the most serious concerns posed by the power converters is the stability of power systems. Indeed, the stability of the power system has been redefined recently to take into account the impact of converter-based resources [2]. Most relevantly, a new classification of power system stability, shown in Fig. 1.1, has been jointly proposed by the IEEE Power System Dynamic Performance Committee and the CIGRE Study Committee 38 [2]. This new classification emphasizes on the inclusion of the impact introduced by power converters on the power system dynamics. In fact, as compared to the preceding classifications [3], two new stability categories have been added, which are resonance stability and converter-driven stability.

As its name suggests, converter-driven stability represents a phenomenon where instabilities are caused by the internal control system of the power converter or the interactions between power converters and other system components. According to the frequency spectrum, converter-driven instabilities fall into two groups, namely, fast interaction and slow interactions. The former case often ranges from hundreds of hertz to several kilohertz [4]. In many cases, this type of instability is associated with the resonances caused by the LCL filter which is used to mitigate the switching harmonics. Interactions among power converters operating in parallel have also been reported [5]. Such high-frequency resonances can be mitigated by either using passive resistors or active damping control techniques [6].

Similarly, slow-interaction instability refers to resonances in the range of sub-synchronous frequencies. This type of resonance is often caused by the interactions between the gird synchronization system, usually a phase-locked loop (PLL), and other system components. In many situations, slow-interaction instability couples with electromechanical and electromagnetic dynamics of the power system leading to instability in a wide range of frequencies [4]. Slow-interaction instability usually appears in weak networks where the power converter is connected to the grid through a considerable large impedance. This is because the voltage at the point of connection varies more significantly during an event, making the PLL unable to track the grid voltage properly. In recent years, several control strategies, which do not require the use of PLL for synchronization, have been proposed for power converters to improve the grid stability [7].

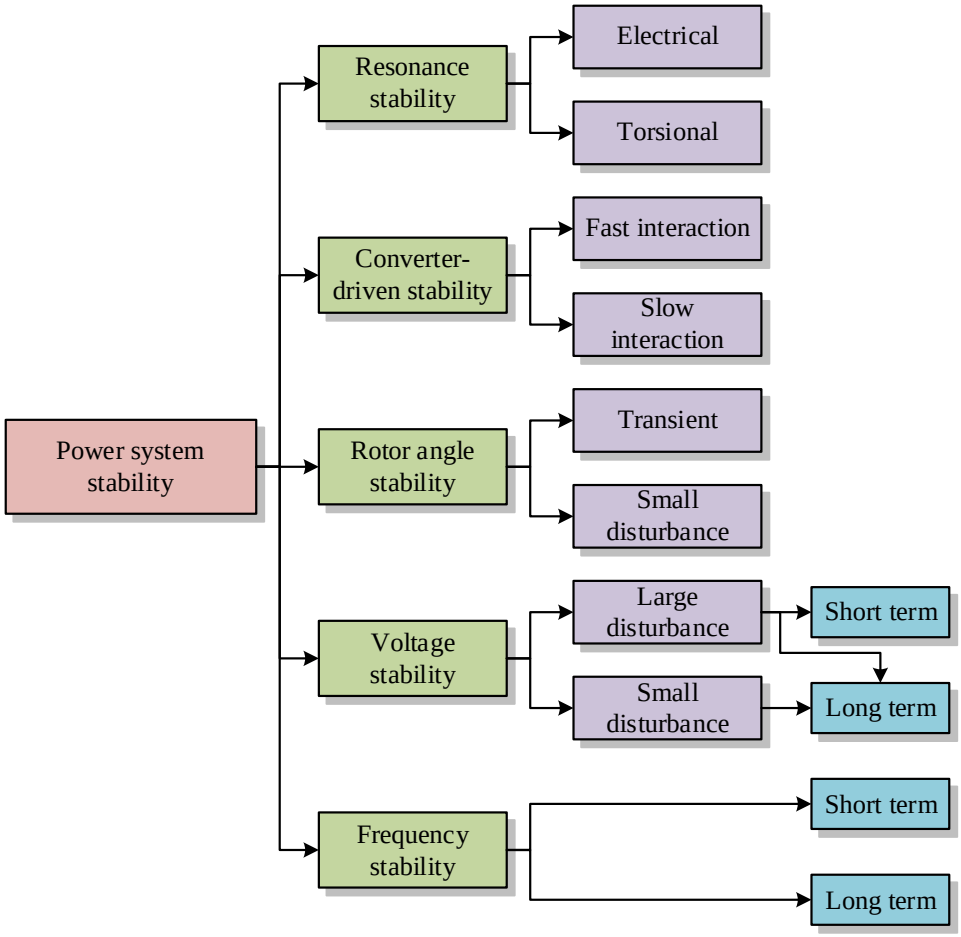

Fig. 1.1. Classification of power system stability [2].

Power converters also have a significant impact on the other stability categories. As discussed in recent publications and grid codes, grid frequency is strongly influenced by power converters. In fact, power converters deteriorate the frequency stability of power systems. This is mainly because power converters inherently do not provide inertia response as in the case of synchronous generators. Therefore, as the power converter displaces conventional generations, the net inertia of the grid decreases accordingly. As a result, frequency excursions become more aggressive with higher values of ROCOF and frequency nadir. Several studies suggest that frequency stability can be retained by de-loading continental generators instead of decommissioning them entirely [8]. A more efficient approach is to take advantage of the fast dynamics of the power converter in order to implement synthetic inertia [9].

Power converters do not traditionally provide either inertia or damping, thus rotor angle stability of power systems is also negatively affected. That is, due to the increasing deployment of renewables, the power flow of the tie-lines is greatly altered leading to undesired changes in interarea modes, stability margin, and damping [10]. More critically, displacing conventional generation equipped with power system stabilizers degrades significantly the stability margin of the system. In fact, it has been suggested that supplementary control should be provided by a power converter through synthetic damping; like the damping control provided by FACTS devices [11].

Numerous incidents in which there is a clear contribution of renewable resources to the cascading failures have been reported around the world. For instance, the infamous blackout in the South Australia network on 28th September 2016 affected nearly 1.7 million people and caused more than 229 million euros in financial loss [12]. A similar event took place on the 9th August 2019 in the Great Britain network affecting 1 million customers and costing system operators approximately 10 million euros [13]. Even though there are multiple causes of such blackouts, the link of power converter-based generations to such an event is undeniable. Indeed, in the former case, PV and wind generations account for around 50% of the total demand in the system.

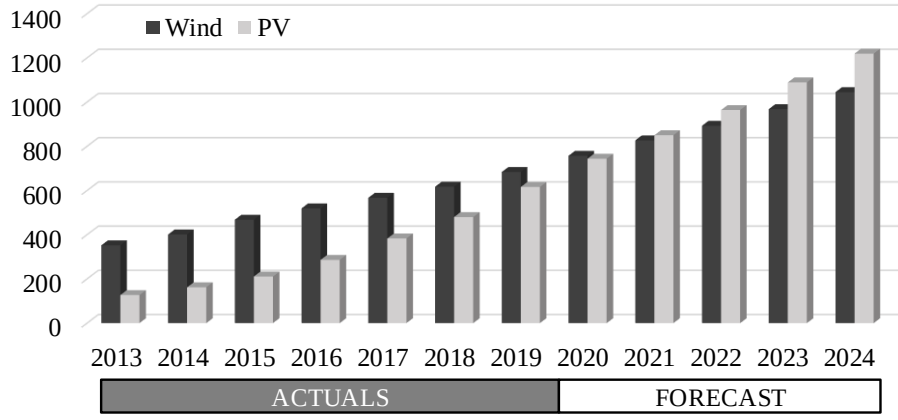

Fig. 1.2. Global cumulative installations for PV and wind power in GW. Source: IEA.

To achieve the environmental targets, incentives of various forms have been promoted by governments in order to increase the share of renewable generations in the total supply. This has further boosted the ever-increasing installation of renewable plants worldwide [14]. As shown in Fig. 1.2, deployment of PV and Wind power has increased steadily with annual additions of around 30% and 10% respectively. It is estimated that the total installation of PV and Wind power will reach 2264 GW by 2024 [15]. Furthermore, due to

the recent advances and cost reduction in battery energy storage systems (BESS), the installation of BESS is expected to increase exponentially in the coming years, as shown in Fig. 1.3. As a result, the presence of power converters in power systems will continue to increase significantly in the coming years.

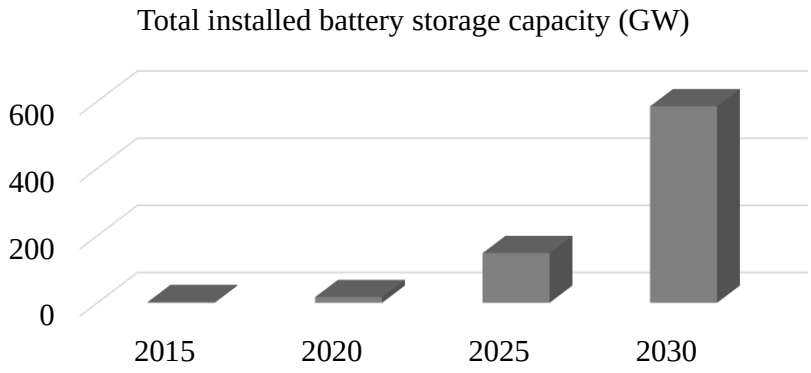

Fig. 1.3. Total installed battery storage capacity in the Net Zero Scenario. Source: IEA.

1.2 Problem Formulation

For accommodating such a high penetration of renewables, more advanced functionalities are required from grid-connected power converters. In this regard, ENTSO-E outlined a series of guidelines and preliminary technical requirements for grid-forming functions [16]. This technical report highlights the need for GFM converters in renewable-rich power systems. Notably, technical specifications for grid-forming functions such as creating system voltages, fault current contribution, and synthetic inertia among others are detailed. Similarly, NREL also published a research roadmap summarizing the importance as well as the technical challenges in deploying GFM converters [17].

In fact, the concept of GFM converter was proposed more than a decade ago [18] for AC microgrids. Initially, the main objective for grid-forming converters is to maintain a stable voltage after both intended and unintended islanding. To do so, this very first generation of GFM converter is designed to control the power converter as an ideal voltage source during an islanding event. In the islanded operation, the GFM converter regulates the grid voltage and frequency to reach reference values. To operate in parallel with the grid or other converters, droop control is often used as an outer loop for the voltage control loop. Since communications are not needed for the droop implementation, this control method is widely used in microgrids [19].

Even though the droop control strategies can guarantee a reasonable power-sharing among power converters while providing frequency and voltage support for the grid in the steady-state, this control approach does not provide any tangible support to the grid during transitoriness. To remedy such a drawback, new implementations based on the concept of a virtual synchronous machine (VSM) have been adopted for grid-forming converters [20]. Essentially, this type of grid-forming converter reacts to the grid disturbances in the same way as a synchronous machine would, for instance, inertia response. To do so, VSM-based GFM converter emulates the equations of a synchronous machine in its control system. Depending on the implementation, both electromechanical and electromagnetic equations can be used [21].

There are several implementations of VSM-GFM converter in the literature for different applications. For instance, the complete set of equations of a synchronous machine is emulated in the VISMA and Synchronverter implementation [22], [23]. For reducing unnecessary complications, reduced electromechanical and electromagnetic equations have also been proposed in the Virtual Synchronous Generator [24] and Synchronous Power Controller (SPC) implementation[25]. By emulating fully or partially the dynamics of a synchronous machine, the VSM-GFM converter can provide support to the grid only in the steady-state as well as during transient events. The effectiveness of VSM-GFM in supporting frequency regulation and damping subsynchronous oscillation has also been reported [25], [26].

Despite the rich literature on control implementation for VSM-GFM, there are still several major research questions that have not been fully addressed such as:

i. The main objective of the VSM-GFM converter is to enhance the stability of the grid. Yet, one important fact which has not been seriously considered by the researchers is that the grid conditions cannot be improved if the power converter itself is not stable. Indeed, power converters have been known for being more fragile when connected to weak grids due to resonances. Thus, it is of importance to ensure a stable operation of the GFM converter itself under a wide range of grid conditions.

ii. Most of the implementations for GFM converters are designed to program the GFM control algorithms on the digital controller of the power converter. However, this is not always straightforward as it may seem. In fact, firmware updates and additional testing are often required for implementing VSM-GFM converters. This requirement certainly increases the development costs and efforts and therefore

hinders the actual deployment of GFM algorithms. Moreover, mass firmware updates and testing for commissioned converters have been proved to be not cost-effective.

iii. Most of the existing grid-forming implementations solely focus on providing inertia response. However, there is only a handful of developments that target power oscillation damping capability which could potentially be provided by a power converter. Even though synthetic inertia response is vital for low-inertia power systems, damping power oscillations is by no means less crucial.

1.3 Objectives of Dissertation

This PhD thesis aims to address the aforementioned research gaps using both theoretical and empirical approaches. Indeed, research works conducted focuses on the two pressing stability issues in power electronics dominated power systems namely, frequency stability and rotor angle stability. Particularly, the objectives of the PhD thesis are to:

i. Redesign the inner control loop of the GFM converter to ensure its internal stability for a wider range of disturbances including variations in grid impedance and distortion grid voltages. In this regard, new parameters tuning approach based on optimization will be devised to simplify the tuning process for the current controller which could potentially have more than ten tunable parameters. Furthermore, this new inner controller will also eliminate the need for grid voltage sensors for purpose of reducing implementation cost and complexity for the grid-connected power converters.

ii. Devise a control framework that allows implementation of grid-forming functions on external control hardware that communicates with the conventional GFL converter through a digital link. This way, modification of the firmware of the power converter can be avoided. The functions implemented in the external control hardware can be tailored to meet different communication specifications. In this regard, the influence of communication delay on the system performance and stability of the GFM will also be investigated.

iii. Propose a new concept for the implementation of a GFM converter that does not only provide inertia support but also enhance the rotor angle stability of the grid. In

particular, this PhD thesis aims to extend the current virtualization concept of synchronous machine emulation to a newer level where an emulated machine can have more than one virtual rotor. This unique feature will allow the GFM converter to damp multiple oscillatory modes selectively with higher flexibility.

1.4 Organization of Dissertation

The remaining chapters of this dissertation are organized as follows:

Chapter 2 reviews the existing control approaches for grid-connected power converters. The two dominant control schemes, namely GFL and GFM converters are discussed. In particular, different implementations of the GFM converter will be analysed. Also, this chapter will summarize key aspects in tuning parameters for the GFM based on synchronous power controller which is used intensively in the subsequent chapters.

Chapter 3 focuses on improving the internal control of grid-forming converters. In this chapter, a robust voltage sensorless current controller, which is based on internal model principle and linear matrix inequality technique, is proposed to ensure the stability of the current control loop under the presence of various grid uncertainties e.g., variation in the grid impedance when the power converter is connected to a week grid. Experiments using a laboratory prototype are conducted for assessing the performance of the controller.

Chapter 4 presents a new implementation strategy for GFM converters using external control hardware to overcome the requirement of modifying the internal firmware of power converters. In addition to the overall description of the control architecture, parameter tuning with respect to communication delay will also be provided. It will be shown that such a new implementation is suitable for both a single power converter and renewable power plants.

In chapter 5, An advanced implementation for GFM to provide enhanced power oscillation damping capability will be presented. This new implementation is devised by using the multi-rotor virtual machine approach where the GFM converter emulates not only one rotor but several ones simultaneously. Consequently, such a GFM converter is able to damp multiple critical modes at the same time with an adjustable damping effect. The proposed control scheme will be numerically validated with an IEEE benchmark power system.

Finally, conclusions and future works are provided in Chapter 6.

1.5 List of Publications

During the PhD project, contributions and results have been published in journals and presented at conferences.

1.5.1 Journal papers

1. **N. B. Lai**, G. N. Baltas and P. Rodriguez, "Multi-Rotor Virtual Machine for Grid-Forming Converter to Damp Sub-Synchronous Resonances," *IEEE Access*, vol. 9, pp. 128178-128187, 2021, doi: 10.1109/ACCESS.2021.3112070.

2. **N. B. Lai**, A. Tarrasó, G. N. Baltas, L. V. Marin Arevalo and P. Rodriguez, "External Inertia Emulation Controller for Grid-Following Power Converter," *IEEE Transactions on Industry Applications*, vol. 57, no. 6, pp. 6568-6576, Nov.-Dec. 2021.

3. **N. B. Lai**, K. Kim and P. Rodriguez, "Voltage Sensorless Control Scheme Based on Extended-State Estimator for a Grid-Connected Inverter," *IEEE Transactions on Power Electronics*, vol. 35, no. 6, pp. 5873-5882, June 2020.

4. A. Tarrasó, **N. B. Lai**, C. Verdugo, J. I. Candela and P. Rodriguez, "Design of Controller for Virtual Synchronous Power Plant," *IEEE Transactions on Industry Applications*, vol. 57, no. 4, pp. 4033-4041, July-Aug. 2021.

5. G. N. Baltas, **N. B. Lai**, A. Tarraso, L. Marin, F. Blaabjerg, and P. Rodriguez, "AI-Based Damping of Electromechanical Oscillations by Using Grid-Connected Converter," Front. Energy Res., vol. 9, Mar. 2021.

6. G. N. Baltas, **N. B. Lai**, L. Marin, A. Tarrasó and P. Rodriguez, "Grid-Forming Power Converters Tuned Through Artificial Intelligence to Damp Subsynchronous Interactions in Electrical Grids," *IEEE Access*, vol. 8, pp. 93369-93379, 2020.

7. A. Tarraso, **N.B. Lai**, G. N. Baltas, and P. Rodriguez, "Power Quality Services Provided by Virtually Synchronous FACTS," *Energies*, vol. 12, no. 17, p. 3292, Aug. 2019.

1.5.2 Book chapter

1. P. Rodriguez and **N. B. Lai**, "Grid-following and grid-forming PV and wind turbines," in *Control of Power Electronic Converters and Systems*, Elsevier, 2021, pp. 499–521.

1.5.3 Patent

1. P. Rodriguez, J. Ignacio Candela, A. Tarraso, **N. B. Lai**, and A. Luna, "Método de control síncrono para plantas con múltiples unidades de generación de potencia distribuida," Spain, 2021, Patent number ES2816798A1.

1.5.4 Conference papers

1. **N. B. Lai,** L. Marín, A. Tarrasó, G. N. Baltas and P. Rodriguez, "Frequency Selective Damping of Sub-synchronous Oscillations for Grid-Forming Power Converters," *2021 IEEE Energy Conversion Congress and Exposition (ECCE)*, 2021, pp. 877-881.

2. **N. B. Lai**, A. Tarrasó and P. Rodriguez, "Efficient Management of Energy Storage Systems using Competitive Controller," *2021 IEEE 12th International Symposium on Power Electronics for Distributed Generation Systems (PEDG)*, 2021, pp. 1-3.

3. **N. B. Lai**, G. N. Baltas, L. Marin, A. Tarrasó and P. Rodriguez, "Voltage Sensorless Control for Grid-connected Power Converters based on State Feedback and State Observer," *2020 IEEE 21st Workshop on Control and Modeling for Power Electronics (COMPEL)*, 2020, pp. 1-5.

4. **N. B. Lai**, A. Tarraso, G. N. Baltas, L. Marin and P. Rodriguez, "Inertia Emulation in Power Converters with Communication Delays," *2020 IEEE Energy Conversion Congress and Exposition (ECCE)*, 2020, pp. 1665-1669.

5. **N. B. Lai**, A. Tarrasó and P. Rodriguez, "LMI-based Control Design to Enhance Robustness of Synchronous Power Controller," *2019 IEEE Energy Conversion Congress and Exposition (ECCE)*, 2019, pp. 1429-1433.

6. A. Tarrasó, **N. B. Lai** and P. Rodriguez, "Resynchronization Strategy for a 200kVA Grid- Forming Power Converter," *2021 IEEE Energy Conversion Congress and Exposition (ECCE)*, 2021, pp. 1000-1005.

7. A. Tarraso, **N. B. Lai** and P. Rodriguez, "Synchronous Fault Compensator for Voltage Sensorless Grid-Following Power Converters," *2021 IEEE 12th International Symposium on Power Electronics for Distributed Generation Systems (PEDG)*, 2021, pp. 1-5.

8. A. Tarraso, **N. B. Lai**, G. N. Baltas and P. Rodriguez, "Voltage Sensorless Grid-Forming Power Converters," *2020 IEEE 21st Workshop on Control and Modeling for Power Electronics (COMPEL)*, 2020, pp. 1-5.

9. G. N. Baltas, **N. Bao Lai**, L. Marini, A. Tarrasó and P. Rodriguez, "Grid-forming Power Converter controller with Artificial Intelligence to Attenuate Inter-Area Modes," *2020 IEEE 21st Workshop on Control and Modeling for Power Electronics (COMPEL)*, 2020, pp. 1-5.

10. L. Marin, A. Tarrasó, **N. B. Lai**, G. N. Baltas and P. Rodriguez, "Small-signal Model and Analysis of a Grid-forming Power Converter based on the Synchronous Power Controller," *2020 IEEE 21st Workshop on Control and Modeling for Power Electronics (COMPEL)*, 2020, pp. 1-6.

11. A. Tarraso, L. Marín, **N. B. Lai** and P. Rodriguez, "Enhanced Proportional-Resonant (PR) Controller with Negative Decoupling for Weak Grids," *2020 IEEE 21st Workshop on Control and Modeling for Power Electronics (COMPEL)*, 2020, pp. 1-4.

12. G. N. Baltas, **N. B. Lai**, L. Marin, A. Tarraso and P. Rodriguez, "A Growing Self-Organising Maps Implementation for Coherency Identification in a Power Electronics Dominated Power System," *2020 IEEE Energy Conversion Congress and Exposition (ECCE)*, 2020, pp. 1963-1967.

13. A. Tarrasó, J. I. Candela, **N. B. Lai**, G. N. Baltas and P. Rodriguez, "Virtual Admittance PLL Structure for Grid-forming Power Converters in Microgrids," *2020 IEEE Energy Conversion Congress and Exposition (ECCE)*, 2020, pp. 5007-5011.

14. A. Tarrasó, C. Verdugo, **N. B. Lai**, J. Ignacio Candela and P. Rodriguez, "Synchronous Power Controller for Distributed Generation Units," *2019 IEEE Energy Conversion Congress and Exposition (ECCE)*, 2019, pp. 4660-4664.

CHAPTER
2.

Control of Grid Power Converters

This chapter reviews various control strategies commonly used for grid-connected power converters. Section 2.1 introduces the overall development trends and considerations for the control system of grid-connected power converters. Section 2.2 discusses the generic control structures of a GFL converter with a special focus on the basic control blocks. As the main focus of this chapter, Section 2.3 presents popular GFM schemes. Then, guidelines for parameter design for an SPC-based GFM converter is presented in Section 2.4. Finally, the summary of the chapter is given in Section 2.5.

2.1 Introduction

Grid-connected power converters (GCC) were originally designed with a primary objective to deliver energy from renewable sources to the grid as most efficient as possible. Thus, reference tracking was of the utmost importance. However, as grid codes become more and more stringent, additional functionalities such as harmonic suppression, unbalanced current injection, and low-voltage ride-through to name a few have also been required for power converters. In general, these additional requirements are often met by enhancing the control system of the GCC, for instance, harmonics suppression might be achieved by adding resonant terms to the current controller. Nevertheless, most of the functions implemented in GCC are focused on improving the internal stability of the power converter rather than supporting the grid, especially in the case of GFL converters which solely follow the grid voltage measured at the PCC. As a result, GFL converters do not support the operation of the grid.

Due to the increase in renewable installation and replacement of the synchronous generations, grid strength reduces significantly during the last years. In particular, grid inertia and damping of some power systems have become critically low [27]. Thus, it becomes apparent that GCC should also provide grid-supporting functionalities to the grid.

In fact, this has been the main motivation for the GFM concept which aims to control GCC in a more flexible manner. GFM strategies attempt to maintain the highly efficient operation of GCC during steady-state while providing support to the grid during transient events.

2.2 Grid-following Power Converters

GFL controller refers to a group of control approaches where the regulation of the injected active and reactive is solely based on the grid voltages. That is, the GFL converter uses the magnitude and angle of the grid voltage to determine the setpoints for the injected currents. For this purpose, the control system of the GCC converter usually consists of four control blocks, namely the pulse-width modulation (PWM), the current controller, the phase-locked loop (PLL), and the power controller. The overall configuration of a GLF converter is depicted in Fig. 2.1. In general, energy from renewable resources and energy storage systems are transformed into a stable DC source either by using rectifiers or DC-DC converters before being injected into the grid. Such a DC source acts as the primary source for the grid-connected power converter. Due to the fact that the dynamics of the DC link is nearly decoupled from those of the AC side, the impact of DC-link voltage can be omitted when designing the current controller. The GCC is connected to the grid through an inductance to smoothen the switching ripples in inverter currents. To reduce the filter size as well as to increase the harmonics attenuation capability, LCL filters are more often used. Without losing genericity, an LCL-filtered converter is considered throughout this PhD thesis.

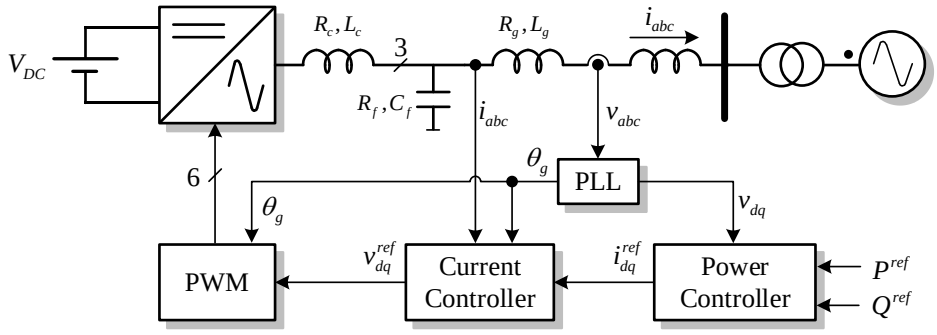

Fig. 2.1. Overall configuration of a GFL: Power circuit and control system.

Among the four control blocks, the current controller and the phase-locked loop are the most important ones when it comes to the stability and performance of a GFL converter. The current controller can be implemented in the stationary reference frame or the synchronous reference frame. Both implementations have their advantages. Indeed, it is more straightforward to implement current limitations on *dq*-reference since the

fundamental components are of DC quantities. On the other hand, the implementation on $\alpha\beta$ - frame can eliminate the need for the decoupling network as well as the use of PLL estimates in the PWM block which simplifies the overall implementation and analyses. There are multiple ways to calculate the references for the current controller from the power setpoints. For instance, the power setpoints could be tracked by a PI controller whose outputs are reference currents. A more simple and reliable approach is to calculate the reference currents directly from the power setpoints by using the below equations.

$$i_d^{ref} = \frac{Pv_d + Qv_q}{v_d^2 + v_q^2} \tag{2.1}$$

$$i_q^{ref} = \frac{Pv_q - Qv_d}{v_d^2 + v_q^2} \tag{2.2}$$

where the subscript dq denotes the direct and quadrature components of the voltage and current in the synchronous reference frame. For implementation in the $\alpha\beta$ -reference frame, the equations are also in a similar form.

The control structure of the proportional-integral (PI) based current controller is shown in Fig. 2.2. In this case, as the reference currents are required to be in a dc form, Park's transformation is used to convert the currents and grid voltages from the natural reference frame into the synchronous reference frame by using the grid angle estimated by the PLL. To cancel out the crossed-coupling dynamics between the *d*-axis and *q*-axis components, a decoupling network is also used. This decoupling network helps to separate the dynamics of the active power and reactive power, resulting in more independent control of these two quantities. The voltage references are transformed to the $\alpha\beta$-frame for modulation purposes. To improve the transient response of the current controller, measured grid voltages are sometimes used as feedforward signals.

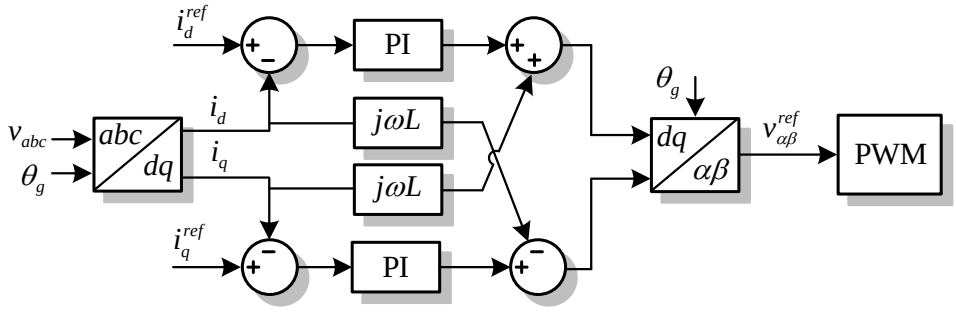

Fig. 2.2. Proportional-integral current controller for GFL converter.

The current controller can also be implemented in the stationary reference frame as shown in Fig. 2.3. The major difference is that proportional-resonant (PR) controllers are used instead of the PI controllers. PR controller allows the reference currents which have synchronous frequency to be tracked asymptotically. Moreover, PLL and decoupling networks are not required in this implementation.

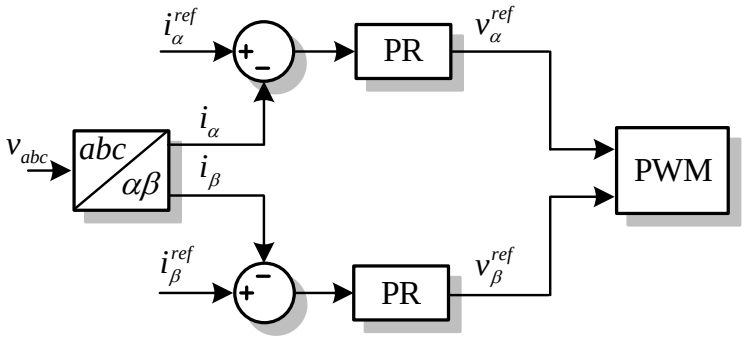

Fig. 2.3. Proportional-resonant current controller for GFL converter.

Having an equally important role in the performance and stability of the power converters, the PLL is mainly used to estimate the magnitude and angle of the grid voltage from the measurements at the point of connection. Fig. 2.4 shows the PLL implemented on the synchronous reference frame. This type of PLL is often referred to as SRF-PLL. The SRF-PLL and its variants are widely used for grid-connected applications due to its simplicity and robustness [28]. Nevertheless, this type of PLL is not able to obtain a proper estimation under distorted and unbalanced grid voltage conditions. To address such a limitation, a moving average filter has also been used to filter out the higher-order harmonics from the estimated phase angle as in [29].

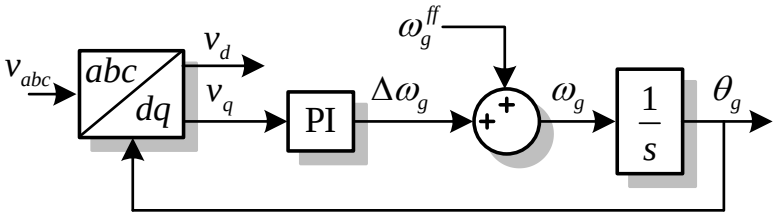

Fig. 2.4. Synchronous reference frame phase-locked loop.

2.3 Grid-forming Power Converters

In recent years, the interest in power converters has shifted from internal stability towards the global stability of the grid. That is, there have been an increasing amount of

research works aiming to take advantage of the fast dynamics of power converters to enhance grid stability and performance. This has been the main motivation for the concept of the GFM converter. Even though the development of GFM converters have just become relevant in the last few years due to the new grid codes, the concept was coined a decade ago by academia [30]. According to the initial definition [30], grid-forming converters are controlled as voltage source which is capable of working in both grid-connected and islanded mode. This definition is derived from the perspective of controlling a power converter. Recently, a more power system-oriented definition has been proposed by ENTSO-E. This new definition is, as described in the previous chapter, based on the functionalities that should be provided by the power converter such as inertia response, power oscillation damping among others.

Recently, there have been a number of proposals for GFM converters. Broadly speaking, these approaches fall into two groups, namely voltage source-based techniques and virtual synchronous machine (VSM)-based techniques. The former are realized following the working principle of uninterrupted power supplies and is more popular in small systems or microgrids where electromagnetic interactions between the generation units are of the primary concern. In contrast, electromechanical dynamics are of more relevance in power systems with higher penetration of renewables and energy storage systems. This issue is currently addressed by using the VSM-GFM converter where the power converter acts as a mechanical synchronous machine in responding to a grid event.

Due to the fact that the VSM-GFM converter is more effective and relevant for grid-connected applications, this section is devoted to reviewing the common implementations of VSM-GFM converters. In fact, these implementations will be analysed from the dynamical interaction perspective. That is, the control structures of these approaches will not be discussed based on their functionalities but based on their dynamical interactions with the grid.

2.3.1 Implementation tree

Independent of their control structures, the functions of existing GFM approaches can be analysed from the perspective of synchronization, electromechanical interaction, and electromagnetic interaction with the grid as shown in Fig. 2.5. Grid-synchronization refers to the ability of power converters to keep synchronism with the grid. Such synchronism is needed to regulate the power exchange with the grid and is often achieved through using either the grid voltage or the injected power. Indeed, a power converter can track the angle and magnitude of grid voltage by using a PLL. This approach is relatively simple and has been commonly used for GFL converters. The main disadvantage of voltage-based

synchronization approaches is potential instability. In fact, the PLL is tuned to meet internal transient specifications such as overshoot and settling time for frequency estimation rather than grid conditions. However, under weak grid conditions, i.e. low short circuit ratio, PLLs become unable to estimate grid voltage properly which can easily cause instabilities. On the other hand, power-based synchronization is more resilient because the power the grid frequency is estimated through the power deviation which is the direct result of the interaction between the power converter and the grid.

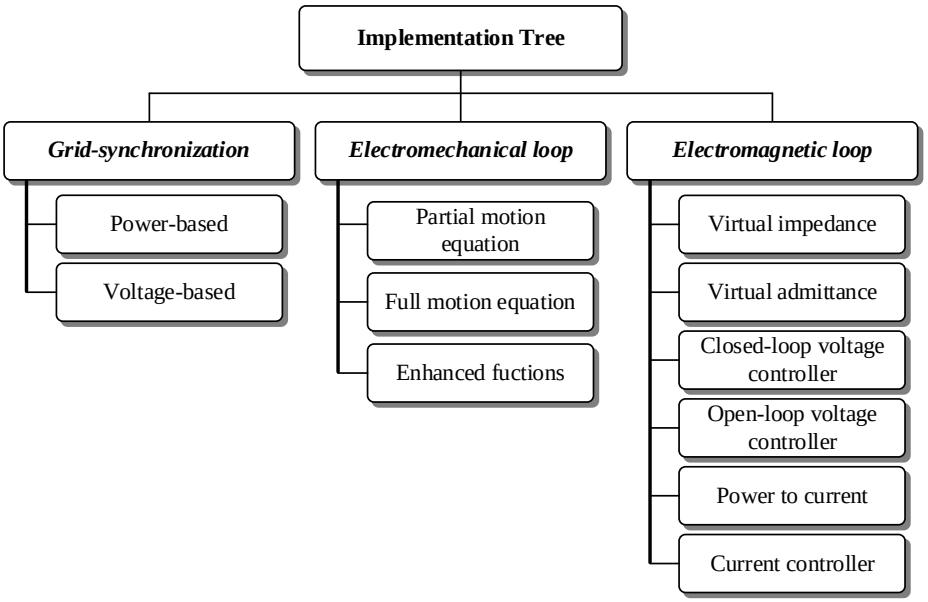

Fig. 2.5. Classification of control blocks of a grid-forming converter.

The focus of GFM converters is to provide dynamic support to the grid through their electromechanical loop. This control loop determines the behaviour of the GFM converters in a time frame ranging from hundreds of milliseconds to a few seconds. To mimic the operation of conventional generations, this control layer is realized by emulating the motion equation of a synchronous generator. Depending on the implementation, the motion equation can be partially or fully emulated. In some cases, advanced functions can be incorporated into this control layer to provide additional functionalities which cannot be obtained with a simple motion equation.

Central to the internal stability of the GFM converters, the functions that focus on electromagnetic transients are implemented in the electromagnetic layer. The control blocks for this loop are greatly varied for the existing GFM implementation. In fact, this control layer can be implemented by using an open-loop voltage controller i.e. voltage references

generated by the electromechanical loop are fed directly to the PWM block. Though simple, this approach is not practical since it is not possible to control the injected current. In most cases, a current controller is needed in the GFM implementation. The reference currents can be generated directly from the reference power, which is referred to as the power-to-current approach. Oftentimes, the output of the electromechanical layer is reference voltage rather than power. Therefore, a closed-loop voltage controller is often used in GFM implementation. As the GFM are also required to operate in parallel with other GFMs as well as the grid, virtual admittance or virtual impedance are often employed to improve power-sharing capacity.

2.3.2 Virtual Synchronous Machine

As the first VSM-GFM implementation, the virtual synchronous machine (VISMA) is patented in 2006 [31] and then published in an article in 2007 [22]. The electromechanical layer of the VISMA is based on a detailed model of an SG, which receives the virtual mechanical torque and excitation voltage as references. The VISMA emulates both the swing and the flux linkage equations, encompassing the stator, the excitation and damper windings. These equations dictate the current flowing through the stator of the VISMA as a function of the rotor voltage, angle, and grid voltages. Such output currents are employed as reference values for the internal current controller, which eventually controls the current injected by the power converter. Even though the hysteresis current controller is employed in the VISMA implementation, any other current controller might be also used. The control block diagram of the VISMA is shown in Fig. 2.6. Inputs of the VISMA include active and reactive reference powers, and grid voltages. The reference powers can be calculated through the voltage and frequency droop controllers to improves power sharing during parallel operation.

The main advantage of the VISMA implementation is the use of power-based synchronization which is certainly more grid friendly and stable during islanded operation. Nevertheless, the VISMA realization is rather complex. In fact, many parameters and equations are needed for implementing the virtual machine, which leads to higher computation times and is less reliable. Furthermore, the VISMA inherits all characteristics of an SG, even though some are undesired, such as weak damping and slow transient response. To provide harmonic and imbalance compensation, a PLL-based compensator can be integrated into the VISMA as in [32].

Fig. 2.7 shows the implementation tree for the VISMA. As shown, the VISMA is built upon the power-based synchronization method through the emulation of the motion equation of an SG. Nevertheless, voltage-based frequency estimation for harmonic

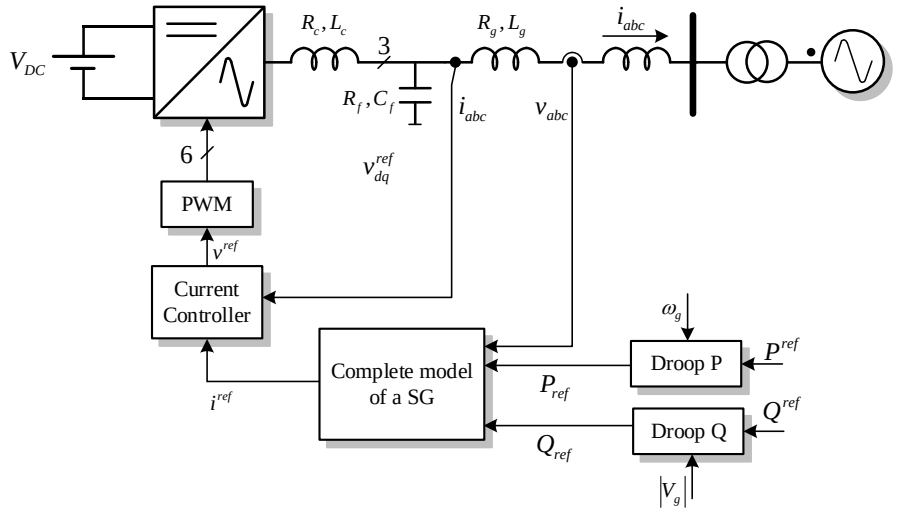

Fig. 2.6. Control block diagram of the virtual synchronous machine (VISMA).

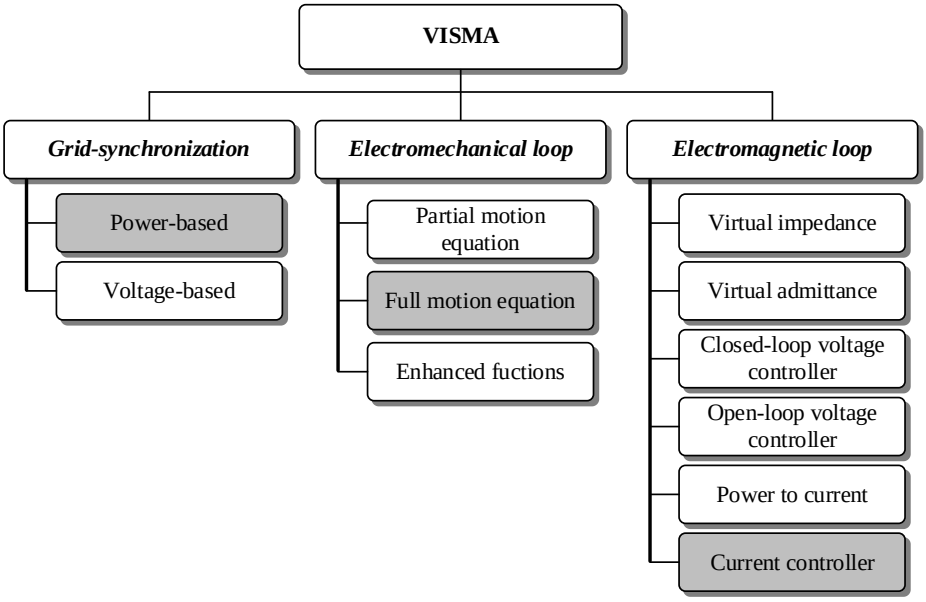

Fig. 2.7. Implementation tree for the VISMA-based GFM converter.

compensation is still based on grid voltage measurements. With regard to the electromagnetic layer, the VISMA faithfully implements the full set of equations of an SG, which is indeed a drawback due to the unnecessary complexity required in actual realization. The electromagnetic interaction of the VISMA relies mainly on the emulation of the stator circuit of an SG to calculate the references for the injected current which is then regulated by a current controller. Due to the lack of a voltage control loop, it is not

straightforward to provide voltage support functions using the VISMA. Further improvements on damping and voltage control capability for the VISMA are also proposed in [33] where the electromechanical layer is simplified to emulating only the inertia and damping coefficient. In addition, a closed-loop controller based on virtual admittance is included. Further improvement based on virtual impedance is also presented in the literature [34].

2.3.3 Virtual Synchronous Generator

The first implementation for the virtual synchronous generator (VSG) is proposed in 2007 in the framework of the VSYNC project which aims to incorporate short-term energy storage with grid support capability into the grid for stability purposes [35]. The control diagram of the VSG is shown in Fig. 2.8. Regarding control structure, the VSG is relatively close to a conventional GFL approach. That is, the VSG is constituted by a PLL and a current controller. The reference currents are generated by the power-to-current block which computes explicitly the current by using the following equations.

$$i_d = \frac{Pv_d + Qv_q}{v_d^2 + v_q^2} \tag{2.3}$$

$$i_q = \frac{Pv_q - Qv_d}{v_d^2 + v_q^2} \tag{2.4}$$

Different from a conventional GFL converter, the PLL block of the VSG is modified to emulate the dynamics of an SG. In fact, the PI controller commonly employed in the SRF-PLL is replaced by a single integrator whose gain k_i represents the inertia constant of the virtual machine. The damping of the VSG is determined by the damping coefficient k_{damp} which is indeed used to generate a compensation active power from the estimated grid frequency. Together with this compensation term, the original references power is also modified by the PLL through RoCoF term to provide inertia response.

The VSG has been employed in a number of applications including grid frequency control, islanded operation, microgrid operation including black-start [36]. Several experimental works have been reported for the VSG implementation. For instance, the demo of 5 kW is conducted in the Netherland in 2009 [37]. A demonstration of a more significant power level was launched in Romania in the same year for supplying a residential load [24]. Further real-time simulations were also conducted to investigate the interaction between the VSG and the grid [38] where the capability of the VSG to provide dynamic frequency support is confirmed.

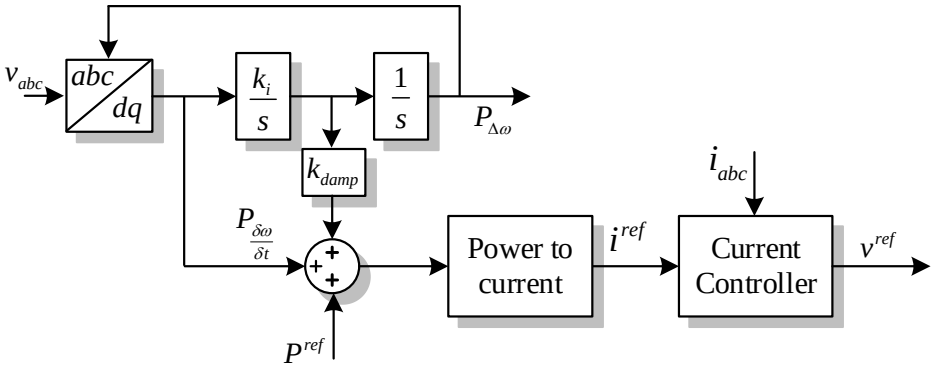

Fig. 2.8. Control block diagram of the virtual synchronous generator (VSG).

Due to the use of a PLL, the grid-synchronization method of the VSG falls into a voltage-based approach. Furthermore, since only inertia and damping of the swing equation are taken into account, the electromechanical layer of the VSG emulates partially the motion equation. As for the electromagnetic layer, the VSG is composed of the power-to-current block and a current controller. The implementation tree for the VSG-GFM can be derived as in Fig. 2.9.

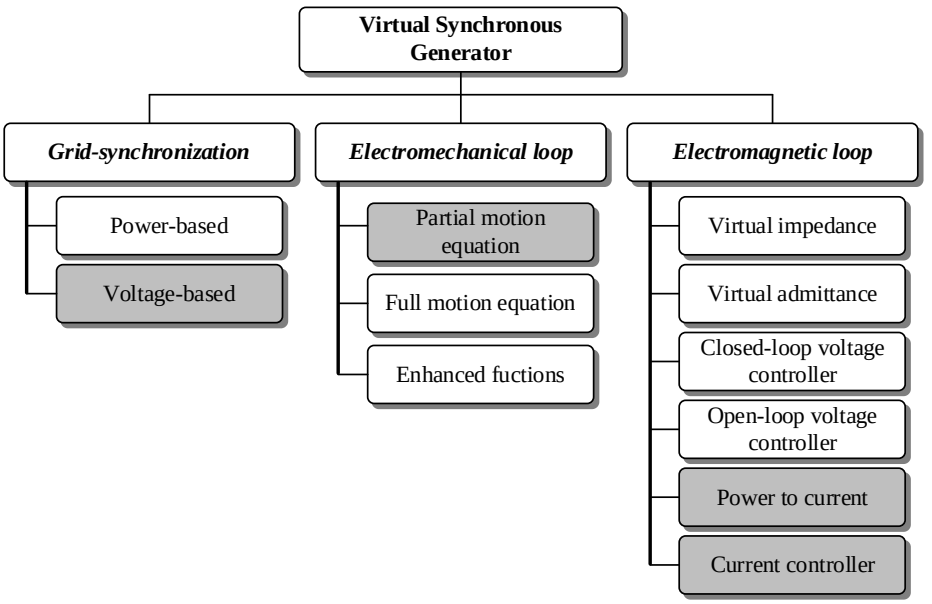

Fig. 2.9. Implementation tree for the VSG-based GFM converter.

It is obvious from the implementation tree that the VSG is relatively simple but quite effective. The main advantage of the VSG is its control structure which is considerably similar to the conventional GFM except for the parameters of the PLL and the compensation terms for active power. Nevertheless, due to the voltage-based synchronization, the VSG bears the same potential instability issues when operated in weak-grid conditions. Furthermore, the VSG does not provide the means for controlling the PCC voltage owning to the lack of a dedicated voltage control unit. In conclusion, the VSG implementation is ideal when only grid frequency regulation is the main objective. For applications that have more complex control requirements, the VSG could be insufficient.

2.3.4 Synchronverter

The Synchronverter is among the most referred implementations for GFM converters. The synchronverter, originally named static synchronous generator, was proposed in 2009 in an attempt to force power converters to behave like SGs from the grid's perspective [39]. Due to its grid-friendly characteristics, the synchronverter was adopted in various applications such as in electrical drive systems [40], STATCOM [41], phase-locked loop [42], power system stabilizer [43] to name a few. The control block diagram of the synchronverter is shown in Fig. 2.10. Much similar to the VISMA implementation, the synchronverter aims to emulate most of the equations of an SG. In general, the synchronverter implement the electromechanical loop using a simplified swing equation with only inertia constant. For parallel operation, voltage and frequency droop are also used. The output of the synchronverter is the reference voltage which is fed directly to the PWM.

For such an initial implementation, the implementation tree for the synchronverter can be illustrated in Fig. 2.11. Even though the synchronization of the synchronverter is based on active power during operation, PLL is still needed for starting up the system. This feature may add overall complexity to the implementation and operation of the converter. Likewise, the electromagnetic layer, which is made of only inertia constant, may suffer from insufficient damping. As another drawback, since the synchronverter relies on an open-loop voltage controller, there is a limited possibility to control the injected current in case harmonic compensation or sequence control is required. Despite the above demerits, since the synchronverter is quite well described and explained in the literature, it is widely adopted for GFM converters.

Over the years, many attempts have been made to further validate and improve the synchronverter implementation. That is, considerable improvements have taken place in all the layers of the synchronverter implementation tree. In 2013, a PI controller was added to the voltage control loop to compensate for parameter mismatches, which slightly modified

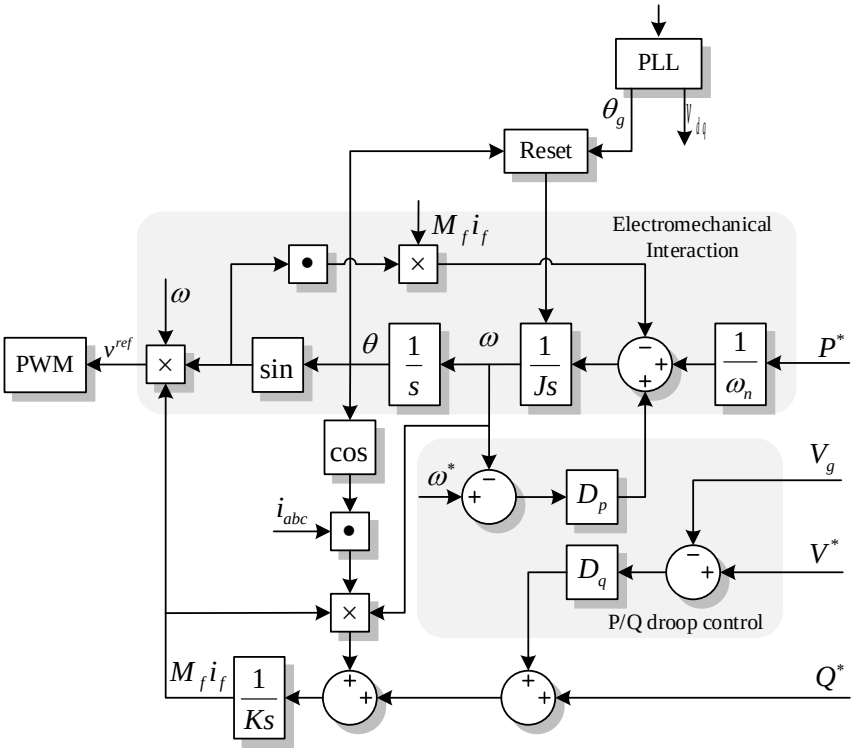

Fig. 2.10. Control block diagram of the synchronverter.

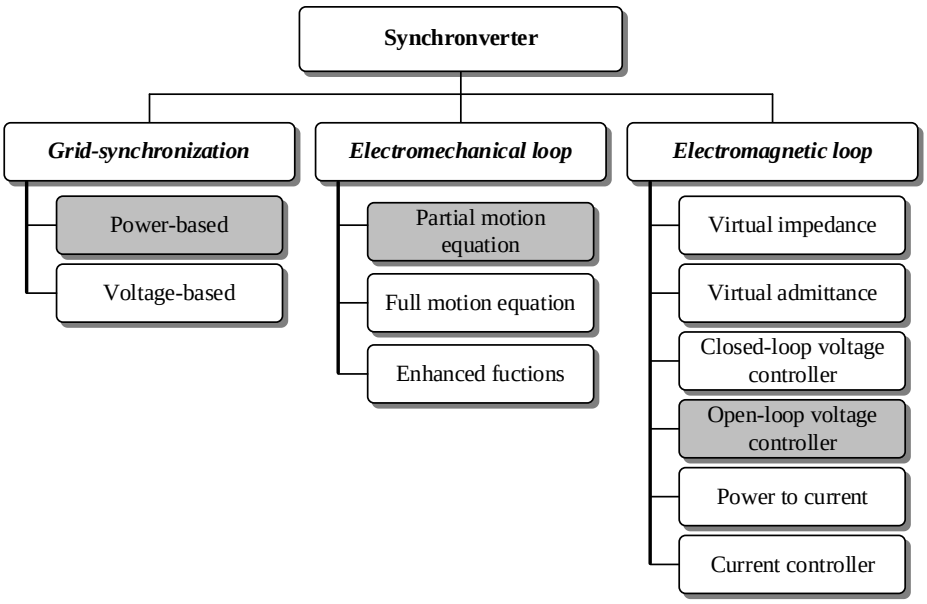

Fig. 2.11. Implementation tree for the synchronverter-based GFM converter.

modified the electromagnetic interaction layer [44]. Likewise, [45] compares the grid-supporting capabilities of the synchronverter with those provided by a synchronous machine. Notably, to eliminate the need for PLL during the start-up, a major modification was proposed for the synchronization layer in [46]. In fact, during the start-up process, reference active and reactive powers are set to zero. In addition, a PI controller and a virtual admittance are added to track grid voltage angular and amplitude

In 2017, the issue regarding electromagnetic interaction of synchronverter was also studied. It was concluded in [47] that synchronverter are less stable than synchronous machines of the same ratings since the inductance of the inverter filter of a typical three-phase inverter is much smaller than the stator inductance of a synchronous machine. To tackle this problem, virtual impedance is added to the voltage control loop to increase the total impedance of the synchronverter. The main idea behind this method is that a virtual impedance is added in series with an output filter, which virtually increases the total impedance of the synchronverter as shown in Fig. 2.12.

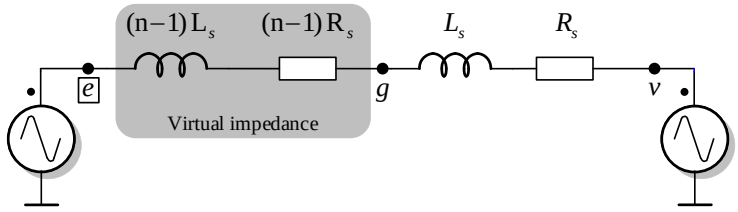

Fig. 2.12. Virtual impedance for the synchronverter.

From Fig. 2.12, the phase voltage applied to LCL filter g can be given as

$$g = \frac{(n-1)v + e}{n} \tag{2.5}$$

where v and e are grid voltage and back emf voltage, respectively. By using this approach, total impedance can be increased by n times of filter impedance. Obviously, the R/X ratio is unchangeable.

Electromechanical interaction of synchronverter with the grid was also investigated in [48]. It was confirmed that having a damping factor dependent on the droop coefficient is inconvenient since the dynamic response of the synchronverter cannot be adequately adjusted without affecting the steady-state droop characteristic. For the purpose of making the damping factor of the synchronverter independently adjustable, a damping correction loop is added to the synchronverter [48]. This is achieved by adding a derivative term to the active power feedback path. However, because of the introduction of a derivative term, low-

pass filters are required to implement this control scheme. To date, there is still limited evidence of the performance of the synchronverter under grid faults and islanding operation.

2.3.5 Power-Synchronization Loop

Being the simplest implementation for a VSM-based GFM converter, the power-synchronization loop (PSL) includes only the crucial parts of a VSM [49]. As shown in Fig. 2.13, the PSL mainly contains only an active power controller, a reactive power controller, and a filter-based resonant damper. The active power controller is formed by an integrator and a proportional gain which acts as virtual inertia constant. In addition to regulating the active power, this controller is also responsible for grid synchronization. Similarly, the reactive power controller aims to emulate the automatic voltage regulator (AVR). The outputs of the two controllers are grid voltage angle and reference voltage magnitude. Such outputs are combined to form the reference voltage for the power converter through the PWM.

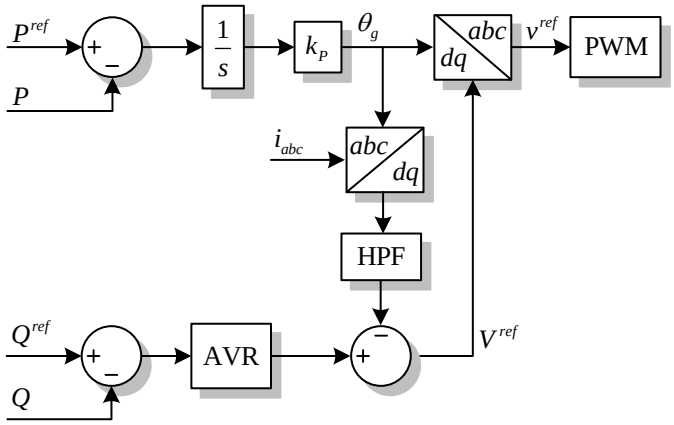

Fig. 2.13. Control block diagram of the power-synchronization loop.

Since the active power control loop consists of only an integrator, the PSL suffers from insufficient damping. Thus, a high-pass filter, whose input is the measured currents, is used to emulate the effect of a virtual resistor to eventually increase the damping of the PSL.

From Fig. 2.13, the implementation tree of the PSL can be derived as in Fig. 2.14. The synchronization of the PSL is mainly based on power regulation. Yet, a backup PLL is still highly recommended. Since only the inertia constant is taken into consideration, the PSL implements only partially the motion equation. This might limit the application of the PSL since adjustable damping through damping coefficients are more preferred. Especially, when the grid is in low inertia conditions or has a low damping ratio. The main disadvantage

of the PSL is attributed to the open-loop voltage controller. In fact, there is no voltage or current controller used in the PSL. Such lack of controllability makes it impossible to implement necessary functions such as harmonic compensation, negative-sequence voltage compensation, or voltage regulation to name a few. In conclusion, the simple structure of the PSL might make it easy for implementation. However, the lack of controllability on all control layers hinders the adoption of this implementation in real applications where power converters are required to deliver simultaneously multiple control functions. Further improvement and analyses of the PSL are reported in [50], [51].

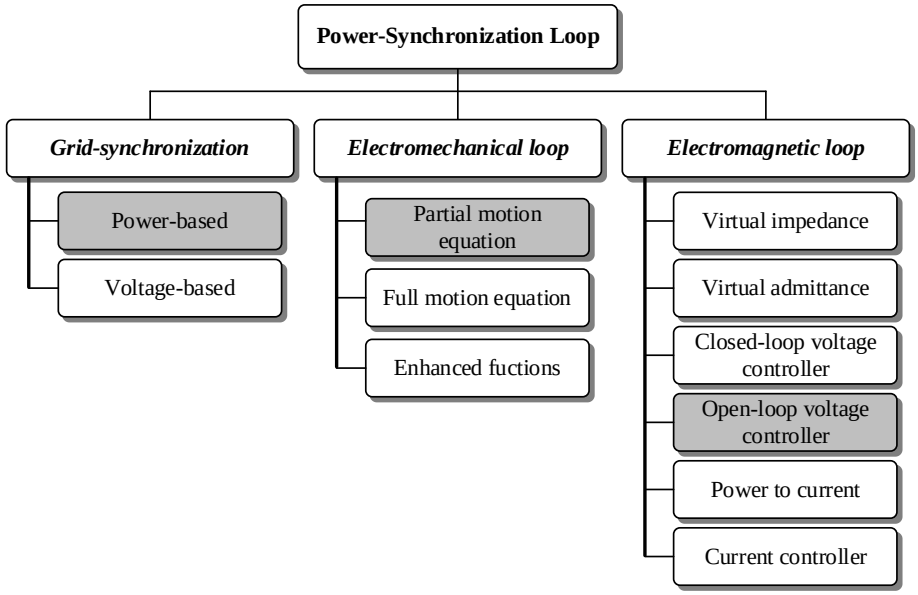

Fig. 2.14. Implementation tree of the PSL-based GFM converter.

2.3.6 Cascaded Voltage-Current Controller

Different from the aforementioned implementation, the cascaded voltage-current controller (CVCC) is devised from the power electronic perspective rather than the power system viewpoint. The CVCC is first proposed in 2013 [52], and further improved in [53] and [54]. As shown in Fig. 2.15, the CVCC primarily consists of four main control blocks, namely active power controller, reactive power controller, voltage controller, and current controller.

The active power controller is mainly based on the swing equation for the purpose of grid synchronization and power regulation. The virtual inertia constant of the CVCC can be set through T_a such that $T_a = 2H_v$. In addition, the damping of the electromagnetic loop is adjusted through the damping coefficient k_d. The output of the active power controller is

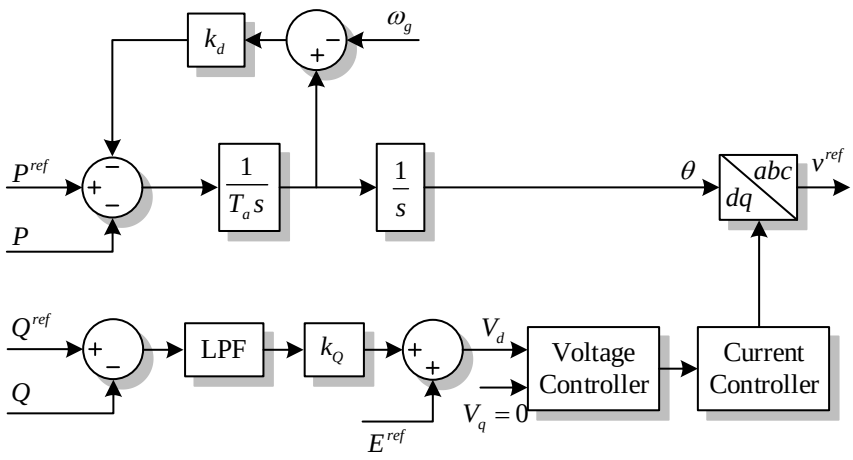

Fig. 2.15. Control block diagram of the cascaded voltage-current controller.

fed through an integrator block to obtain the estimated angle of the grid. Likewise, the reactive power controller is based on a conventional droop controller which can also provide voltage support to the grid. The reactive power controller is relatively simple with only a low-pass filter (LPF) to determine the dynamics and a droop coefficient k_0. The voltage and current controller are cascaded and implemented in the synchronous reference frame. However, this control structure can also be extended to the stationary reference frame.

The CVCC however entails some limitations in terms of dynamics such as inherent cascaded delays. Moreover, the bandwidth of the two cascaded control loops needs to be significantly different from one another to prevent coupling interactions. Indeed, [52] shows how, for low switching/sampling frequencies, the interactions between both cascaded control loops, make it difficult to select proper control parameters. As a remedy, a tuning approach based on eigenvalue sensitivities analyses of the linearized system model was proposed in [91]. Furthermore, to improve the quasi-stationary characteristic of the CVCC, virtual impedance is also used [54].

The implementation tree of the CVCC-GFM converter is shown in Fig. 2.16. The CVCC is synchronized with the grid through active power regulation which is considered an advantage because potential instability posed by PLL can be avoided. In addition, the electromechanical layer of the CVCC features a full implementation of the motion equation allowing individual adjustment of the inertia constant and damping. Similarly, the use of a closed-loop control structure for both voltage and current loop makes it easier to implement advanced control functions for current and voltage control. However, the voltage control loop of the CVCC also poses several drawbacks. Firstly, the voltage control loop is based on a PI controller which is not ideal for grid-connected applications because PCC voltage

is not easy to control in the case of a strong grid. Therefore, the voltage control loop might suffer from saturation crippling the whole control system. In addition, it is not straightforward to implement the virtual impedance in practice. As can be seen in (2.6), implementation of the virtual impedance block requires a derivative operator or equivalent approximation technique. As a general rule, the derivative operator is not preferred within a control system since noise can be easily amplified leading to degraded performance or even instabilities.

$$G_{vi}(s) = L_v s + R_v \tag{2.6}$$

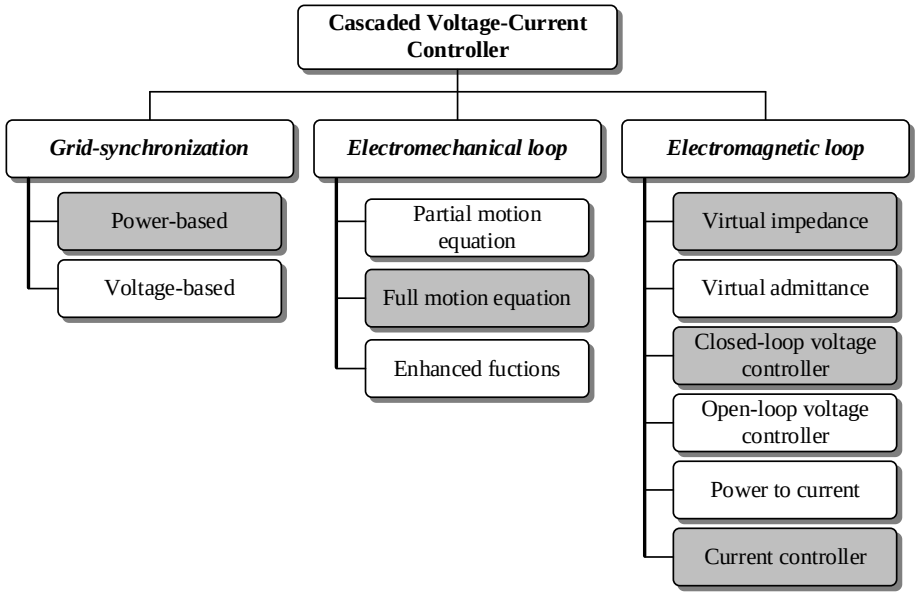

Fig. 2.16. Implementation tree for the CVCC-based GFM converter.

2.3.7 Synchronous Power Controller

It is fair to say that the synchronous power controller (SPC) captures very well the main advantages of the aforementioned control technique in a simple and stable implementation. The concept of the SPC was first patented in 2011[55] and later published in 2013 [56]. The main motivation of the SPC is to create a GFM converter that emulates the preferred dynamic characteristic of a conventional SG at the same time takes advantage of the flexibility of the power converter to incorporate advanced functions. Such advanced functions are usually unavailable in an SG.

The control block diagram of the SPC is depicted in Fig. 2.17. In general, the SPC consists of five main control blocks, namely the power loop controller (PLC), the reactive power controller, the voltage-controlled oscillator (VCO), the virtual admittance, and the

current controller. The PLC is based on the swing equation and is in charge of both grid-synchronization and active power regulation. The reactive power is often constructed by a PI controller for regulating the reactive power. Oftentimes, the bandwidth of the reactive power controller is significantly lower than that of the PLC to prevent the coupling effect. The outputs of the active and reactive power controller are estimated grid angle and reference grid voltage, respectively. The two quantities are used as inputs for the VCO which generates the instantaneous reference voltages either in the synchronous or stationary reference frame. The virtual admittance acts as the stator windings of an SG to transform the reference voltage into current references for the current controller.

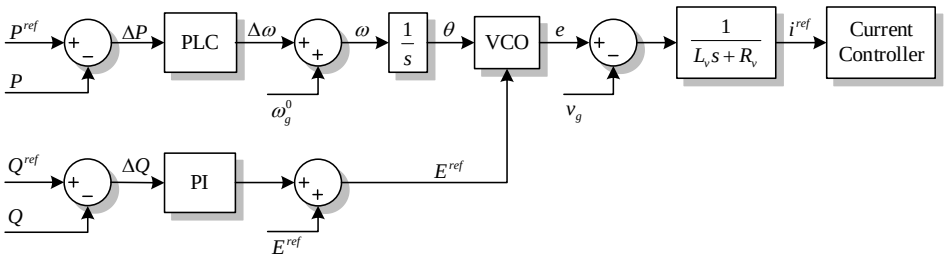

Fig. 2.17. Control block of the SPC.

It has been pointed out in [57] that the SPC might suffer from a high inherent droop coefficient if the SPC is to be sufficiently damped. This issue has been addressed by replacing the conventional swing equation with a lead-lag controller [58]. The lead-lag controller provides an additional degree of freedom that enables tuning separately the inertia, damping, and droop coefficient. In another work, the virtual admittance is enhanced by implementing multiple virtual admittance blocks in parallel to provide simultaneously harmonic suppression, sequence control of injected current, and transient improvement [59]. The SPC has been widely adopted in PV plants [60], HVDC [61], [62].

Fig. 2.18 shows the implementation tree of the SPC-based GFM converter. The grid-synchronization of the SPC is solely based on active power balancing which is advantageous in terms of overall stability under weak grid conditions. Unlike any other VSM-based implementation, the electromechanical layer of the SPC includes not only conventional swing equations but also advanced transfer functions such as the lead-lag controller to improve both transient and steady-state performance of the power converter. The same capabilities have also been proved for the electromagnetic layer. Another highlight of the SPC lies in the virtual admittance which can be generally given in the following equation.

$$G_{va}(s) = \frac{1}{L_v s + R_v} \tag{2.7}$$

It can be seen from (2.7) that the virtual impedance does not entail a derivative operator as in the case of CVCC. In fact, the implementation of the virtual impedance is rather simple and stable. The virtual admittance block can also be tuned to accommodate different voltage support requirements. As pointed out in [58], by appropriately selecting the virtual inductance L_v and the virtual resistance R_v, the SPC can easily meet voltage support criteria.

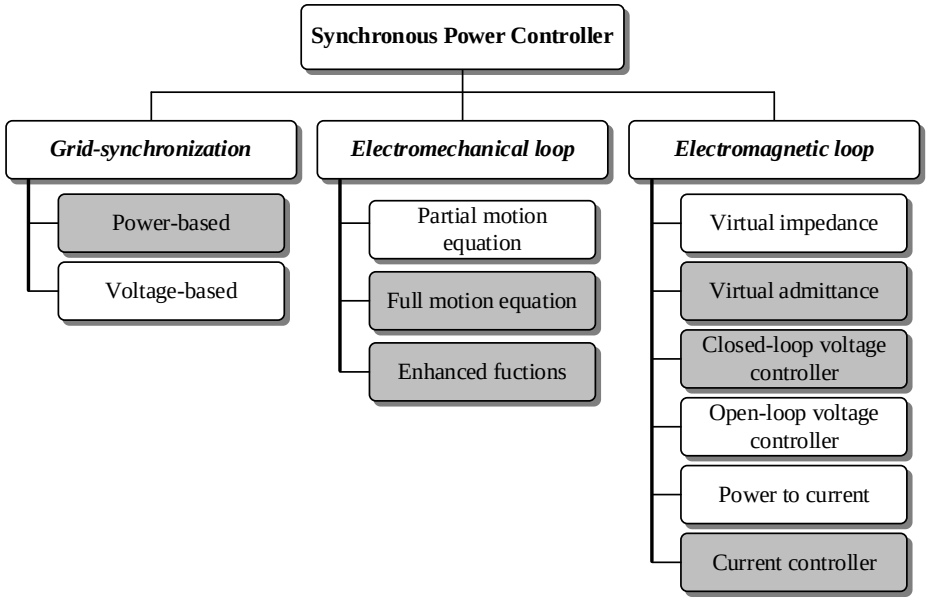

Fig. 2.18. Implementation tree of the SPC-based GFM converter.

2.4 SPC-based Grid-forming Converters

Due to its effectiveness and simple implementation, the SPC is used as the basis for designing the controllers used in the PhD thesis. Therefore, this section aims to dive into the parameter tuning and functionalities of the SPC. In general, the design of the SPC can be achieved by using the bottom-up approach. That is, the parameters of the SPC is often tuned from the current controller then the voltage controller, and lastly the active and reactive power controller. To simplify the parameter tuning of the controllers, the bandwidths of the controllers are often distinct from one another such that the dynamics of the inner loop controller does not interfere with those of the outer loop controller.

Similar to a conventional power converter, the current controller can be implemented in either a synchronous or stationary reference frame. Regardless of the internal control structure, the current controller should be able to track references in a fast and stable manner under a full range of grid operating conditions. Once the current controller is properly designed. The virtual admittance block can be tuned. Oftentimes, the virtual admittance block is designed to meet the voltage support requirements. In most cases, it is adequate to choose the virtual admittance as $X_v = \sqrt{L_v^2 + R_v^2} = 0.3\,\text{pu}$. The ratio between the virtual inductance and the virtual resistance can be selected such that the transient response of the voltage control loop is appropriately damped.

For tuning the active and reactive power control loop, it is convenient to consider only the power flow on the virtual admittance rather. Indeed, as the voltage control loop is much slower than the power control loop, the dynamics of the virtual admittance hardly has any influence on the dynamics of the power control loop. The active power flows determined by the virtual admittance can be calculated by the following equations.

$$P_A = \frac{E}{R_v^2 + X_v^2}\left[R_v\left(E - V_g\cos\delta\right) + X_v V_g \sin\delta\right] \tag{2.8}$$

where E is the reference voltage generated by the VCO, V_g is the grid voltage, and δ is load angle.

Given that the load angle is relatively small during normal operation, it is reasonable to assume $cos\,\delta \simeq 0$ and $sin\,\delta \simeq \delta$. The power flow equation in (2.8) can be written as

$$P_A = \frac{EX_v V_g}{R_v^2 + X_v^2}\delta\,. \tag{2.9}$$

Since the virtual resistance R_v is usually much smaller than the virtual impedance X_v, equation (2.9) can be further simplified as in the following.

$$P_A = \frac{EV_g}{X}\delta \tag{2.10}$$

Conveniently, the maximum power that can be delivered by the SPC is defined as

$$P_{\max} = \frac{EV_g}{X_v}\,. \tag{2.11}$$

Provided that $E \simeq V_g = 1$, equation (2.11) can be also expressed in per-unit form as

$$P_{\max}^{pu} = \frac{1}{X_v} = Y_v \,. \tag{2.12}$$

From (2.11) and assuming that reactive power controller is considerably slower than the SPC. The small-signal model of the SPC can be derived as in Fig. 2.19.

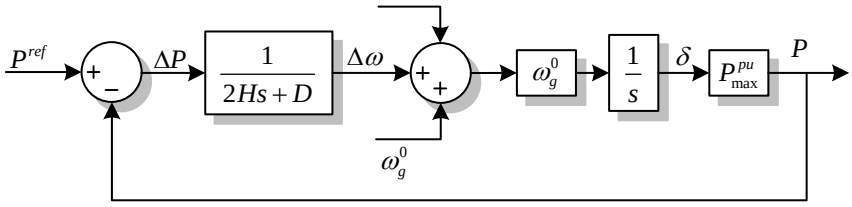

Fig. 2.19. Small-signal model of the SPC.

From the small-signal model, the closed-loop transfer function of the SPC is obtained as in the following.

$$G_{P2P}(s) = \frac{P_{\max}\omega_g^0}{2Hs^2 + Ds + P_{\max}\omega_g^0} \tag{2.13}$$

Comparing the denominator (2.13) with that of a standard second-order system, one might easily see that

$$\omega_n = \sqrt{\frac{P_{\max}\omega_g^0}{2H}} \tag{2.14}$$

$$\zeta = \frac{D}{4H\omega_n} \tag{2.15}$$

where ω_n and ζ are natural frequency and damping ratio of the SPC. Normally, the value of virtual inertia is required by system operators. Thus, once the virtual is selected, the natural frequency can be calculated by using (2.14). Consequently, the damping coefficient can also be calculated for a specified damping ratio ζ by using (2.15).

2.5 Conclusions

This chapter presents the commonly used control schemes for power converters in grid-connected applications. The main control blocks of a conventional GFL converter are reviewed. Particular focus has been paid to the introduction of the widely used current controllers and PLL scheme. Based on such basic control blocks the most popular GFM strategies are also revisited. Indeed, the majority of this chapter is devoted to analyses the

merits and demerits of the GFM strategies. The control blocks of the GFM converters are divided into different layers namely grid-synchronization, electromechanical layer, and electromagnetic layer. Mapping the control bocks of GFM strategies into these layers facilitate the understanding of the functionalities and disadvantages of each implementation from the practicality point of view. It has been shown that GFM can be implemented through emulating fully or partially the equations of an SG. Among the popular implementations, the SPC stands out as the most suitable approach for practical applications due to its simplicity and effectiveness. Finally, the parameter tuning of the SPC is provided for facilitating the development of the controllers in the subsequent chapters.

CHAPTER
3.

Robust Current Controller

In the previous chapter, the grid-supporting functionalities, such as inertia emulation and power oscillation damping, for the reviewed grid-forming approaches are designed assuming the inner control loop of the power converter is stable regardless of the grid conditions. This is, in fact, a strong assumption because the stability of these inner controllers is heavily dependent on the grid strength and voltage profile. That is, the power converter might become unstable when the short circuit ratio of the grid decreases. Aiming to design a grid-connected converter that can withstand adverse grid conditions, this chapter presents a robust sensorless current controller suitable to be used as an inner controller for the grid-forming converters. The present current controller uses only measurements of the injected current for reference tracking and grid synchronization. The three most common types of grid disturbances including impedance variation, harmonically distorted voltages, and voltage imbalance are mathematically considered in designing the current controller. In addition, the controller is optimally calculated to ensure system stability for a predefined range of system parameters. This chapter is organized as in the following. Section 3.1 reviews the existing current control schemes for a grid-connected converter. Section 3.2 presents the mathematical modelling of a power converter, which serves as a basis for the design of the robust controller in Section 3.3. The comparative simulation and experimental results are analyzed in Section 3.4 and Section 3.5. Finally, the conclusions of the chapter are given in Section 3.6. The work presented in this chapter is based on the publication "Voltage Sensorless Control Scheme Based on Extended-State Estimator for a Grid-Connected Inverter, *IEEE Transactions in Power Electronics*, 2020".

3.1 Introduction

Although most of the grid-forming control schemes focus on the improvement of the grid operation, the stability of the power converter itself plays a pivotal role in the system

as a whole. Indeed, an unstable current controller might render all the grid-supporting functionalities useless. As a primary objective, the power converters are designed to exchange the power between renewable sources or storage systems with the power grid [63], [64]. Besides the system stability, the number of sensors required for the control system of a power converter is in many cases is considered excessive [65]. That is, at least two current sensors and two grid voltage sensors are needed in conventional control schemes. Especially, additional sensors for measuring the capacitor currents are often used to prevent resonance issues associated with LCL-filter based converters [66], [67]. Such a large number of sensors increase not only the cost but the complexity of the power converter [68].

The majority of the recent control schemes proposed for the power converters try to deal with the resonances caused by the LCL filters. Even though the LCL filters are more effective in coping with switching harmonics and have smaller physical sizes, they often suffer from instabilities due to the resonance under weak grid conditions [5]. The existing approach for damping the resonances can be classified into two groups, namely, passive damping and active damping. In the former case, damping resistors are often connected in series with the filter capacitors to increase the stability margin of the converter system. Even though this approach is simple, the power loss caused by the damping resistor is unavoidable.

On the other hand, the active damping methods are more flexible and cost-effective [5]. The early works in this topic focus on the use of a digital filter to attenuate the actuation signals at the resonant frequencies [69], [70]. In recent years, full-state feedback controllers have also been used to deal with the resonances caused by the LCL filters [71], [72]. This is because the full state feedback controller can stabilize the converter system with any set of parameters. In general, full-state feedback controllers often require full measurement of all the system states. For a three-phase grid-connected converter, three voltage sensors and six current sensors might be needed for implementing a full-state feedback control scheme. To aid the selection of the controller gains for the state feedback controller, a design procedure that ensures the system robustness through the linear matrix inequality approach is studied in [73], [74]. Similarly, [75] employs the pole placement technique to enforce the performance requirements into the calculation of the feedback gains. As a more intuitive method, a virtual resistor is also used to deal with the resonance imposed by the LCL filters [76], [77].

The main drawback of the above methods is the excessive use of sensors, which increases not only the cost of the system but also the complexity of the control hardware and firmware. To alleviate such a shortcoming, voltage sensorless control schemes have

been investigated. These controllers often estimate the values of grid frequency and phase angle using only current measurements. The estimation algorithms used in these controllers fall into two groups, namely adaptive and linear approaches. As its name suggests, the former approaches make use of adaptive algorithms to estimate the grid voltages. For instance, both injected current and voltage estimation are achieved by using a single predictive controller in [68]. A combination of Kalman filter and sliding mode control are also used [78]. In this work, the grid voltage is estimated by the Kalman filter whereas the injected current is controlled by the three decoupled sliding mode controllers. Similarly, a control scheme composed of a deadbeat controller and an adaptive estimator is also presented [79]. Due to the fact that model uncertainties are taken into account in this control scheme, the system performance is improved significantly, especially under harmonically distorted voltages and low short circuit ratio. Nevertheless, the nonlinear nature of the adaptive algorithms hinders mathematical analyses of the closed-loop system. Therefore, it is not straightforward to assess the stability and robustness of the converter system.

On the other hand, stability analyses can be easily carried out in the latter case i.e. linear estimator [80], [81], [82], [83]. The linear estimator can be constructed by using change of variables or by using state observer. That is, a change of variables is used to make it possible for calculating the grid voltage from the new set of variables. In the new coordinate, the observer dynamics and the system parameter uncertainly can be dealt with separately. However, this approach has only been tested with the ideal grid voltage. Inspired by the control system of electrical machines, an estimation method based on the virtual flux concept is presented in [83]. These early works demonstrated the potential of linear estimators. However, the stability of the converter system has not been investigated as a whole. Moreover, as the dynamics of the controller and the estimators are often coupled, it is necessary to consider simultaneously both of these control functions in the design of the converter system.

From a control perspective, the above concerns can be addressed using the extended-state estimator. That is, the state-space model of the system can be extended to contain also the states of the disturbance, thus transforming two coupled design processes, i.e. designing controller and estimator, into a single feedback regulator problem. As a consequence, the tracking and robustness problem can be dealt with effectively using proven control design techniques. In this line of work, [84] investigated the use of the internal model principle (IMP) to construct the disturbance model such that it can be readily added into the state-space equation of the system. The estimated disturbance is then used as a feedforward term to cancel out the effect of the actual disturbance to achieve asymptotic tracking of the reference signal. Because most of the systems states and disturbances can be estimated

using the extended-state estimator, many of the sensors in the system become redundant. As a consequence, the extended-state estimator approach has been widely known in the control community [85], [86]. The recent adaptation of the extended-state estimator to eliminate the need for the grid voltage sensors in power converters have also been reported in [82]. In this work, the extended-state estimator is employed to estimate the grid voltages to facilitate the current control loop. In addition to the ability to deal with grid voltage imbalance, it is apparent from [82] that the order of the closed-loop system is directly proportional to the dynamics of the disturbance. This, however, poses a challenge in tuning the feedback gain of the system due to the high number of gains needed to be selected in order to ensure not only the system performance but also its robustness.

Aiming to design a complete framework for the current control loop of a grid-forming controller, this chapter presents a robust voltage-sensorless controller (RVSC) where only the measurements of the grid-side current sensors are required. The voltage sensorless controller consists of a state feedback regulator and an extended-sate estimator. The RVSC takes into account voltage distortion and grid impedance variation in the design of the controller gains. In fact, the voltage harmonic distortions are modelled in a form of state-space equations by using IMP, whereas the grid impedance is incorporated by transforming the system equations into a polytopic form. The complete model of the RVS allows the calculation of feedback gain to be optimized using the LMI approach.

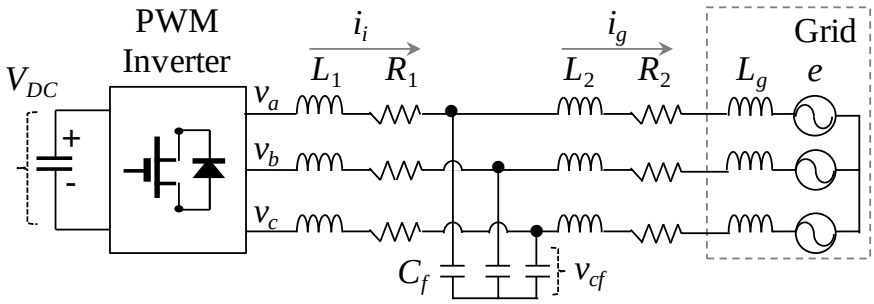

Fig. 3.1. Power circuit of a three-phase inverter with LCL-filters.

3.2 Modelling of a Grid-connected Converter

To facilitate the design and tuning of the RVSC, it is essential to obtain the state-space model of the power converter. Without loss of genericity, a three-phase LCL-filtered power converter is considered. The power circuit of the converter is shown in Fig. 3.1 in which R_1 and R_2 are the filter resistances, L_1 and L_2 are the filter inductances, C_f is the filter

capacitance. The grid inductance is represented by an equivalent one L_g. It is assumed that the resistance of the capacitor is negligible.

From Fig. 3.1, Kirchhoff's voltage equation of the power converter can be obtained as in the following:

$$\frac{di_i^{abc}(t)}{dt} = \frac{v_c^{abc}(t) - v_{cf}^{abc}(t)}{L_1} - \frac{R_1}{L_1} i_i^{abc}(t), \tag{3.1}$$

$$\frac{dv_{cf}^{abc}(t)}{dt} = \frac{i_i^{abc}(t) - i_2^{abc}(t)}{C_f}, \tag{3.2}$$

$$\frac{di_g^{abc}(t)}{dt} = \frac{v_{cf}^{abc}(t) - e_g^{abc}(t)}{L_2} - \frac{R_2}{L_2} i_g^{abc}(t), \tag{3.3}$$

where v_c, i_i, v_{cf}, i_g, and e_g are the converter output voltage, the converter-side current, the capacitor voltage, the grid-side current, and the grid voltage. The superscript *abc* denotes that these variables are in the natural reference frame. In fact, each of the equations above represents a set of three equations for the three electrical phases. To reduce the number of the equation needed to be dealt with in the control design and analyses, the equation (3.1), (3.2), and (3.3) can be transformed into the stationary reference frame using Clarke transformation as follows:

$$\frac{di_i^{\alpha\beta}(t)}{dt} = \frac{v_c^{\alpha\beta}(t) - v_{cf}^{\alpha\beta}(t)}{L_1} - \frac{R_1}{L_1} i_i^{\alpha\beta}(t), \tag{3.4}$$

$$\frac{dv_{cf}^{\alpha\beta}(t)}{dt} = \frac{i_i^{\alpha\beta}(t) - i_2^{\alpha\beta}(t)}{C_f}, \tag{3.5}$$

$$\frac{di_g^{\alpha\beta}(t)}{dt} = \frac{v_{cf}^{\alpha\beta}(t) - v_g^{\alpha\beta}(t)}{L_2} - \frac{R_2}{L_2} i_g^{\alpha\beta}(t), \tag{3.6}$$

where the superscript $\alpha\beta$ denotes that variables are in the stationary reference frame. Because the equations in the stationary reference frame are identical for $\alpha-$axis and $\beta-$axis, they can be decoupled and treated independently. Therefore, only one of the equations is taken into constructing the state-space equation. For the sake of simplicity, the superscript $\alpha\beta$ will be omitted. The state equations of the power converter system can be derived from (3.4), (3.5), and (3.6) as

$$\dot{\mathbf{x}}_c(t) = \mathbf{A}_c \mathbf{x}_c(t) + \mathbf{B}_c u_c(t) + \mathbf{B}_{dc} w_c(t), \tag{3.7}$$

$$y_c(t) = \mathbf{C}_c \mathbf{x}_c(t), \tag{3.8}$$

where $\mathbf{x}_c = [i_i \quad v_{cf} \quad i_g]^T$, $u_c = v_c$, $w_c = e$, and the matrices are given by

$$\mathbf{A}_c = \begin{bmatrix} -R_1/L_1 & -1/L_1 & 0 \\ 1/C_f & 0 & -1/C_f \\ 0 & 1/(L_2+L_g) & -R_2/(L_2+L_g) \end{bmatrix}, \tag{3.9}$$

$$\mathbf{B}_c = \begin{bmatrix} 1/L_1 \\ 0 \\ 0 \end{bmatrix}, \tag{3.10}$$

$$\mathbf{B}_{dc} = \begin{bmatrix} 0 \\ 0 \\ -1/(L_2+L_g) \end{bmatrix}, \tag{3.11}$$

$$\mathbf{C}_c = \begin{bmatrix} 0 & 0 & 1 \end{bmatrix}. \tag{3.12}$$

To facilitate the implementation of the controller in digital microprocessors, the continuous-time equations in (3.7) and (3.8) can be discretized using the zero-order-hold approach [87]. The equivalent discrete-time state equations of the power converters can be obtained as in the following.

$$\begin{bmatrix} \mathbf{x}_{dis}(k+1) \\ x_\varphi(k+1) \end{bmatrix} = \begin{bmatrix} \mathbf{A}_{dis} & \mathbf{B}_{dis} \\ \mathbf{0} & 0 \end{bmatrix} \begin{bmatrix} \mathbf{x}_{dis}(k) \\ x_\varphi(k) \end{bmatrix} + \begin{bmatrix} \mathbf{0} \\ 1 \end{bmatrix} u(k) + \begin{bmatrix} \mathbf{B}_{ddis} \\ 0 \end{bmatrix} w(k), \tag{3.13}$$

$$y(k) = \begin{bmatrix} \mathbf{C}_c & 0 \end{bmatrix} \begin{bmatrix} \mathbf{x}_{dis}(k) \\ x_\varphi(k) \end{bmatrix}, \tag{3.14}$$

where $\mathbf{A}_{dis} = e^{\mathbf{A}_c T_s}$, $\mathbf{B}_{dis} = \int_0^{T_s} e^{\mathbf{A}_c \eta} d\eta \cdot \mathbf{B}_c$, $\mathbf{B}_{ddis} = \int_0^{T_s} e^{\mathbf{A}_c \eta} d\eta \cdot \mathbf{B}_{dc}$, $\mathbf{0}$ is a zero matrix with appropriate dimension, the variables $\mathbf{x}_{dis}(k)$, $u(k)$, $w(k)$, $y(k)$ are the discrete-time counterpart of $\mathbf{x}_c(t)$, $u_c(t)$, $w_c(t)$, $y_c(t)$, respectively. The dummy state x_ϕ is added to model one sample period delay in the control input signal *u* introduced by the PWM implementation. The system in (3.13) and (3.14) can be rewritten concisely as

$$\mathbf{x}(k+1) = \mathbf{A}\mathbf{x}(k) + \mathbf{B}u(k) + \mathbf{B}_d w(k), \tag{3.15}$$

$$y(k) = \mathbf{C}\mathbf{x}(k). \tag{3.16}$$

3.3 Robust Voltage Sensorless Controller

This section presents the main building blocks of the RVSC. From a control point of view, the RVSC is composed of two parts, namely the state-feedback regulator and the extended state observer. The overall block diagram of the RVSC is shown in Fig. 3.2. The extended state observer uses the measurement of the injected current to estimate system states as well as the grid-voltage states. The system states are then employed for the regulator while the grid voltage states are feedforwarded to the control input as a compensation component to cancel out the effect of the actual grid voltage. The estimated grid voltages are also used as inputs for the SRF-PLL to obtain the grid angles which are used to generate the references for the injected currents. In the following subsections, the formulation and design of these control blocks are explained in detail.

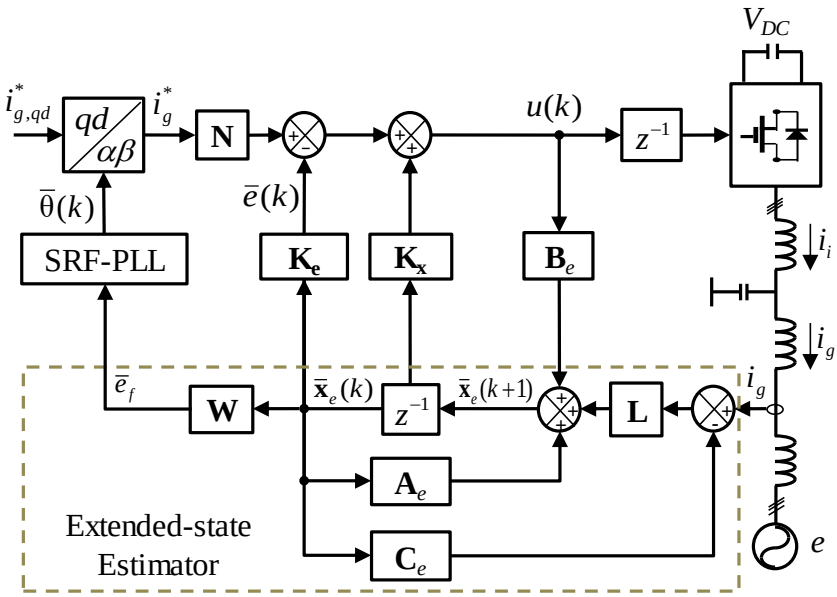

Fig. 3.2. Block diagram of the proposed control scheme.

3.3.1 State Feedback Regulator

The main objective of the state-feedback regulator is to stabilize the system i.e. forcing the system into an equilibrium state. In this particular case, as the system is linear, the equilibrium state coincides with an operating point that all the states are zero. In addition, the regulator also plays an important role in shaping the dynamic response of the closed-loop system. Considering that the grid impedance can vary during operation, it is necessary to take into account such variation in selecting the parameters for the controller such that the system is stable for a predefined range of the grid impedance. For this purpose, the state

equation (3.15) can be rewritten in a polytopic form to include the uncertainties in the grid impedance as follows [6]:

$$\mathbf{x}(k+1) = \mathbf{A}(\alpha)\mathbf{x}(k) + \mathbf{B}u(k) + \mathbf{B}_d(\alpha)w(k), \tag{3.17}$$

where

$$(\mathbf{A}, \mathbf{B}_d)(\alpha) = \sum_{j=1}^{2} \alpha_j (\mathbf{A}, \mathbf{B}_d)_j, \sum_{j=1}^{2} \alpha_j = 1, \ \alpha_j \geq 0, \ \ j = 1,2. \tag{3.18}$$

The vertex matrices in (3.18) can be calculated by substituting the maximum and minimum values of L_g into the matrices $(\mathbf{A}, \mathbf{B}_d)(\alpha)$. Remark that the values of L_g directly reflect the impedance of the grid.

To stabilize the converter system for a range of grid impedance, a full state feedback regulator is used in the RVSC. Considering the system described in (3.17), the input signals provided by the regular can be formalized as follows:

$$u(k) = \mathbf{K}\mathbf{x}(k). \tag{3.19}$$

Substituting (3.19) into (3.17), the state equation of the converter system can now be rewritten as:

$$\mathbf{x}(k+1) = (\mathbf{A}(\alpha) + \mathbf{B}\mathbf{K})\mathbf{x}(k) + \mathbf{B}_d(\alpha)w(k), \tag{3.20}$$

$$y(k) = \mathbf{C}\mathbf{x}(k). \tag{3.21}$$

With regard to the system stability, the system in (3.20) is considered stable if, and only if, the below inequalities hold [30].

$$\begin{bmatrix} \varepsilon^2 \mathbf{Q} & (\mathbf{A}_j \mathbf{Q} + \mathbf{B}\mathbf{Y})^T \\ \mathbf{A}_j \mathbf{Q} + \mathbf{B}\mathbf{Y} & \mathbf{Q} \end{bmatrix} > 0 \ \text{ and } \ \mathbf{Q} > 0, \tag{3.22}$$

where $\mathbf{Q} \in \Re^{4\times4}$ is a positive-definite matrix, $\varepsilon \in (0,1)$ is the decay rate which dictates the dynamic behavior of the system states and $\mathbf{Y} = \mathbf{K}\mathbf{Q}$. In fact, the higher the decay rate the faster the system states converge to zero.

To achieve the fastest convergent speed for the chosen decay rate and the variation in grid impedance, the feedback gain $\mathbf{K}$ can be calculated from the below LMI optimization problem.

$$\underset{\varepsilon>0}{\text{Minimize}} \quad \mathbf{Q} \quad \text{subject to } (5.22). \tag{3.23}$$

In (3.23), $\mathbf{A}_j$ is calculated by using (3.18), and ε is desired decay rate. The matrices $\mathbf{Y}$ and $\mathbf{Q}$ can be obtained by using an LMI solver e.g. LMI control Toolbox in MATLAB [31]. Then, the feedback gain vector can be evaluated as $\mathbf{K} = \mathbf{YQ}^{-1}$.

3.3.2 Extended-state Estimator

The main focus of the extended-state estimator is to provide the current controller with good disturbance rejection capability. In other words, one of the main uses of the extended states is to cancel out the influence of the grid voltages on the injected currents. In fact, the grid voltage will be estimated and used as a feedforward term for the RVSC to counteract the actual grid voltages. Due to the fact that both $\mathbf{B}_d$ (α) and $w(k)$ in (3.17) contain uncertainties, it is more convenient to use the equivalent quantities to mathematically represent these two terms [87]. Since the estimated grid voltage will enter the system as an input signal rather than a disturbance signal, the estimated grid voltage must obey the following equality in order to fulfil the disturbance rejection requirement.

$$\mathbf{B}_d w(k) = \mathbf{B} w_e(k) . \tag{3.24}$$

Substituting (3.24) into (3.17) yields:

$$\mathbf{x}(k+1) = \mathbf{A}(\alpha)\mathbf{x}(k) + \mathbf{B}(u(k) + w_e(k)) , \tag{3.25}$$

where w_e is the equivalent term for the grid voltage.

Even though the magnitude and phase of the equivalent grid voltage w_e can vary during operation, the frequency of w_e or in other words the frequency of the grid only varies slightly in most cases. Considering that the grid voltages contain not only the fundamental component but also harmonics, the grid voltages can be mathematically modelled as follows:

$$\dot{\mathbf{x}}_{weci}(t) = \mathbf{F}_{ci}\mathbf{x}_{weci}(t) , \tag{3.26}$$

$$w_{eci}(t) = \mathbf{H}_i \mathbf{x}_{weci}(t) , \tag{3.27}$$

where $\mathbf{x}_{weci} \in \Re^{2\times 1}$ being the state vector of the grid voltage model, the parameter matrices are:

$$\mathbf{F}_{ci} = \begin{bmatrix} 0 & 1 \\ -\omega_i^2 & 0 \end{bmatrix}, \quad \mathbf{H}_i = \begin{bmatrix} 1 \\ 0 \end{bmatrix}^T , \tag{3.28}$$

and the subscript $i=(6k\pm1)^{\text{th}}$, with k being a non-negative integer, indicates the order of the component whose angular frequency is ω_i. By employing the state equation given in (3.26) and (3.27), any order of grid voltage harmonics can be described as:

$$\dot{\mathbf{x}}_{wec}(t)=\mathbf{F}_c\mathbf{x}_{wec}(t), \tag{3.29}$$

$$w_{ec}(t)=\mathbf{H}\mathbf{x}_{wec}(t). \tag{3.30}$$

where:

$$\mathbf{x}_{wec}=\begin{bmatrix}\mathbf{x}_{wec1}\\ \vdots\\ \mathbf{x}_{weci}\\ \vdots\end{bmatrix},\ \mathbf{F}_c=\begin{bmatrix}\mathbf{F}_{c1} & & & \\ & \ddots & & \\ & & \mathbf{F}_{ci} & \\ & & & \ddots\end{bmatrix},\ \mathbf{H}=\begin{bmatrix}\mathbf{H}_1^T\\ \vdots\\ \mathbf{H}_i^T\\ \vdots\end{bmatrix}^T. \tag{3.31}$$

The discrete-time counterpart of (3.29) and (3.30) can be derived as:

$$\mathbf{x}_{we}(k+1)=\mathbf{F}_d\mathbf{x}_{we}(k), \tag{3.32}$$

$$w_e(k)=\mathbf{H}\mathbf{x}_{we}(k), \tag{3.33}$$

where $\mathbf{F}_d=e^{\mathbf{F}_cT_s}$. To form the extended-state estimator, the grid voltage equation in (3.32) and (3.33) can be added to the converter equation in (3.16) and (3.25) as

$$\begin{bmatrix}\mathbf{x}(k+1)\\ \mathbf{x}_{we}(k+1)\end{bmatrix}=\begin{bmatrix}\mathbf{A}(\alpha) & \mathbf{BH}\\ \mathbf{0} & \mathbf{F}_d\end{bmatrix}\begin{bmatrix}\mathbf{x}(k)\\ \mathbf{x}_{we}(k)\end{bmatrix}+\begin{bmatrix}\mathbf{B}\\ \mathbf{0}\end{bmatrix}u(k), \tag{3.34}$$

$$y(k)=[\mathbf{C}\quad\mathbf{0}]\begin{bmatrix}\mathbf{x}(k)\\ \mathbf{x}_{we}(k)\end{bmatrix}. \tag{3.35}$$

Equations (3.34) and (3.35) can be concisely rewritten as in the following.

$$\mathbf{x}_e(k+1)=\mathbf{A}_e(\alpha)\mathbf{x}_e(k)+\mathbf{B}_eu(k), \tag{3.36}$$

$$y(k)=\mathbf{C}_e\mathbf{x}_e(k). \tag{3.37}$$

A Luenberger observer can be constructed to estimate the states of the extended-state model from the inverter reference voltage $u(k)$ and the grid-side current measurement $y(k)$ as follows:

$$\bar{\mathbf{x}}_e(k+1)=\mathbf{A}_e(\alpha)\bar{\mathbf{x}}_e(k)+\mathbf{B}_eu(k)+\mathbf{L}(\mathbf{C}_e\bar{\mathbf{x}}_e(k)-y(k)), \tag{3.38}$$

where $\bar{\mathbf{x}}_e(k)$ is the estimated state and $\mathbf{L}$ denotes the estimator gain. The estimation error $\tilde{\mathbf{x}}_e(k) = \mathbf{x}_e(k) - \bar{\mathbf{x}}_e(k)$ can be obtained by subtracting (3.38) from (3.36) as:

$$\tilde{\mathbf{x}}_e(k+1) = (\mathbf{A}_e(\alpha) + \mathbf{L}\mathbf{C}_e)\tilde{\mathbf{x}}_e(k)\,. \tag{3.39}$$

The estimator gain can also be optimally calculated following the procedure used to obtain $\mathbf{K}$ in the preceding sub-section (3.39). That is, the stability condition for the extended-state estimator in (3.38) is:

$$\begin{bmatrix} \varepsilon_e^2\mathbf{Q}_e & \mathbf{Q}_e\mathbf{A}_{ej} + \mathbf{Y}_e\mathbf{C}_e \\ (\mathbf{Q}_e\mathbf{A}_{ej} + \mathbf{Y}_e\mathbf{C}_e)^T & \mathbf{Q}_e \end{bmatrix} > 0 \text{ and } \mathbf{Q}_e > 0\,, \tag{3.40}$$

where $\mathbf{Y}_e = \mathbf{Q}_e\mathbf{L}$, and $\varepsilon_e \in (0,1)$ is the convergent speed of the estimator states. The matrices $\mathbf{Q}_e$ and $\mathbf{Y}_e$ can be obtained by computing the following LMI optimization problem:

$$\underset{\varepsilon_e>0}{\text{Minimize}} \quad \mathbf{Q}_e \quad \text{subject to (30)}\,. \tag{3.41}$$

Similarly, the estimator gain can be calculated as $\mathbf{L} = \mathbf{Q}_e^{-1}\mathbf{Y}_e$. It is necessary to mention that implementing a parameter-varying estimator in (3.38) is unrealistic. Thus, it is important to fine constant system matrices for the estimator. Such system matrices should ensure that the closed-loop system is stable with calculated gain **K** and **L.** To assess the stability of the closed-loop system including the state-feedback regular, the extended-state estimator and the feedforward grid voltage $\bar{e}(k)$ can be augmented from (3.19), (3.38), and Fig. 3.2 as follows:

$$\begin{bmatrix} \mathbf{x}(k+1) \\ \bar{\mathbf{x}}_e(k+1) \end{bmatrix} = \begin{bmatrix} \mathbf{A}(\boldsymbol{\alpha}) & \mathbf{B}(\mathbf{K}_x - \mathbf{K}_e) \\ -\mathbf{L}\mathbf{C} & \mathbf{A}_e + \mathbf{B}_e(\mathbf{K}_x - \mathbf{K}_e) + \mathbf{L}\mathbf{C}_e \end{bmatrix} \begin{bmatrix} \mathbf{x}(k) \\ \bar{\mathbf{x}}_e(k) \end{bmatrix} + \begin{bmatrix} \mathbf{B} \\ \mathbf{B}_e \end{bmatrix} \mathbf{N}r(k) + \begin{bmatrix} \mathbf{B} \\ \mathbf{0} \end{bmatrix} w_e(k)\,, \tag{3.42}$$

where $\mathbf{K}_x = [\mathbf{K} \quad \mathbf{0}]$, $\mathbf{K}_e = [\mathbf{0} \quad \mathbf{H}]$, r is the reference current, and $\mathbf{N}$ is a feedforward gain.

Fig. 3.3 shows the flow chart diagram that summarizes the steps proposed to find the system matrices for the extended-state estimator. As shown, the regulator and estimator gains are first computed using the LMI approach. Then, different values of grid inductance L_g is used to evaluate the stability of the system in (3.42). The grid inductance will be varied from its minimum value to its maximum value with a deviation of ΔL_g for every iteration. In each iteration, the stability of the closed-loop system (3.42) is checked by simply monitoring the real part of the eigenvalues. The governing principle of this design procedure is based on the stability condition for polytopic linear time-invariant systems [88]. As stated in [88], the system in (3.42) is robustly stable in the uncertain domain (3.18) if, and only if,

the stability holds at the vertexes of the uncertain domain. For constructing the estimator, any valid value of L_{ge} can be used.

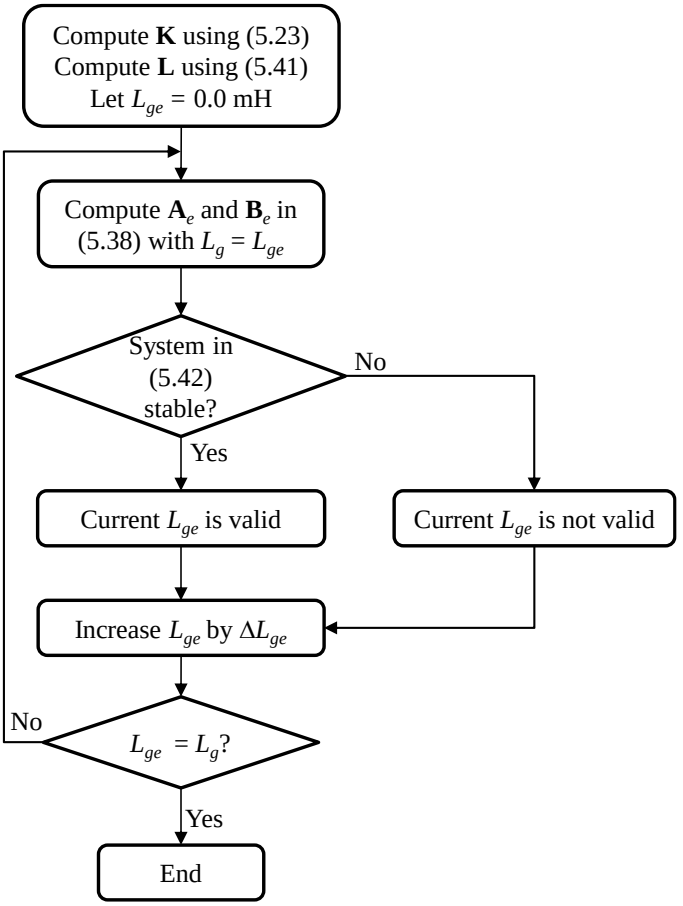

Fig. 3.3. Proposed design procedure of determining grid impedance values in the implementation of extended-state estimator to ensure a stable closed-loop system.

To demonstrate the above design procedure, a three-phase power converter described in Table 3.1 is considered. As for the grid voltage, harmonics of 5th, 7th, and 11th order are taken into account. For the first calculation step, the regulator and estimator gains are computed for the decay rates of $\varepsilon = 0.6$ and $\varepsilon_e = 0.985$, respectively. For selecting a proper decay rate, it is worth mentioning that the convergent speed of the system is inversely proportional to the decay rate. That is, the lower the decay rate results in the higher the system bandwidth. Logically, the stability margin of the system also reduces as the system bandwidth increases. Once **K** and **L** are obtained, the remaining steps can be literately

computed to obtain the range of L_{ge} for constructing the estimator. For the given design parameters, the valid inductance values are calculated as $L_{ge} \in [0.2, 0.9]\,\text{mH}$.

Table 3.1. Parameters of the three-phase inverter

Symbol	Quantity		Value
P	Nominal inverter power		2.5kVA
E	Nominal grid line-line voltage		220V
f_g	Nominal grid frequency		60Hz
V_{DC}	DC-link voltage		400V
R_1/R_2	Filter resistance		0.5/0.3Ω
L_1/L_2	Filter inductance		1.7/0.9mH
C_f	Filter capacitance		4.5μF
L_g	Grid inductance:	Min.	0.0mH
		Max.	0.9mH

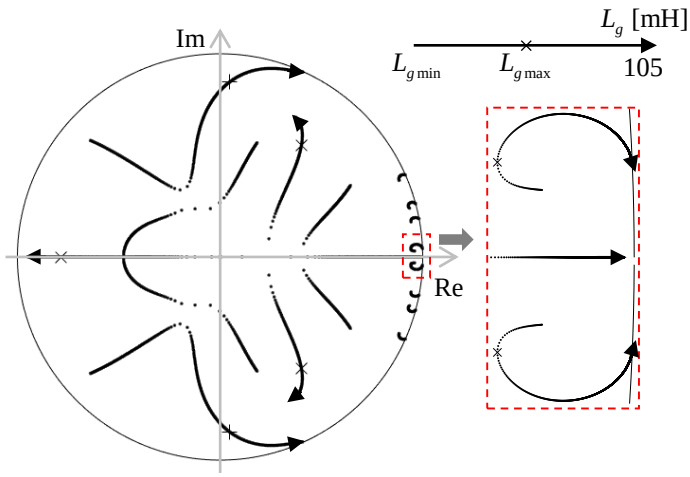

Fig. 3.4. Eigenvalue map of the closed-loop system when L_g varies from 0 to 105 mH.

The stability of the closed-loop system can be numerically validated by using the root locus method. Fig. 3.4 shows the root loci of the closed-loop system described in (3.42) for different values of L_g. It is shown that, as the grid inductance increases, some of the eigenvalues move closer to the boundary of the unit circle. Indeed, the system becomes unstable as soon as the grid inductance surpass $L_g = 105\,\text{mH}$. Regardless, for the predefined range of grid inductance $L_g = [0-9]\,\text{mH}$, the system remains stable. This result validates the robustness of the proposed control scheme again the variation in the grid inductance.

3.3.3 Reference Tracking and Grid Synchronization

The above procedure ensures that any influence of the grid voltage on the injected current is asymptotically rejected by employing estimated grid voltage. Indeed, the state space equation of the controller depicted in Fig. 3.2 can be derived as in (3.43).

$$\mathbf{x}(k+1) = \mathbf{A}(\boldsymbol{\alpha})\mathbf{x}(k) + \mathbf{B}\mathbf{K}\bar{\mathbf{x}}(k) - \mathbf{B}\bar{w}_e(k) + \mathbf{B}\mathbf{N}r(k) + \mathbf{B}w_e(k) \tag{3.43}$$

It is obvious from (3.43) that the system states are decoupled from the grid voltage in the steady-state where the estimated grid voltage is identical to the real grid voltage $\bar{w}_{e\infty} = w_{e\infty}$. In fact, feeding back estimated grid voltage cancels out the effect of not only the grid voltage but also parameter variation. In this regard, Fig. 3.5 shows that the gain and phase of the closed-loop system at the targeted frequencies remain constant for different values of L_g. In many cases, the strength of the grid is indicated by the short-circuit ratio instead of the grid inductance.

The short-circuit ratio can be calculated from the grid inductance by using the following formula:

$$SCR = \frac{1}{L_g \omega_g} \cdot \frac{q}{\sqrt{1+q^2}} \cdot \frac{E^2}{P}, \tag{3.44}$$

where q denotes the *X/R* ratio of the grid impedance.

Because the gain and phase of the RVSC-controlled power converter are completely decoupled from the grid voltage and inductance variation in the steady-state, the feedforward gain **N** can be calculated such that the closed-loop system exhibit a unity gain and zero phase delay at the fundamental frequency the grid. For the converter system described in Table 3.1, the feedforward gain **N** can be calculated from (3.43) at the fundamental frequency as follows:

$$\mathbf{N} = \frac{1}{0.1062} \angle -(-7.0779\,^\circ) = 9.4162 \angle 7.0779^\circ. \tag{3.45}$$

Instead of the measured grid voltage, the estimated grid voltage can be used to obtain the grid phase angle which is needed to generate the references for the injected currents. In fact, it is even more advantageous to use the estimated voltage because the voltage components are separated. That is, the estimator acts as a series of band-pass filters which separate the grid voltage into fundamental and harmonic components. For the PLL, it is

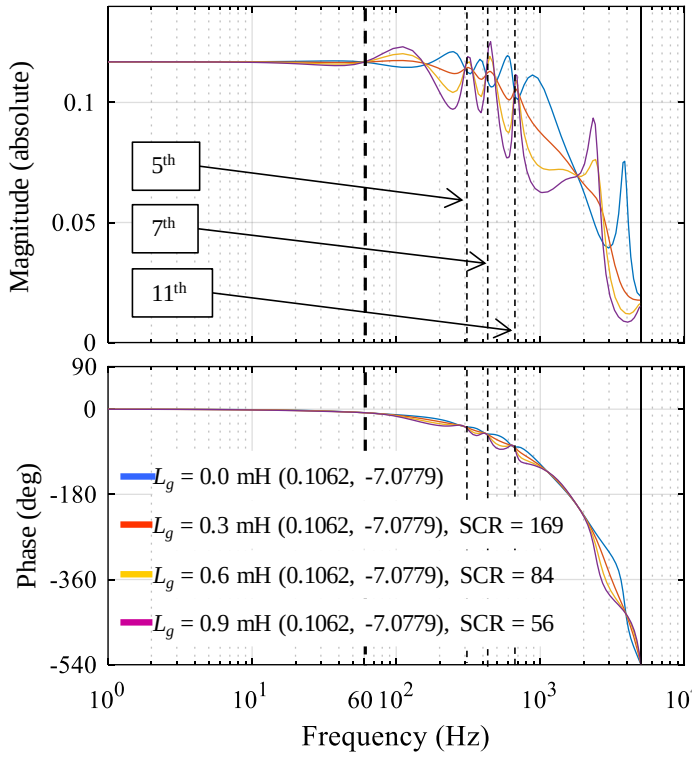

Fig. 3.5. Frequency responses of the closed-loop system in (32) when $N=1$, $w_e=0$, and $L_g=\{0.0, 0.3, 0.6, 0.9\}$ mH. Values in parentheses indicate the magnitude gain and phase delay of corresponding response at 60 Hz.

to use only the fundamental component. Thus, the PLL will not be affected by the harmonic voltages. As a result, a conventional SRF-PLL [89] can be used in conjunction with the RVSC even if the grid voltage is highly distorted. The fundamental component of the grid voltage can be extracted from the estimated states by using (3.46)

$$\bar{e}_f = \mathbf{W}\bar{\mathbf{x}}_e, \tag{3.46}$$

where $\mathbf{W}=[\mathbf{0}^{1\times4} \quad -1 \quad \mathbf{0}^{1\times7}]$.

In the steady-state where $\bar{w}_{e\infty}=w_{e\infty}$, Equation (3.43) can be simplified as:

$$\mathbf{x}(k+1)=\mathbf{A}(\boldsymbol{\alpha})\mathbf{x}(k)+\mathbf{BK}\bar{\mathbf{x}}(k)+\mathbf{BN}r(k). \tag{3.47}$$

Equation (3.47) implies that the RSVC is completely not affected by the grid voltage in the steady-state. Furthermore, the effect on the variation in grid inductance is also taken into account as an input parameter in section 5.3.1 and section 5.3.2. As a consequence, the

RSVC is capable of coping with grid voltage disturbances as well as grid inductance variation.

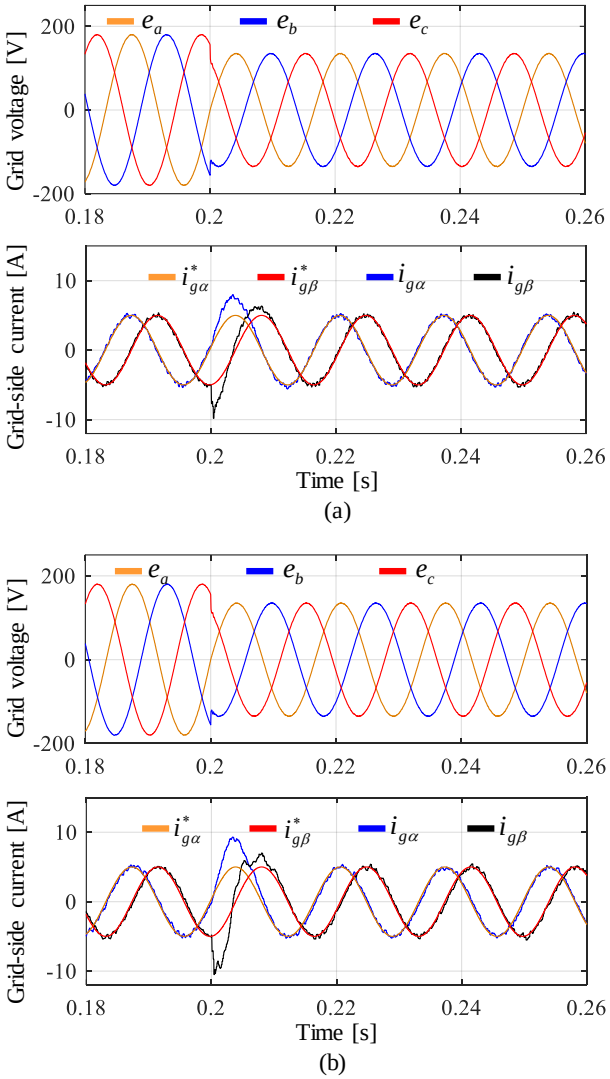

Fig. 3.6. Simulation results under grid voltage dip of 25% at t = 0.2 s. (a) Control scheme presented in [82]. (b) Proposed control scheme.

3.4 Simulation Results

To validate the performance of the RVSC, simulations using PSIM software have been conducted. The parameters of the power converter are given in Table 3.1. Decay rates and other control parameters of the regulator and the estimators are identical to those calculated

in section 5.3. Two grid voltage profiles are used in the following simulations: (1) ideal grid voltage, (2) unbalanced and harmonically distorted grid voltage. In the latter profile, there is a 20% reduction in the *a*-phase voltage and all the phases are polluted with 5th, 7th, and 11th harmonics of 10%, 10%, and 5% of the nominal magnitude. The total harmonic distortion (THD) value of the abnormal voltage profile is 15%.

To highlight the performance of the RVSC over existing controllers, the controller reported in [82] is also adopted for comparisons. Fig. 3.6 shows the simulation results of both control schemes in an event of a grid voltage dip of 25%. It is clear that the two controllers show similar transient responses in the injected currents. Upon the occurrence of the event, the two controllers took about 10 ms to bring the power converters back to a steady state. Also, there is a peak in the injected currents. However, such an overshot is still within acceptable limits.

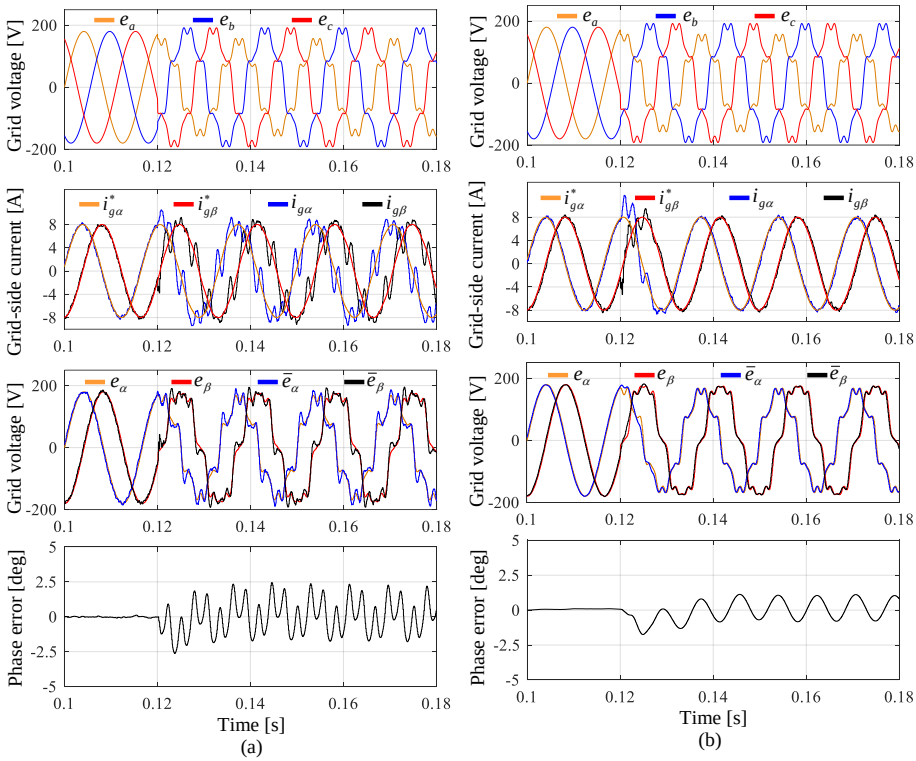

Fig. 3.7. Simulation results for control and estimation performance under the grid voltage change at t = 0.12 s. (a) Control scheme presented in [23]. (b) Proposed control scheme.

Fig. 3.7 shows the response of the two controllers under unbalanced and distorted grid voltages. As shown in Fig. 3.7a, as the grid voltages are superimposed with unbalanced and

distorted components at t = 0.2 seconds, the grid-side currents become unacceptably distorted in the case of the controller in [82]. Because the distorted current is highly distorted, the estimated voltages are also noticeably affected. This shortcoming of the controller in [82] is even more visible in the error in the bottom waveform. On the other hand, as shown in Fig. 3.7b, the RVSC can effectively deal with the harmonics in the grid voltage on the injected current with a transient period of approximately 15 ms. Such a good disturbance rejection capability of the RVSC is obtained by the incorporation of the grid model in the controller.

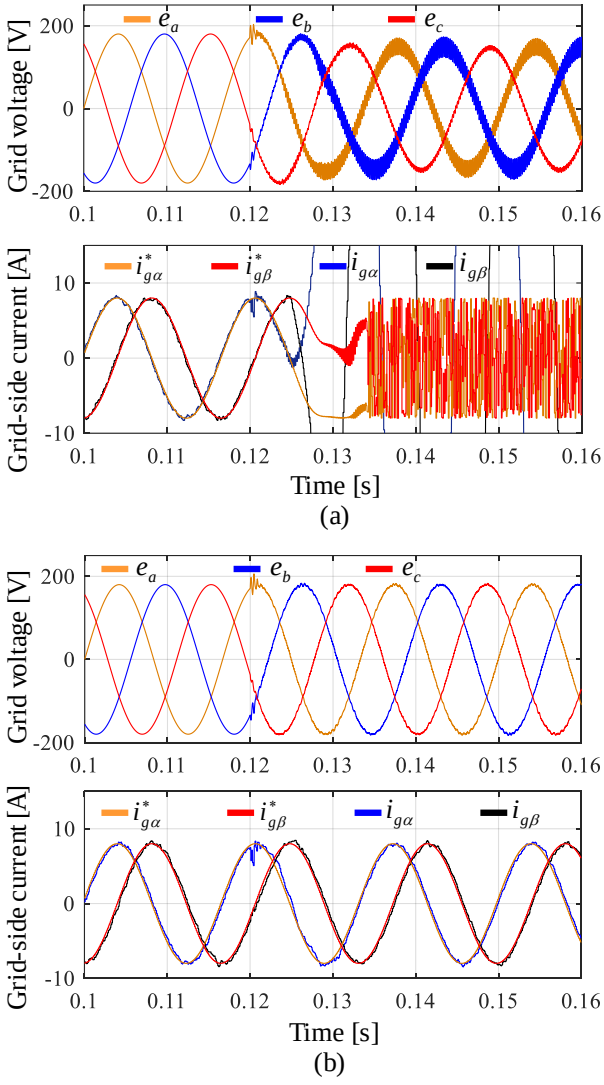

Fig. 3.8. Simulation results for control performance under the grid impedance change at t = 0.12 s. (a) Control scheme presented in [23]. (b) Proposed control scheme.

In a similar way, Fig. 3.8 shows the performance comparison of the two control controllers when there is a sudden change in grid inductance at 0.12 seconds. As can be seen from Fig. 3.8a, the controller in [82] is not able to stabilize the power converter under such a condition. However, as demonstrated in Fig. 3.8b, such a variation in grid inductance merely affects the operation of the converter when the RVSC is used. In fact, the converter currents only suffer considerably short transience. This property of the RVSC is achieved by using the LMI approach to consider the variation of the grid inductance in the design of the RVSC.

In comparison to the existing controller, the proposed scheme provides better control performance in case of distorted grid voltage and parameter variation. The shortcoming of the existing controller to cope with abnormal grid voltage is because the proportional resonant (PR) controller and the estimator consider only the fundamental frequency component [82]. As a result, the existing controller is not able to eliminate the harmonic component in the injected currents. Furthermore, the variation in grid inductance was not taken into account in [82]. In fact, the ability to deal with parameter variation in [82] is merely a by-product effect instead of a design criterion. On the contrary, as demonstrated in section 3.3, both the abnormal voltage and parameter uncertainties are considered as design inputs in the RVSC. That is, the parameter variation is taken into account in the proposed controller by using the polytopic representation and LMI-based tuning technique. In addition, the grid voltage abnormality is modelled by using the IMP approach as shown from (3.29) to (3.35). As a result, the RVSC can withstand both the grid inductance variation and adverse grid voltage. Concretely, the ability to cope simultaneously with different types of uncertainties sets the RVSC apart from the existing controllers.

3.5 Experimental Results

To further validate the practicality of the proposed control scheme, the experiments using a three-phase 2.5 kVA prototype grid-connected inverter have been performed. The prototype grid-connected inverter is implemented using an intelligent power module (IPM) PM50RL1A120 with the turn-on and turn-off dead times of 1 μs within the DSP. The system parameters, the control gains, and the grid conditions are the same as those used in the simulations. The entire control scheme is implemented using 32-bit floating-point DSP TMS320F28335 with a clock frequency of 150 MHz. The sampling and switching frequencies are chosen as 10 kHz. To emulate the grid, a three-phase programmable AC power source (PACIFIC Power Source 320-ASX) is connected to the filters through a transformer (PACIFIC M99211).

Fig. 3.9 shows experimental waveforms of the proposed control scheme during the start-up process which is one of the most critical tasks faced by voltage sensorless control schemes. As can be seen from Fig. 3.9, it takes about 30 ms for the estimated grid voltages to reach the actual values. Such transience can also be obtained from the estimated grid voltage angle. The waveforms of grid-side currents confirm a stable inverter operation during the start-up process.

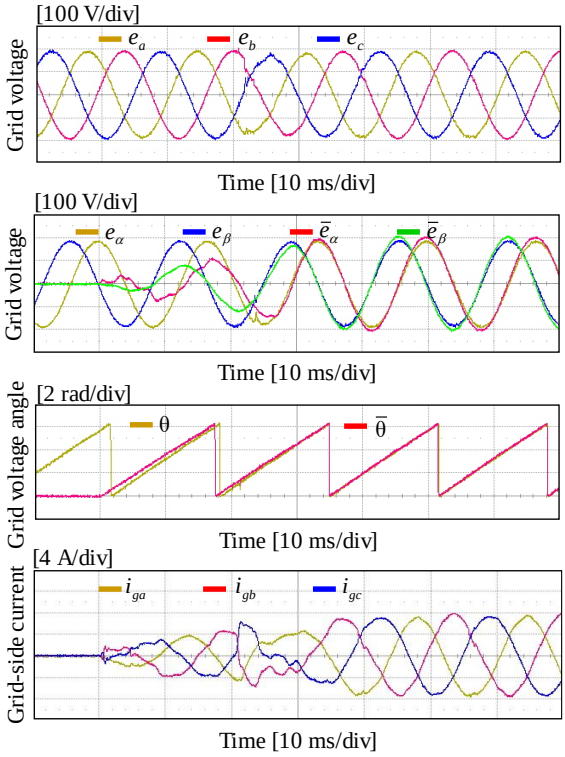

Fig. 3.9. Experimental results of the proposed control scheme during start-up process.

Fig. 3.10 shows the experimental results of the proposed control scheme when the ideal grid voltages are suddenly changed into unbalanced and distorted voltages and Fig. 3.11 shows the experimental results when there is a step-change in reference currents under an unbalanced and distorted grid. All the experimental results are well-matched with the simulation waveforms in Fig. 3.7. It is confirmed from these experimental results that the proposed voltage sensorless control scheme which uses only the grid-side current measurements operates stably as well as effectively even in such a severe grid environment.

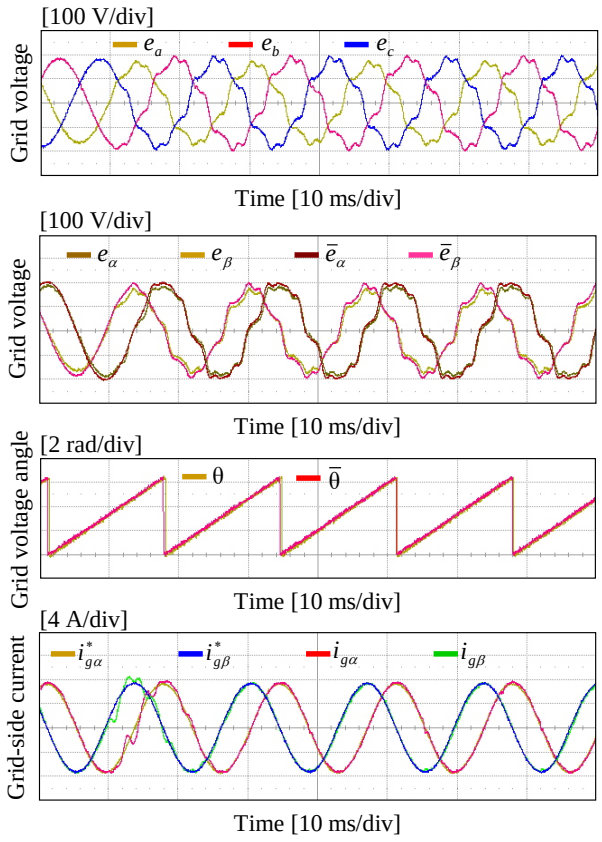

Fig. 3.10. Experimental results of the proposed control scheme when the grid voltage changes from the ideal condition to unbalanced and distorted one.

As also seen in Fig. 3.9 and Fig. 3.10, the estimated grid voltages well assemble the actual grid voltages. However, there is a small difference in magnitude between the actual and the estimated voltage because of the imperfection of the experimental system. It should be also noted that such steady-state mismatch in estimated voltage does not affect the estimated grid angle and tracking performance of the proposed control scheme.

To investigate the quality of injected currents experimentally, Fig. 12 shows the experimental results of the proposed control scheme under unbalanced and distorted grid voltages. In spite of the abnormal grid voltages, the grid-side currents are considerably sinusoidal. In fact, according to the FFT result of *a*-phase current, the harmonic contents of injected currents well satisfy the limits specified by the grid interconnection regulation IEEE 1547 with the THD value of only 2.44%.

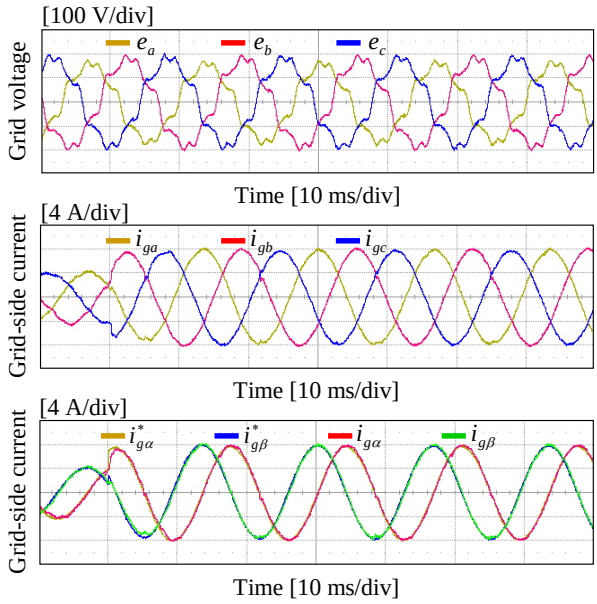

Fig. 3.11. Experimental results of the proposed control scheme when the reference current undergoes a step change.

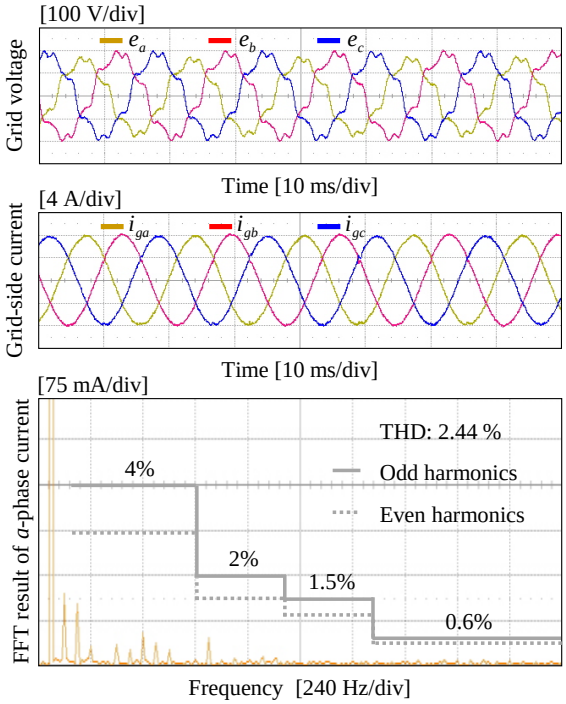

Fig. 3.12. Experimental results for steady-state response of the proposed control scheme under unbalanced and distorted grid voltage.

3.6 Conclusions

This chapter has presented a robust voltage sensorless controller (RVSC) for a three-phase power converter. The RVSC not only controls the converter system in a stable manner under uncertain grid impedance but also ensures harmonic-free injected currents by using only the grid-side current measurements. Structurally, the proposed scheme mainly consists of a state-feedback regulator and an extended-state estimator. Furthermore, the IMP and LMI approach have been employed to consider various types of grid disturbances. As opposed to the existing approach, the RVSC offers a complete framework for designing a controller which can cope with grid voltage distortion and impedance uncertainties at the same time. Comparative simulation and experimental results under different operating conditions have shown significant improvements in control performance by using the RVSC. More importantly, the RVSC can be used for the current control loop of a grid-forming converter to ensure the stability of the electromagnetic loop.

CHAPTER
4.

External Synchronous Controller

This chapter presents a new implementation approach that aims to facilitate the adaptation of the grid-forming concept in industry real-world applications. This new design concept allows the implementation of grid-forming functionalities in a power converter without requiring modification to its internal control firmware. Section 4.1 introduces the overall concept of external controller-based implementation. Section 4.2 presents the external synchronous controller for a single converter unit. In Section 4.3, the implementation of the external synchronous controller is extended for a renewable power plant. Finally, the summary of the chapter is given in Section 4.4. The work presented in this chapter is based on the publication "External Inertia Emulation Controller for Grid-Following Power Converter, *IEEE Transactions on Industry Applications*, 2021".

4.1 Concept

4.1.1 Philosophy

As discussed in Chapter 2, most of the existing grid-forming methods assume full liberty in modification of the internal control firmware of the power converter. However, it is not always straightforward to upgrade such firmware in practice because of the additional development effort and time are required. As a consequence, the actual deployment of the grid-forming converter is still limited to laboratory and small-scale demos even though this concept has been introduced more than two decades ago.

Taking advantage of communication channels available in the power converter, grid-forming functions can be implemented in external control hardware rather than the internal controller of the power converter. The external controller can compute the appropriate reference needed for providing grid-supporting functions to the power converter. This design concept eliminates the need of upgrading power converter firmware. Thus, this

approach can be applied to any grid-following power converter, eventually enabling the existing power converter to work as a grid-former.

The conceptual design of the external controller-based approach is illustrated in Fig. 4.1. Without loss of genericity, the power converter is assumed to (i) be able to operate under adverse grid conditions and (ii) to have a reasonable reference tracking performance. This requirement is to ensure that the power converter is able to follow the reference generated by the synchronous external controller without a significant delay. In this implementation, the grid-forming functions are implemented in the synchronous external controller. Such controller receives measurements from the power converter or measurement devices at the PCC through a communication channel. According to these measurements, the external synchronous controller computes appropriate references for the power converter. Both measurements and references can be transferred through a communication channel.

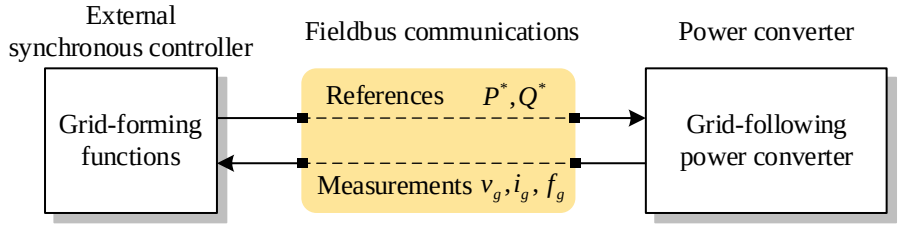

Fig. 4.1. Concept of external synchronous controller.

4.1.2 Design Considerations

Depending on the communication bandwidth, the grid-forming functions which can be implemented externally might include black start, inertia emulation, and power oscillation damping. In most cases, power converters are equipped with fieldbus communication interfaces such as CAN, Modbus, or EtherCAT [90]. Such communication is often used for exchanging operational data between power conversion systems and central control stations [91]. Among the most popular protocols used for grid-connected converters, the CAN bus suffers from a relatively high communication delay. This is because the maximum allowable baud rate is only 1 Mbps according to the protocol standard. However, the actual baud rate depends on cable length. In practice, baud rates from 125 kbps to 500 kbps are often used.

For high-power converters, Modbus are more common, especially, Modbus TCP/IP. As this protocol use Ethernet as a physical layer, the turnaround time of the protocol is much less than that of the CAN bus. The communication speed offered by Ethernet is usually 10 Mbps, 100 Mbps, or even 1000 Mbps. The main delay is caused by the transport layer due

to the connection-oriented nature of the TCP protocol. Indeed, the delay is the result of the overhead for establishing the connection between sending and receiving hosts. In practice, the turnaround time between a computer and a power converter via Modbus range from 20 to 50 ms depending on the networking capacity of the power converter.

Most recently, EtherCAT has been also used in power electronic systems. As this protocol is oriented for automation systems, it is optimized for determinism, speed, and robustness. In fact, the minimum achievable scan cycle is approximately 1 ms for 100 devices with a 100 bytes payload per device. A shorter scan cycle can be achieved with EtherCAT Automation Protocol (EAP). Our laboratory experiments reveal that turnaround of around 100 µs can be achieved with EAP in a peer-to-peer connection between a computer and a power converter.

For designing the external synchronous controller, it is vital to consider the delay introduced by communication delays. In fact, if EAP is available, a delay of around 100 µs allows the most demanding functions e.g. black start and resynchronization to be implemented in the external synchronous controller. However, with the delay of around 50 ms with Modbus TCP, only electromechanical functions are relevant for the external synchronous controller.

4.2 External Inertia Emulation Controller

To demonstrate the above concept, this section presents an implementation of the inertia emulation function using the external synchronous controller, hereafter referred to as eIEC. The main objective of the eIEC is to force the GFL converter to provide a synthetic inertia response for arresting frequency excursion during a frequency event. The eIEC will allow a GFL converter to operate as a GFM one to provide inertia support for improving the frequency stability of the power system.

4.2.1 Grid Model for Frequency Stability Analysis

Generally, an equivalent single-area system is often employed to assess the frequency stability of power systems [92], [93]. Due to the high share of renewables and recent instability incidents, the Nordic system is an exemplary model [94]. The system parameters are summarized in Table 4.1 [95]. It can be seen from Fig. 4.2 that the grid model is of 5^{th} order. As the PI controller, the low-pass filter, and the servo models can be further simplified by using the balanced truncation method as shown in Fig. 4.3. Such a simplification does not only facilitate the analysis of the controller performance but is also beneficial to real-time simulations during the validation.

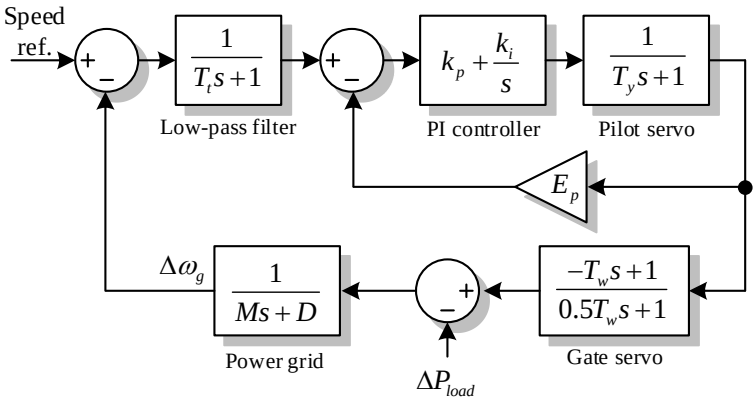

Fig. 4.2. Simplified model of the Nordic power system.

Table 4.1. Parameters of the Nordic system.

Definition	Symbol	Value
Filter time constant	T_t	0.5 s
Proportional gain	k_p	2 pu
Integral gain	k_i	0.49 s^{-1}
Droop coefficient	E_p	0.05 pu
Servo time constant	T_y	0.2 s
Water time constant	T_w	0.5 s
Inertia time constant	M	9.8 s
Frequency dependent load	D	0.9 pu
Coefficient	a_0	0.02265
Coefficient	b_0	0.4531
Coefficient	b_1	0.9937
Frequency deviation for load shielding		1.5 Hz
RoCoF for load shielding		0.18 Hz/s

From Fig. 4.3, the closed-loop transfer function of the reduced model is obtained as:

$$G_{grid}(s) = \frac{\Delta\omega_g(s)}{P_{load}(s)} = \frac{s + a_0}{2Ms^2 + (D + b_1 + Ma_0)s + b_0 + Da_0}. \quad (4.1)$$

To validate the accuracy of the reduced model, Fig. 4.4 shows the response of the grid

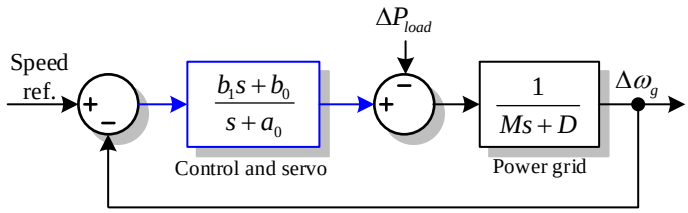

Fig. 4.3. Reduced model of Nordic power system.

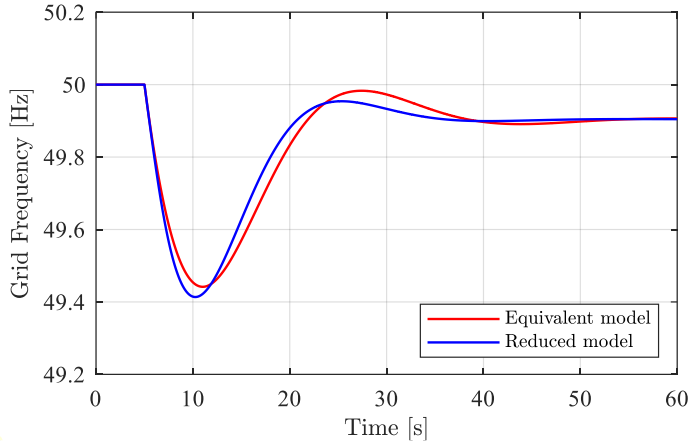

Fig. 4.4. Response of equivalent and reduced model for Nordic power system.

frequency during load of 0.02 pu is connected at 5 seconds. It can be seen that the dynamics of the two models are considerably similar. Indeed, the two response shares ROCOF value and frequency nadir differ slightly. Consequently, the reduced model is sufficient for accessing the performance of the external synchronous controller.

4.2.2 Model of a Grid-following Power Converter

Fig. 4.5 shows a conventional grid-following power converter, which is connected to the grid through an LCL filter. The electrical strength of the grid is modelled by the equivalent impedance characterized by the resistance of R_g and inductance L_g. The control system of the power converter consists of a power controller and a current controller. The main objective of these two controllers is to track the power references P^{ref} and Q^{ref} in a stable manner. For synchronization purposes, the grid phase angle is estimated by a phase-locked loop (PLL) that is constructed on the synchronous reference frame. The dynamic relation from the active power reference to injected power can be generally defined as $G_{PC}(s)$. Consequently, the complete model of the grid and the power converter is constructed as in Fig. 4.6.

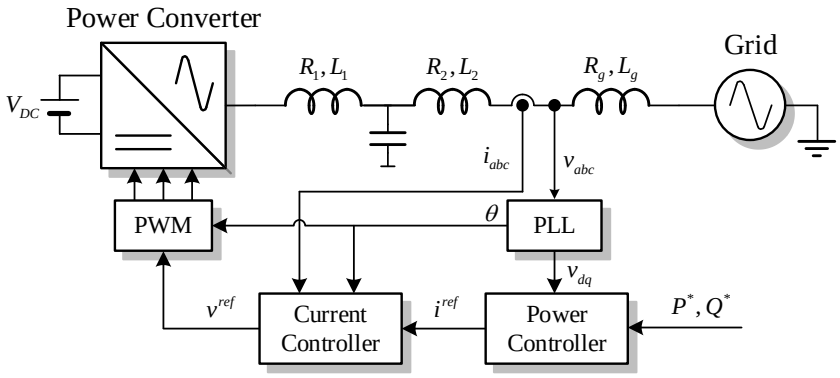

Fig. 4.5 Configuration and control of a typical grid-following power converter.

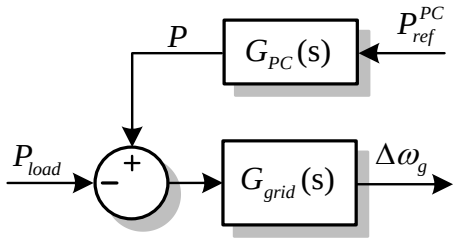

Fig. 4.6. Grid model with power converter integrated.

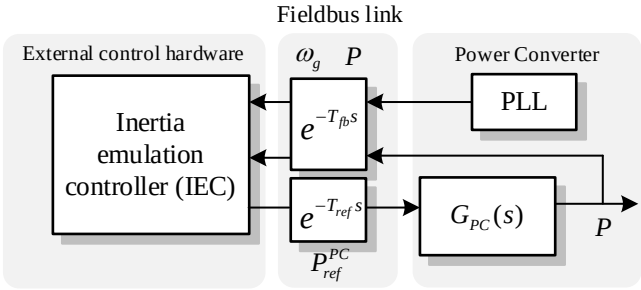

Fig. 4.7. Overall block diagram of the ESC implementation.

4.2.3 Control Structure

Fig. 4.7 shows the overall configuration of the external synchronous controller and the grid-following power converter. For a single converter unit, it is reasonable to assume that the ESC received the measurement at the PCC through the same communication channel used for sending the reference power. The measurements might include measured active power P and grid frequency ω_g. The grid frequency can be measured by the PLL of the power converter.

The control block diagram that is implemented in the external controller is shown in Fig. 4.8. Aiming to provide the inertia response to the grid-following power converter, the inertia emulation controller implements mainly the electromechanical equation. The inertia constant can be adjusted through the parameter H_v. The swing equation of the electromechanical part can be given as in (4.2).

$$G_1(s) = \frac{1}{2H_v s} \tag{4.2}$$

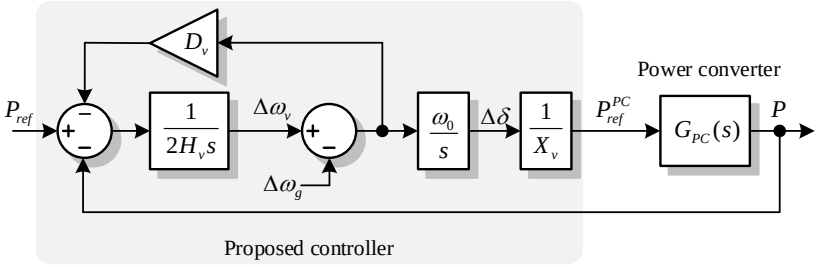

Fig. 4.8. Overall block diagram of the proposed control scheme.

The difference between deviations of virtual angle frequency $\Delta\omega_v$ and the measured grid frequency $\Delta\omega_g$ are used to calculate the angle deviation as:

$$\Delta\delta(s) = \frac{\omega_0}{s}\left(\Delta\omega_v(s) - \Delta\omega_g(s)\right), \tag{4.3}$$

where ω_0 denotes the nominal angular frequency.

As references for most GFL power converters are in a form of active and reactive powers, it is desirable to convert the angle deviation into active power. By using the well-known power flow equation, active power reference can be expressed as a function of angle deviation as:

$$P_{PC}^{ref} = \frac{V_{inv}}{R^2 + X^2}\left[R_V\left(V_{inv} - V_g\cos(\Delta\delta)\right) + X_{inv}V_g\sin(\Delta\delta)\right], \tag{4.4}$$

where V_{inv} and V_g denote the amplitudes of inverter output voltage and grid voltage, respectively, and R_v and L_v represent the virtual resistance and inductance, respectively. Assuming $R_v = 0$, $\sin(\Delta\delta) \approx \Delta\delta$, and $V_{inv} \approx V_g \approx 1$, the power flow equation can be rewritten as:

$$P_{ref}^2 = \frac{1}{X_v}\Delta\delta\,. \tag{4.5}$$

Combining (4.2), (4.5), and the transfer function of the grid-following power converter $G_{PC}(s)$ yields:

$$G_2(s) = \frac{P_{ref}^2(s)}{\Delta\delta(s)} = \frac{\omega_0}{X_v s} G_{pc}(s) . \tag{4.6}$$

To increase the damping ratio of the closed-loop system, the damping coefficient D_v is used as a feedback gain. The input signal for the damping block is taken after the summation block to avoid static gain that often introduces inherent droop characteristics in conventional SPC implementation. The damping of the closed-loop system can be adjusted through the damping coefficient. That is, the damping of the system is proportional to the value of D_v. Remark that, setting a high value for D_v might result in slower transience of the closed-loop system.

It is reasonable to consider that the settling time of the grid-following power converter range from 20 to 50 ms. Such dynamics are relatively fast compared to inertia response which lasts for a few seconds. Therefore, the transfer function of the grid-following power converter can be assumed to be unity, $G_{PC}(s) = 1$. As a consequence, the closed-loop transfer function can be obtained as:

$$\frac{P(s)}{P_{ref}(s)} = \frac{\omega_0}{2H_v X_v s^2 + D_v X_v s + \omega_0}, \tag{4.7}$$

$$\frac{P(s)}{\Delta\omega_g(s)} = \frac{D_v X_v s + \omega_0}{2H_v X_v s^2 + D_v X_v s + \omega_0} . \tag{4.8}$$

Note that (4.7) and (4.8) are in the form of second-order systems whose natural frequency is:

$$\omega_n = \sqrt{\frac{\omega_0}{2H_v X_v}} . \tag{4.9}$$

Generally, the virtual inertia constant H_v is often required by the system operator based on grid codes. For the ease of parameter tuning, the damping coefficient D_v can be expressed in terms of desired damping ratio ζ as in (4.10).

$$D_v = \zeta H_v \sqrt{\frac{8\omega_0}{H_v X_v}} \tag{4.10}$$

Employing (4.8), the frequency characteristics of the eIEC toward a grid frequency event can be illustrated as in Fig. 4.9, where the dashed lines indicate the lower and upper

cut-off frequencies which are approximately 1 and 3 Hz, respectively. Such frequency limits indicate that the eIEC has low susceptibility to high-frequency noises which are often of abundance in the frequency measurements due to the switching. This property suggests that eIEC is more stable in practical implementation than those based on frequency derivatives.

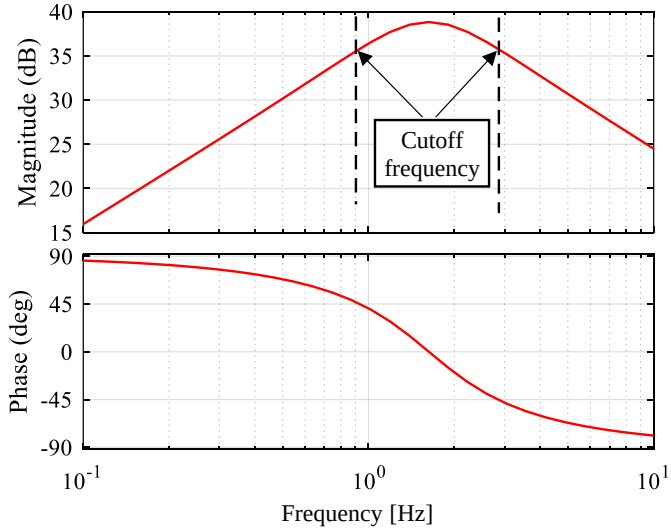

Fig. 4.9. Frequency response of the eIEC to grid frequency according to (8).

It is evident from Fig. 4.7 that the communications will introduce an unavoidable delay in the control loop. Such a delay can deteriorate the overall performance or even destabilize the system. Therefore, it is paramount to investigate the influence of the communication delays on the behavior of the eIEC as well as the stability of the grid.

The delay, which is caused by the forward path for sending reference P_{ref} and the feedback path for reading measurement signals ω_g and P, can be given as

$$T_d = T_{ref} + T_{fb} \tag{4.11}$$

where T_{ref} is the time required for power reference P_{ref} to reach the power converter. Similarly, T_{fb} is the time needed for the feedback signals ω_g and P to arrive at the eIEC. For the ease of latter analysis, the communication delay is approximated by using the first-order Padé approximant as:

$$G_d(s) = \frac{2 - 1.5T_d s}{2 + 1.5T_{ds}}. \tag{4.12}$$

Taking into account the communication delay, the control block diagram depicted in Fig. 4.8 might be extended as in Fig. 4.10 where a time delay transfer function is introduced between the virtual impedance block and the power converter block.

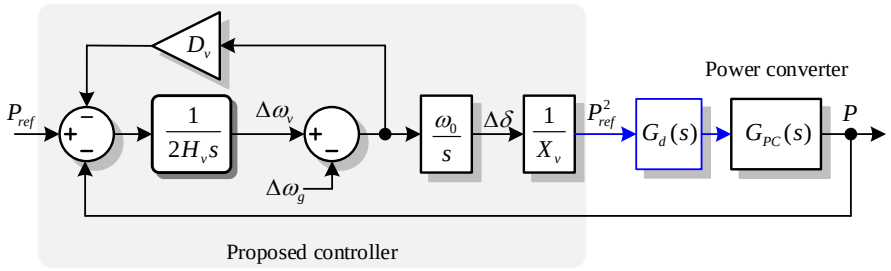

Fig. 4.10. Closed-loop system with communication delay.

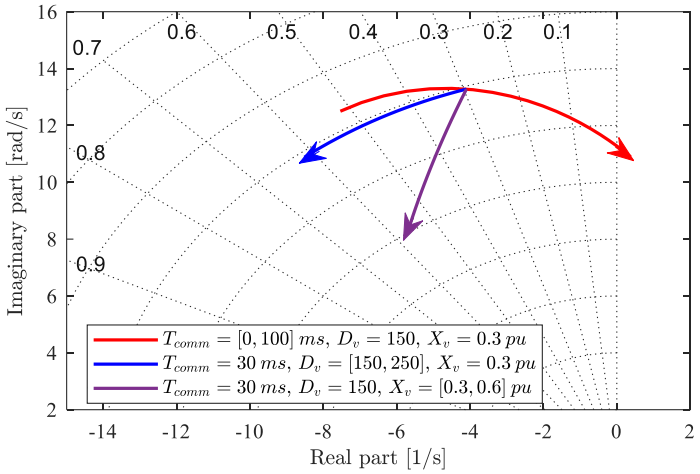

Fig. 4.11. Root locus of (14) with different values of T_{comm}, D_v, and X_v.

From Fig. 4.9, equation (4.6) is can be rewritten as:

$$G_{2d}(s) = G_2(s)G_d(s)\,. \tag{4.13}$$

From Fig. 4.6, (4.1), (4.2), and (4.13), the transfer function that combines the power converter, the eIEC, and the grid can be obtained as follows:

$$\frac{P(s)}{\omega_g(s)} = \frac{(D_v G_{grid} + G_{2d} G_{grid})G_1 + G_{grid}}{(D_v + G_{2d})G_1 + G_{2d} G_{grid} + 1}\,. \tag{4.14}$$

where the Laplace operator s has been omitted in (4.14) for simplicity. Remark that (4.14) is a fifth-order system. For such a high order system, root locus and frequency response techniques can be used to investigate its dynamic behaviour.

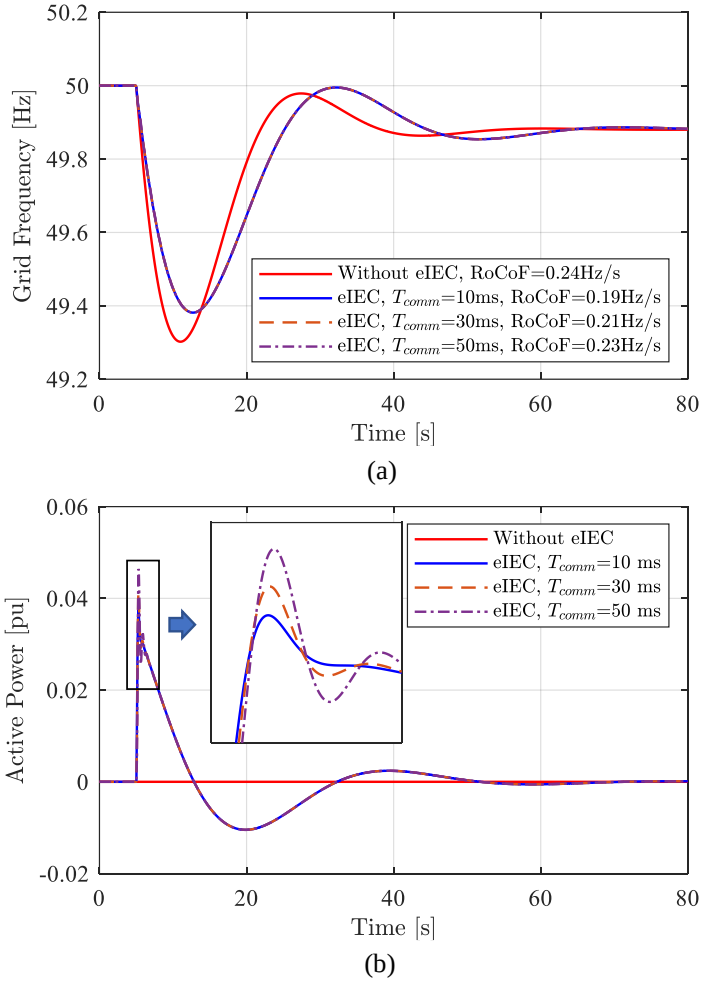

Fig. 4.12. System response to a load connection of 0.05 pu at 5 s for different values of T_{comm} : (a) Grid frequency, (b) Active power injected by grid-following power converter.

For illustration, assuming that the virtual inertia, virtual impedance, and damping ratio are chosen as: $H_v = 5\,s$, $X_v = 0.3\,pu$, and $\zeta = 0.707$, respectively. The damping coefficient can be obtained from (4.10) as: $D_v = 145$. From (4.14), a root locus for various values of T_{comm}, D_v, and X_v can be obtained as in Fig. 4.11. The arrows show the changes of the system poles when communication delay, damping coefficient, or virtual impedance increases. It is clearly shown that the increment of communication delay forces the

oscillatory pole to move closer to the imaginary axis. Such a movement of the pole indicates the decrement in damping ratio and stability margin. In fact, the closed-loop system becomes unstable when the communication delay T_{comm} reaches 100 ms.

Since all the parameters of the eIEC are virtual, they can be adjusted to increase the stability margin of the system. In general, the virtual inertia constant H_v is set by the operator, leaving the virtual impedance X_v and the damping coefficient D_v as potential tuning parameters. It is evident from Fig. 4.10 that the X_v is inversely proportional to the power reference produced by eIEC. Therefore, by decreasing X_v, it is possible to reduce the net gain of eIEC. In a similar manner, D_v can also be increased to compensate for the time delay.

In addition to stability, the performance of the eIEC is also of importance. Fig. 4.12 shows the response of the grid frequency and active power reference under a load step event by using (4.14). Fig. 4.12a confirmed that the eIEC help to reduce the RoCoF and frequency nadir values. That is, the highest frequency deviation is decreased to 0.1 Hz, while the RoCoF value is decreased by 32%. Also, Fig. 4.12b illustrates the active power injected by the power converter. As soon as the communication delay reach 50 ms, the active power injected by the grid-forming power converter becomes noticeably oscillatory. Such oscillatory behaviour is due to the movement of the closed-loop pole toward the right-hand side of the *s*-plane.

Fig. 4.13 shows the system frequency and the active power injected by the converter for a load connection event. As illustrated, the inertia response is directly proportional to the inertia constant H_v. Remark that the system dynamics is also slightly influenced by the inertia value. That is, increasing the virtual inertia make the response more oscillatory, indicating a lower stability margin. Generally, the inertia constant of the generators within an electrical area are usually dictated by system operators to avoid undesired interactions such as electromechanical oscillations. Thus, it is convenient to calculate D_v according to desired inertia constant H_v.

Even though disturbances of around 5% are often considered for small-signal analyses [93], [96], more severe events might occur in power systems in real operations. To analyse the performance of the eIEC in the events where RoCoF values are particularly high, simulations with a load event of 0.2 pu is performed. For such a significant event, the grid suffers from a RoCoF value of approximately 0.98 Hz/s as shown in Fig. 4.14. Despite the severity of the perturbation, the eIEC still perform properly to improve the frequency behaviour of the grid. Indeed, for all the values of communication delays, the eIEC helps to reduce the RoCoF values up to 0.66 Hz which is only 67% of the RoCoF value in the base

case. This improvement is proportional to the results shown in Fig. 4.12. Concretely, the eIEC is effective in improving the frequency stability of the grid even in extreme events.

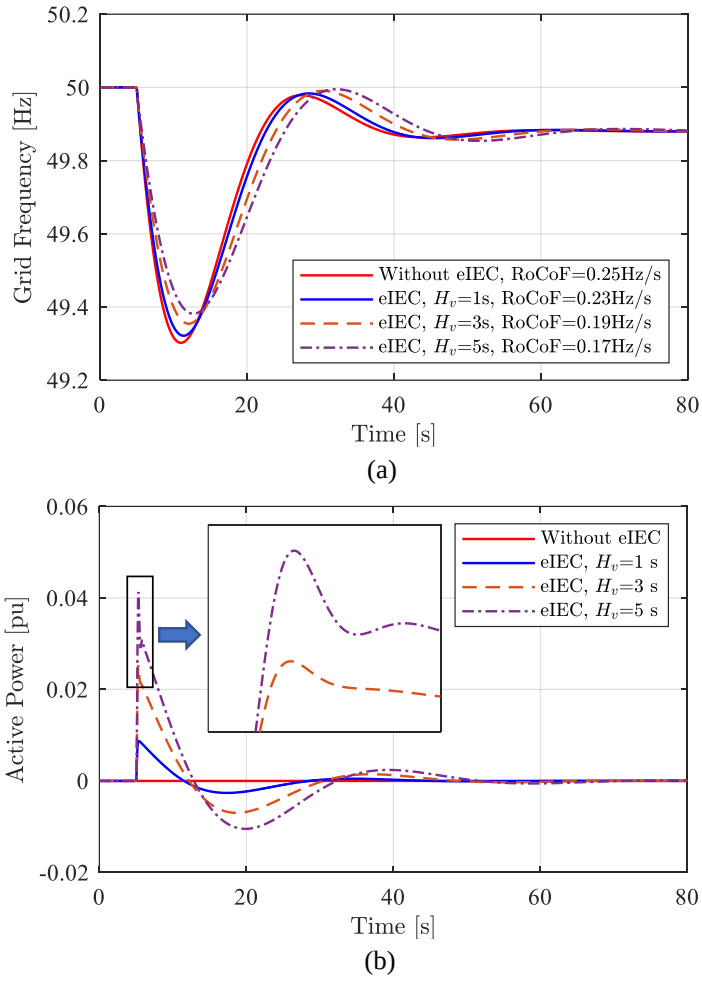

Fig. 4.13. System response to a load connection of 0.05 pu at 5 s for different values of H_v: (a) Grid frequency, (b) Active power injected by the grid-following power converter.

4.2.4 Hardware-in-the-Loop Validation

To investigate the performance of the proposed eIEC in experimental settings, HIL simulations have been carried out. The setup for such simulations is conceptually described in Fig. 4.15(a) and the hardware implementation is illustrated in Fig. 4.15(b). In this setup, the grid model in Fig. 4.3 and the converter circuit in Fig. 4.5 are simulated by a real-time simulator (Typhoon HIL 602+). The inner controllers of the converter including power controller, current controller, and PLL are implemented by a digital controller based on

TSM320F28335. The parameters of the grid-following power converter are summarized in Table 4.2.

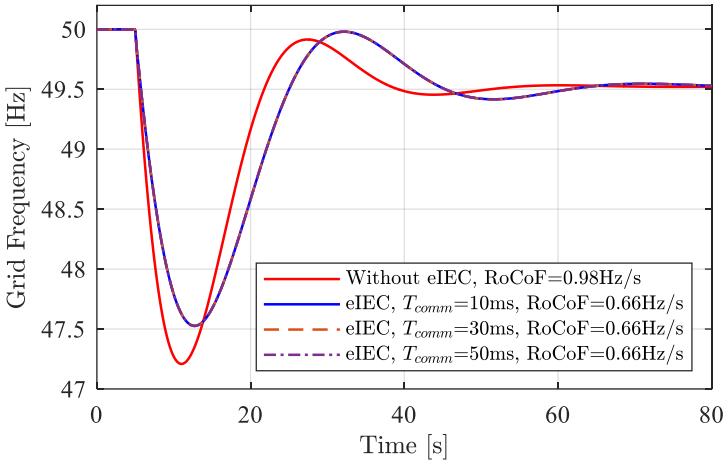

Fig. 4.14. Grid frequency following a load connection of 0.2 pu for different values of communication delay.

The proposed eIEC is tuned under the assumption that the grid-following converter fully complies with respective grid interconnection codes and is supplied by a sufficient source on the DC side. The eIEC is implemented in a programable logic controller manufactured by Beckhoff (CX9020). The communication link between the programable logic controller and the power converter controller is based on EtherCAT Automation Protocol (EAP) which allows high communication speed e.g. up to 1 ms turnaround time. Employing such a high-speed communication link allows for emulating various settings for communication delay. For instance, Fig. 4.16 shows experimental measurements of communication delays for an EtherCAT Automation Protocol (EAP) link with different settings of PLC scan cycles. For the HIL experiments, turnaround times of 10, 30, 50, and 90 ms are considered to emulate the delay caused by the common fieldbus protocols.

With regard to the grid-synchronization of the power converter, a conventional synchronous reference frame phase-locked loop (SRF-PLL) is employed [97]. For all the simulations, the bandwidth of the SRF-PLL is set to 50 Hz which results in a settling time of approximately 20 ms. To emulate a perturbation, a load of 0.05 pu is connected at the PCC at the 5th-second. Remark that the 0th-second in the time axis of the following HIL results denotes the starting time of data acquisition instead of the starting instance of experiments.

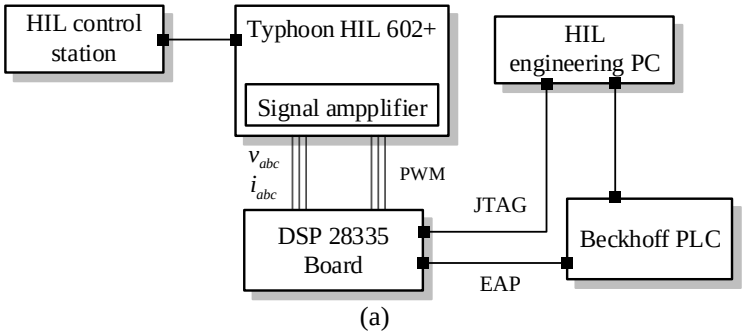

(a)

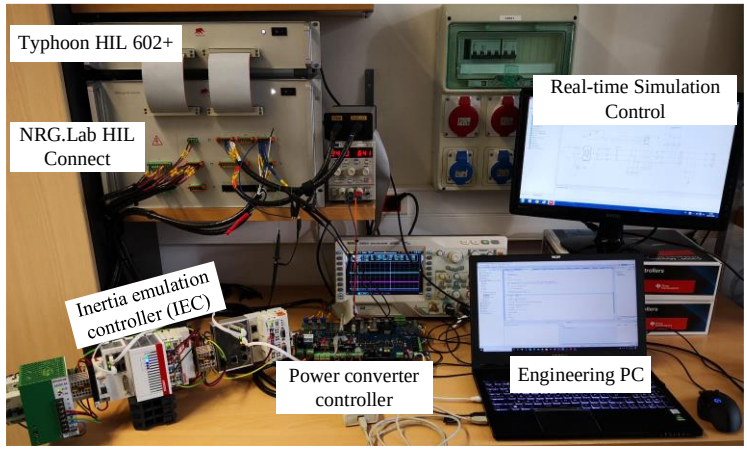

(b)

Fig. 4.15. Hardware-in-the-loop experimental testbed: (a) configuration. (b) hardware setup.

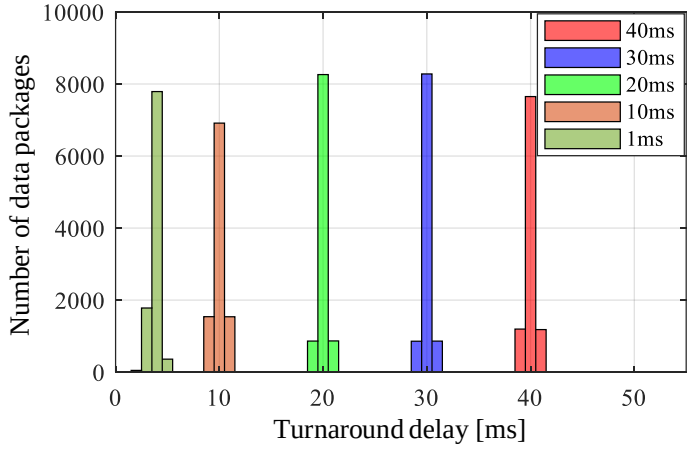

Fig. 4.16. Communication turnaround time for different settings of EAP.

Table 4.2. Parameters of the Nordic system.

Definition	Symbol	Value
Nominal power	P_n	100 kW
Nominal voltage	V_n	400V
Grid frequency	f_g	50 Hz
Switching frequency	f_{sw}	3150 Hz
Sampling frequency	f_s	6300 Hz
DC bus voltage	V_{DC}	750 V
Inverter-side inductance	L_1	778 µH
Inverter-side resistance	R_1	7.3 mΩ
Grid-side inductance	L_2	402 µH

Fig. 4.17 shows the HIL results of the eIEC for different communication configurations. It is clearly shown the injected power is superimposed with high-frequency harmonics due to switching. Such harmonic distortions are common in power converters. Yet, the influence of harmonics on the system performance is minimal. That is, the HIL results are very similar to simulation results based on transfer functions in Fig. 4.12. Similarly, Fig. 4.18 shows the HIL results of the eIEC for different values of virtual inertia. This result practically confirms that the active power provided by the eIEC to support the grid frequency can be determined by the H_v. As shown, for $H_v = 1\,s$, $H_v = 3\,s$, and $H_v = 5\,s$, the maximum amplitude of the active power are 0.01, 0.02, and 0.03 pu, respectively.

As discussed in the preceding section, the communication delay is one of the main factors determining the stability and performance of the closed-loop system, especially when the delay value is higher than 20 ms. As shown in Fig. 4.19, the oscillatory terms in the injected active power are unnoticeable when the communication turnaround time is 10 ms. However, as soon as the time delay increases to 90 ms, the oscillatory poles move toward the imaginary axis, as shown in Fig. 4.11 giving rise to a poorly damped behaviour of the injected active power. Remark that the oscillation frequency observed in Fig. 4.18 is the same as that of the pole depicted in Fig. 4.11. As a result, the HIL results validate the practicality of the eIEC. Moreover, these results also confirm the theoretical analyses performed during the parameter design phase.

4.2.5 Experimental validation

One of the key advantages of the eIEC is to be readily applicable to commercial converters without any modification on the control firmware of the converter. To

demonstrate the key merits of the eIEC, experiments have been carried out. The objectives of the experiments are to verify that

i) the ESC can provide an inertia response,

ii) the ESC can be readily applicable to commercial GFL converters,

iii) the ESC enables remote controlling, parameterizing, and troubleshooting high-level control applications for power converters.

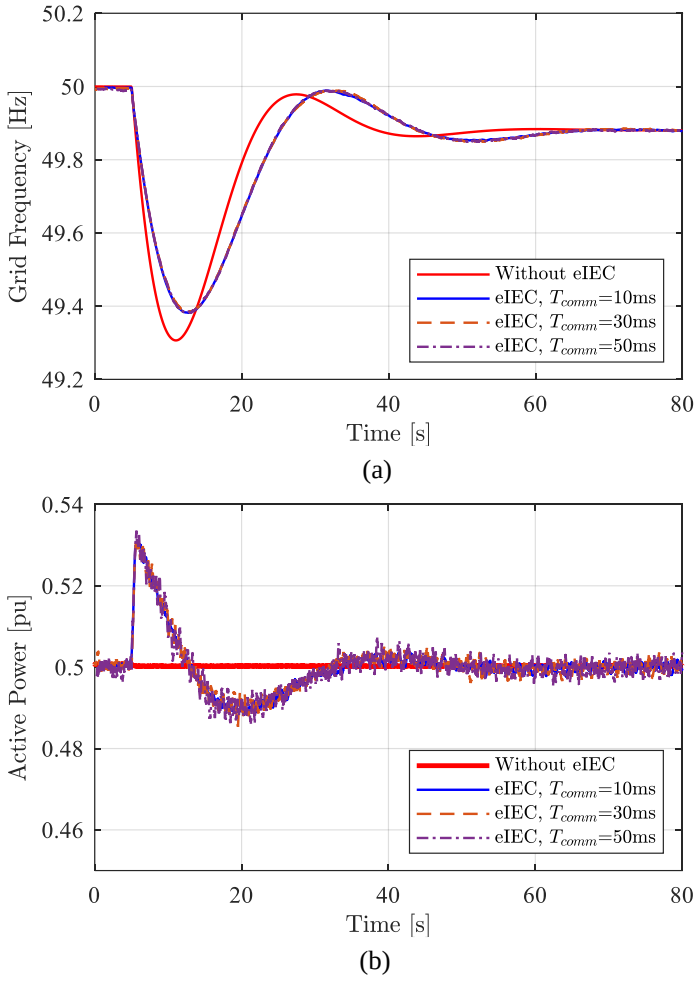

Fig. 4.17. HIL results for different values of communication delay. (a) Grid frequency, (b) Active power injected by the grid-following power converter.

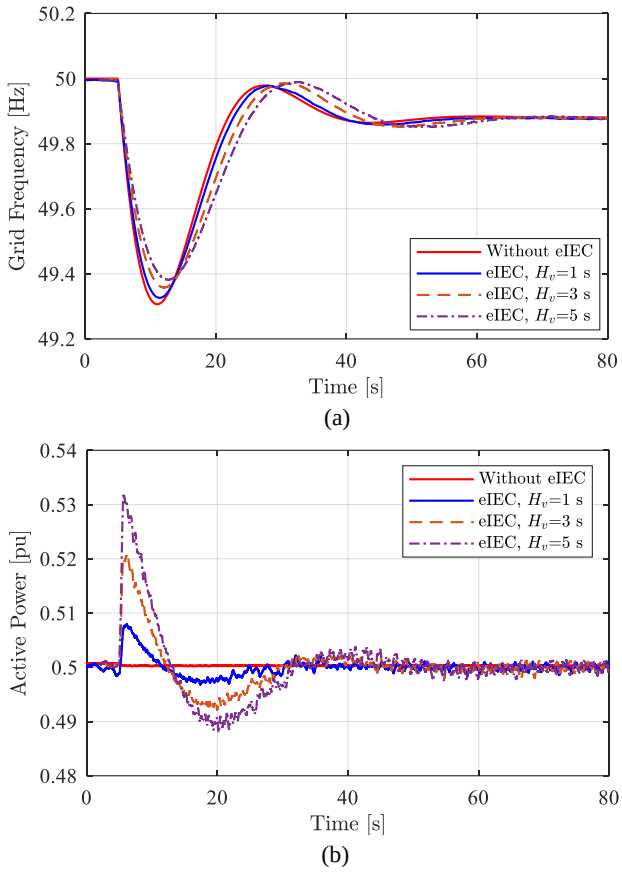

Fig. 4.18. HIL results for different values of virtual inertia. (a) Grid frequency, (b) Active power injected by the grid-following power converter.

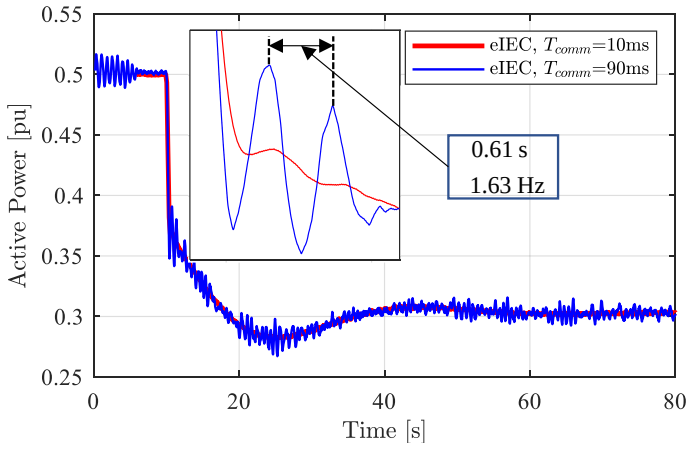

Fig. 4.19. HIL results for maximum allowable communication delay.

The control structure used for experiments is shown in Fig. 4.20. For generalization purposes, a conventional GFL converter is considered. The GFL converter is controlled by a cascaded control scheme which is made of a power controller and a current controller. For designing the eIEC, the exact structure of the control system of the GFL converter is not required. However, it is reasonable to assume the power controller of the GFL converter has a settling time of at most 20 ms so that dynamics of the GFLC can be omitted.

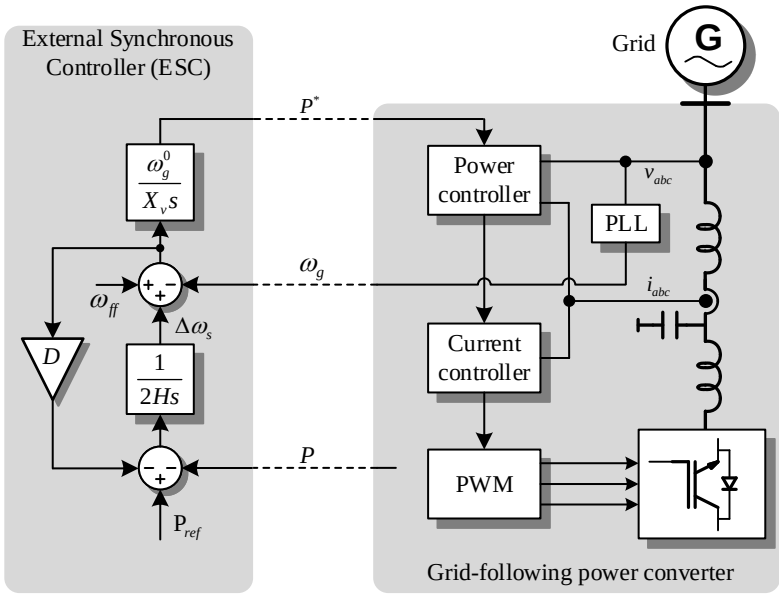

Fig. 4.20. Interconnection between external controller and the GFL converter.

To achieve the aforementioned objectives the experimental system is set up as in Fig. 4.21. The experimental setup consists of two stations. The remote station located in Luxembourg hosts the remote engineering PC for controlling and data acquisition from the local testing site which is located in Spain. The two engineering PCs are connected through a virtual private network (VPN) for a remote desktop connection. The ESC is implemented in a Beckhoff programable logic controller (PLC) model CX1020 with a 1 GHz processor. The PLC is connected with the local engineering PC through the automation device specification (ADS) protocol for operational control, programming, and data acquisition. For control purposes, the PLC communicates with the GFLC through Modbus TCP/IP protocol. The GFLC, which is controlled by a TMS320F28335 microcontroller, has a rated power of 500 kW and is manufactured by JEMA energy. The nominal line voltage and frequency for the GFLC are 400 V and 50 Hz, respectively.

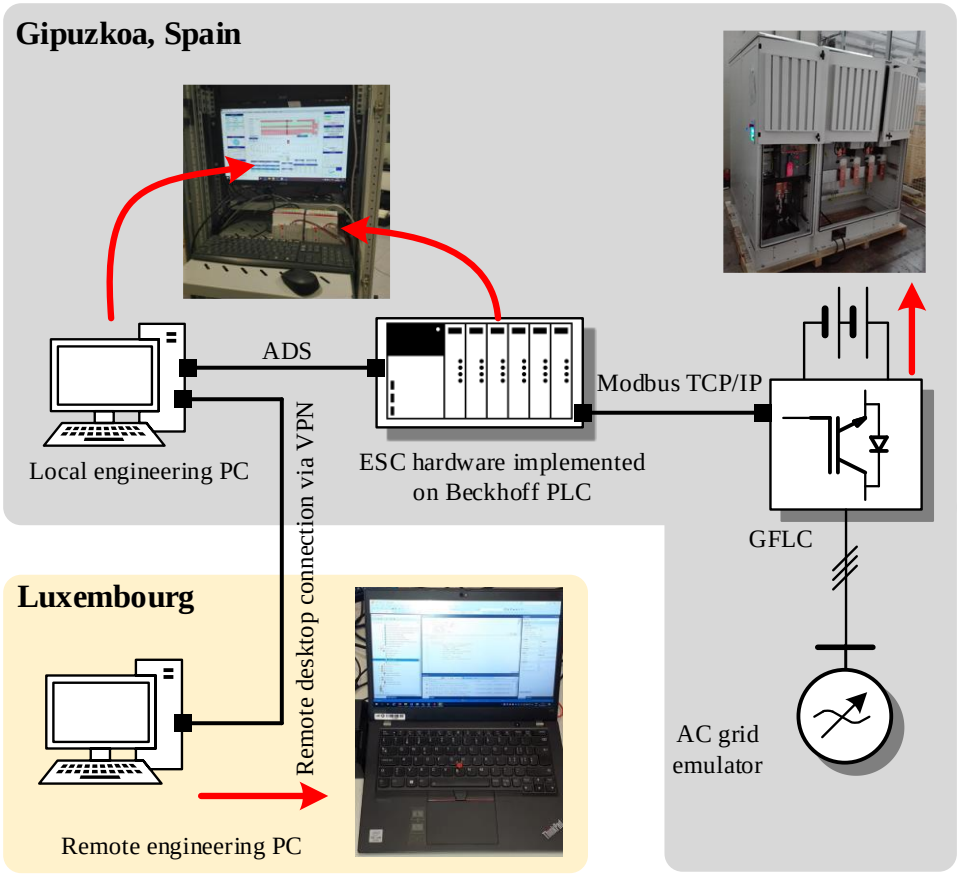

Fig. 4.21. Experimental setup.

Fig. 4.22 shows the transient dynamics of the GFLC. This result reveals the dynamics of the internal controller of the GFLC. It can be seen that the injected currents reach a steady state in around 20 ms. This is consistent with the assumption made in section III to simply the parameter tuning and analysis of the ESC. Indeed, the setting time of the GFLC is well shorter than the delay caused by the communication between ESC and GFLC. Therefore, it is reasonable to omit the dynamics of the GFLC when analysing the electromechanical behaviour of the ESC-GFLC.

From experimental data, the turnaround delay between ESC and the GFLC is less than 20 ms for Modbus TCP/IP connection. Therefore, a sampling period of 20 ms is configured in the experiments for reflecting the normal operating conditions of the system. Fig. 4.23a shows the inertia response of the ESC-GFLC when $T_d = 20$ ms and a negative step change of 1Hz in grid frequency is introduced at around 36 seconds. As clearly shown, the ESC-

GFLC injects active power of around 100 kW or 0.2 pu to support the grid frequency regulation. This inertia response well matches the simulation results shown in the previous section.

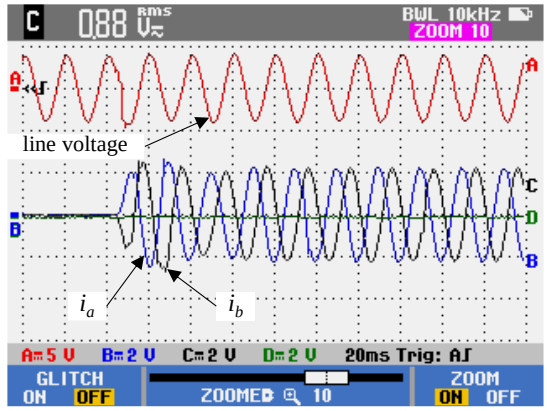

Fig. 4.22. Transient response of the GFL converter under a step change in active power reference.

Even though the turnaround time is 20 ms for this system, the delay could go up to 80 ms in rare cases due to packet dropout or network congestions. Thus, it is important to make sure that the system does not become unstable in such unusual instances. Fig. 4.22b shows the inertia response of the ESC-GFLC when $T_d = 100$ ms and a step-change of -1Hz in grid frequency is introduced at just before 442 seconds. The results confirm that the closed-loop system remains stable regardless of the high value for delay. However, due to the low damping, the system suffers from oscillations, which is well consistent with the analysis and simulation in the previous sections.

The results presented in Fig. 4.23 confirmed that the ESC-GFLC is able to provide inertia response in a stable manner for a predefined range of communication delays, which fulfils the objective (i). Note that the GFLC is loaded with the original control firmware provided by the manufacturer for all the experiments, thus fulfilling the objective (ii). Finally, the experiments have been completely conducted from the remote engineering PC at the remote testing site. This explains the staircase waveforms in Fig. 4.23. The staircase waveform of injected active power is because of the low data acquisition rate at the engineering PC. The fact that the ESC enables experimentation on a utility-scale power converter through a distance of thousands of kilometres suggests the ESC might act as an information gateway for system operators to gain control of high-level functions grid-connected power converters. This feature is not only limited to synthetic inertia but can

easily be extended for other grid-supporting functionality such as power oscillation damping and voltage control.

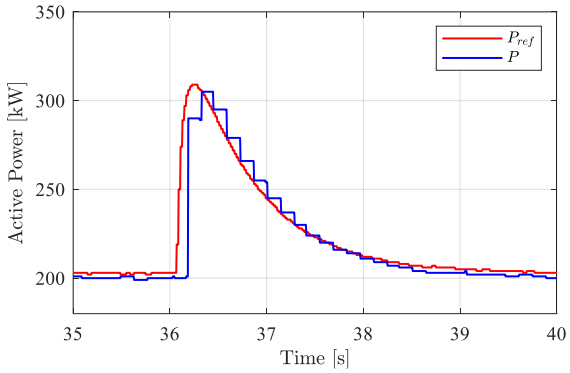

(a)

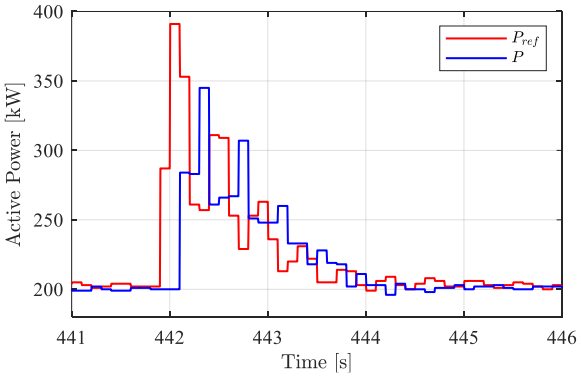

(b)

Fig. 4.23. Inertia response of the eIEC when (a) $T_d = 20\,ms$ and (b) $T_d = 100$ ms.

4.3 External Synchronous Controller for a Power Plant

The application of an external synchronous controller is not limited to a single power converter but can be easily extended to renewable power plants. In fact, most renewable power plants are controlled by a central controller which communicates all the power converters within the plant via a Fieldbus communication. As a result, GFM functions can be implemented in the central control of the renewable power plant. This section briefly describes the implementation of ESC for a PV power plant.

4.3.1 Control Structure

Provided that renewable power plants often consist of a large number of power converters, the measurements at the PCC for the central controller is usually provided by an independent measurement unit connected to the PCC. Fig. 4.24 shows the control structure for a GFM controller using external control hardware. The presented control consists of four parts: the power loop controller (PLC), the reactive power controller, the angle deviation calculator, and the power reference generator. Similar to the SPC, the PLC implement a swing equation to provide inertia and necessary damping. The reactive power employs a PI controller for regulation purposes. The synchronous frequency provided by the PLC is integrated to obtain the synchronous angle which is then later used together with measured grid voltage for calculating the load angle through Park's transformation. From the load angle δ and reference voltage e, the power to be delivered by the power converter are calculated as:

$$P^* = \frac{V_{PCC}}{R_v^2 + X_v^2}\left[R_v \left(V_{PCC} - E_v \cos\delta_v \right) + X_v E_v \sin\delta_v \right], \tag{4.15}$$

$$P^* = \frac{V_{PCC}}{R_v^2 + X_v^2}\left[R_v \left(V_{PCC} - E_v \cos\delta_v \right) + X_v E_v \sin\delta_v \right]. \tag{4.16}$$

The reference power P^* and Q^* can be used to generate the references for each power converter through the proportional gain k_i k obtained from (4.17).

$$k_{pi} = k_{qi} = \frac{S_i}{\sum_1^N S_i} \tag{4.17}$$

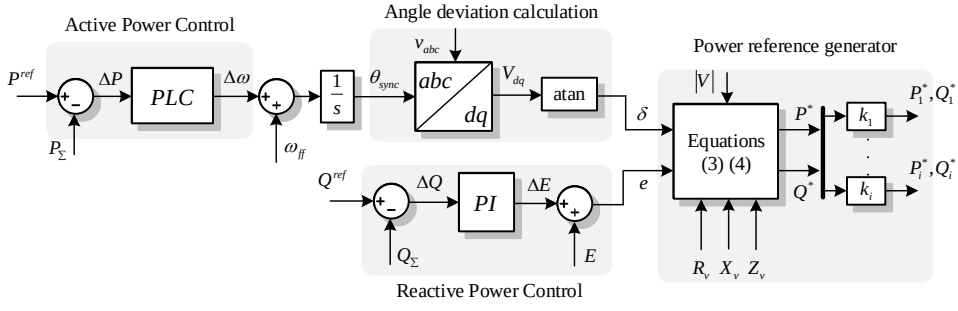

Fig. 4.24. ESC implementation for a renewable power plant.

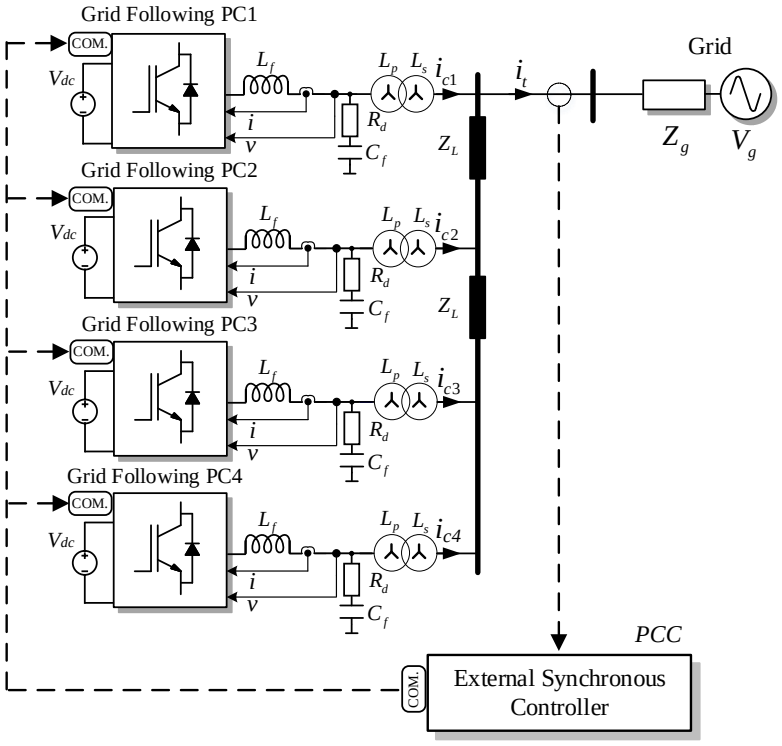

Fig. 4.25. Overview of experimental setup for validating ESC implementation.

4.3.2 Validation

To validate the ESC implementation for a PV power plant, a scaled-down system depicted in Fig. 4.25 is used. The targeted system consists of four GFL power (Danfoss: FC-302P2K2T5E20H1) which are controlled by digital controllers based on a microcontroller TMS320C28335. The dc-link voltage is supplied by a 20 kW dc voltage source (MagnaPower: TSD1000-20). A 30 kVA transformer is used for interfacing the converters with the grid. The experimental setup is shown in Fig. 4.26. The ESC algorithm is implemented in a control board based on a TMS320C28335 DSP which communicates with each power converter via CAN communication at a bandwidth of 125 kps

Fig. 4.27 shows the comparison results for the SPC-GFM controller for each power converter and the ESC under a load step. It can be seen that, in both cases, the power converters inject active power to support the grid under such perturbation. These responses demonstrate that both control schemes provide inertia responses to the grid. Nevertheless, as explained earlier, the dynamic responses of the SPC-GFM controller are not satisfactory due to the unequal power-sharing characteristic during transients. Such a mismatch in active power is caused by the difference in grid impedance between each converter and the PCC.

The transient power mismatch might create power oscillations at PCC thus worsening the power quality. On the contrary, the ESC allows the power converter to provide equal power participation of all GFL converters during transience. Such improvement is achieved because the electromagnetic layer is common for all power converters meaning that the connection impedance is virtually the same for all generation units. It is evident that the ESC offers better dynamic performance compared to conventional GFM implementation. Moreover, modification to the internal control firmware of each power converter is also avoided.

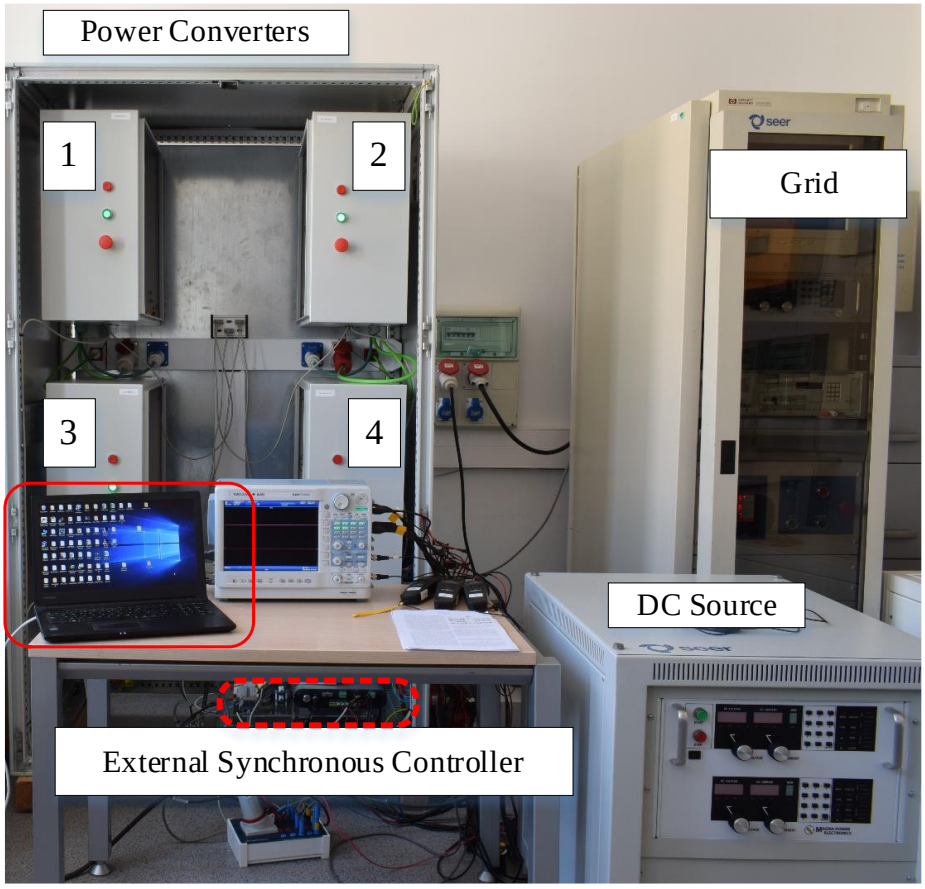

Fig. 4.26. Experimental setup for the system in Fig. 4.25.

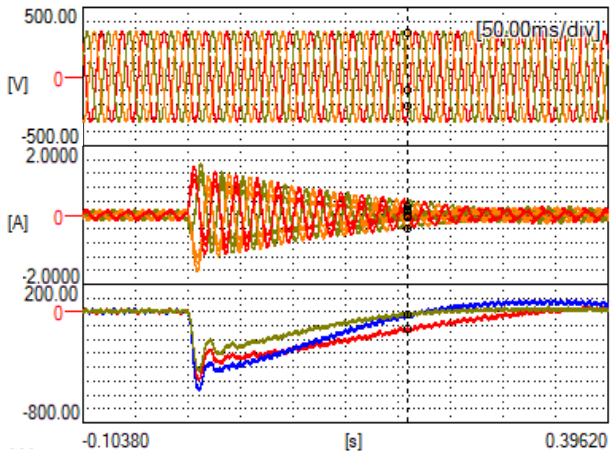

(a)

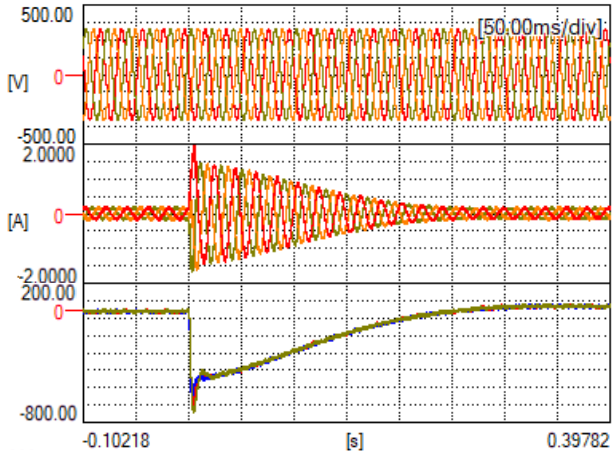

(b)

Fig. 4.27. Experimental results of ESC for a PV power plant under a load step for (a) SPC-GFM controller implemented for each power converter and (b) the ESC controller.

Fig. 4.28 shows the damping performance of the ESC-based PV power plant. The system under test consists of a PV power plant connected to a strong grid. A synchronous generator is connected at the PCC to emulate power oscillations. The configuration of the test system is illustrated in Fig. 4.28a. As shown in Fig. 4.28b where the ESC is tuned with a low damping profile, the system suffers from noticeable oscillations which are typically due to the low damping nature of the SG connected at the PCC. As soon as, the damping of the ESC is increased, the dynamic response of the active power injected by the PV power plant is considerably improved. That is, the oscillatory terms in the injected active power

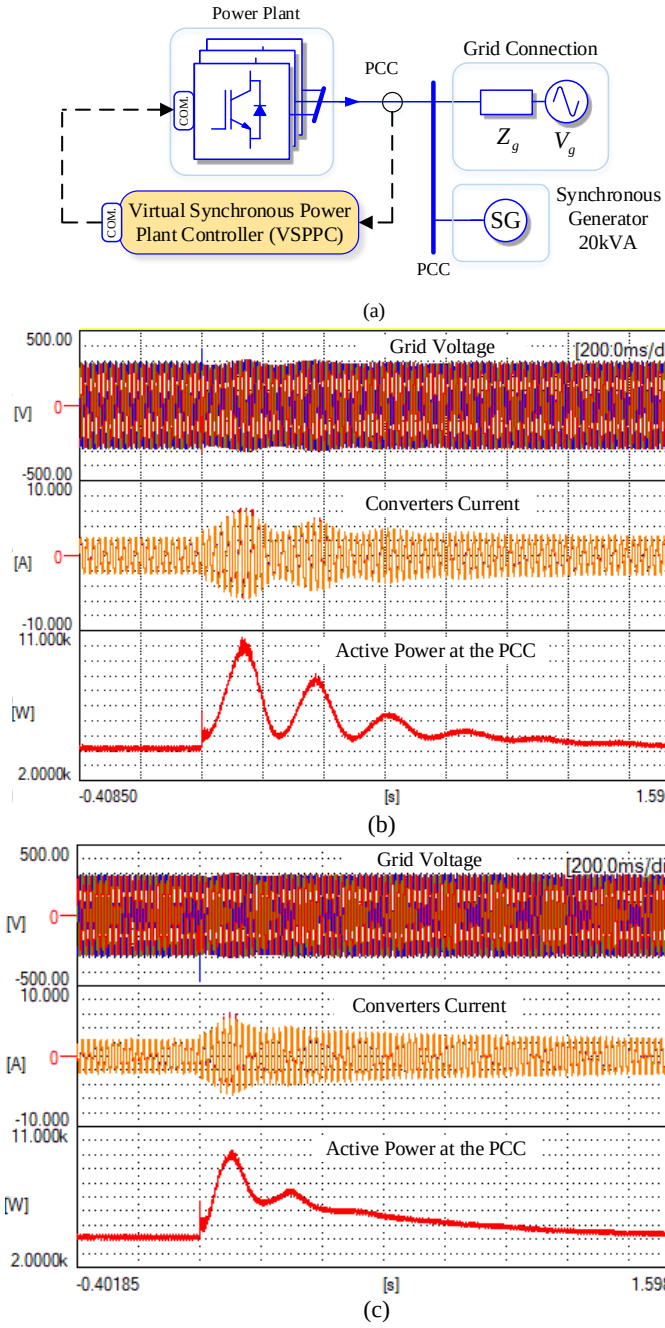

Fig. 4.28. Damping performance of the ESC. (a) Test system, (b) ESC with $G_c = 4.796e^{-4}$ and $\omega_c = 8.186$, (c) ESC with $G_c = 2.741e^{-4}$ and $\omega_c = 14.326$.

are nearly eliminated. This result confirms that the ESC implementation is able to enhance the small-signal stability of power systems without the need to modify the firmware of the individual power converter.

4.4 Conclusions

This chapter presents a new implementation method, namely external synchronous controller, for transforming a GFL converter into a GFM converter. That is, GFM functions can be implemented in external controller hardware which interacts with the GLC converter through a communication link. Depending on the communication bandwidth, different GFM functions can be implemented. For instance, electromechanical dynamics can be possible for most Fieldbus communication as demonstrated in section 4.2. However, for a faster link, part of electromagnetic functions can be also considered as in Section 4.3. For demonstrating the practicality of this new implementation, validation for the system with only one power converter and a system with multiple converters have been tested experimentally. The results clearly confirm that the ESC, if properly designed, might provide a similar dynamic response compared to conventional GFM schemes. The advantages of the ESC are more vividly in the case of renewable power plants where the ESC can provide better performance with minimal modification on the existing system infrastructure.

CHAPTER
5.

Power Oscillation Damper for Grid-forming Converters

Grid-forming power converters have been increasingly used in power systems as an ultimate solution to address the challenges imposed by the ever-increasing renewable integration. In spite of its versatility, GFMC has only been utilized to provide islanded operation, grid regulations, and synthetic inertia. To broaden the application of GFMC in improving the stability of power systems, this chapter presents a multi-rotor virtual machine (MRVM) controller to deal with electromechanical oscillations. Motivated by the well-known virtual synchronous machine (VSM) concept, the MRVM aims to design a VSM-based GFMC with multiple virtual rotors whose electromechanical behaviour are separately tenable to damp specific oscillatory modes in power system. The remainder of this chapter is organized as follows. Section 5.1 review the existing approaches to deal with power oscillations using power converters. Section 5.2 analyses the impact of a grid-forming power converter in damping sub-synchronous oscillations, aiming to highlight the limitation of GFM when dealing with oscillations of higher frequencies. Section 5.3 presents the concept and design of the MRVM. The tuning principle for the MRVM is given to facilitate the selection of the control parameters by using frequency-domain techniques and the eigenvalue locus analyses. Section 5.4 summarizes the key points of the chapter. The work presented in this chapter is based on the publication "Multi-Rotor Virtual Machine for Grid-Forming Converter to Damp Sub-Synchronous Resonances, *IEEE Access*, 2021".

5.1 Introduction

Sub-synchronous resonances (SSR) exist inherently in power systems due to the power exchange between generators when interconnected through long transmission lines [98], [99]. This phenomenon was observed and investigated since the very early development

stages of power networks. However, the advent of renewable energies has attracted a renewed interest in power oscillations within the frequency range of 0.1 to 2.0 Hz [100]. Indeed, the increasing deployment of converter-based generations is not only reducing the damping of the existing oscillatory modes but also introducing new ones [2]. Such an influence of renewable generation degrades the performance of the power system because operators must enforce more conservative limits on the admissible power transfer on transmission lines to retain the system stability. These restrictions, however, increase considerably operational costs leading to social welfare reduction [101]. Therefore, damping of subsynchronous resonances is essential in terms of stability and efficiency.

Power System Stabilizer (PSS) has been one of the most efficient approaches for increasing damping to low-frequency modes. Usually, PSSs are implemented as an additional feature of the excitation system of the generator [102]. There are different types of PSS and also various tuning procedures [103]. In most cases, the PSS parameters are set upon plant commissioning and rarely updated [104]. To achieve optimal results, the placement of the PSS as well as its tuning are of importance. With converter-based generation units displacing many of the existing conventional power plants [105]: (i) suitable PSS deployment sites will become rarer and (ii) the number of already deployed PSS will decrease and so will the damping of critical modes.

Similar to PSS for conventional generators, power oscillation dampers have been also presented for flexible alternating current transmission systems (FACTS). For example, the sliding mode controller has been proposed in a static synchronous compensator (STATCOM) [106]. Likewise, the robust linear quadratic regulator is used in a thyristor-controlled series compensator (TCSC) to damp electromechanical modes [107]. Various damping approaches for FACTS devices are summarized in [108] and [109]. Due to the increasing installation of renewables and energy storage systems (ESS), the use of power converters for dealing with electromechanical interactions in electrical networks has become even more feasible and practical. Noticeably, optimal tuning techniques and proportional-integral-derivative controller have been employed in ESS [110] and photovoltaic systems [111] to damp low-frequency oscillations.

However, the aforementioned techniques only aim to maximize the SSR damping of the power converter, which is not always desirable. In fact, in addition to damping oscillations, power converters often need to provide the functionalities and services to withstand and support the grid during adverse operations, for instance during voltage sags and low-inertia periods [112], [113]. As a result, it is often difficult to implement separately the individual controller for each of the functionalities such that the closed-loop system can operate stably and reliably.

To address such a limitation, the grid-forming converter (GFMC) concept has been introduced in the late 2000s. GFMC refers to a group of control techniques which control grid-connected converters as a voltage source [114], [115]". As per ENTSO-E, a GFMC should be able to support the operation of the ac power system under normal, alerted, emergency, blackout and restoration states without having to rely on services from synchronous generators [16]. Indeed, the GFMC, especially those based on VSM e.g. the synchronous power controller (SPC), enable unifying various functionalities in a cascaded control scheme [116]. Various functionalities of the SPC such as current control, voltage control, power control, inertia emulation, droop control, and power oscillation damping have been demonstrated experimentally [116].

Similar to a synchronous machine, the SPC can damp SSR through its virtual admittance and virtual inertia. For adjusting the damping active power injected by the SPC, an analytical method is presented in [26]. As demonstrated in [26], the participation of the SPC in suppressing the low-frequency oscillations might be improved by properly setting the values of the virtual inertia and the damping coefficient. However, because the damping coefficient also dictates the dynamic characteristics of the SPC, decreasing the value of the damping ratio as proposed in [26] certainly degrades the overall behaviours of the GFMC. To address such a drawback, frequency selective strategies have also been suggested in [117] and [118]. However, there are not any studies that cope with the implementation of such frequency-selective SSR damper for GFMC systematically.

This chapter presents a new control concept, i.e. multi-rotor virtual machine (MRVM), for enhancing the damping performance of GFMC while ensuring its overall dynamic behaviour. That is, the MRVM take advantage of the high flexibility of the power converters to implement virtual machine with multiple rotors to deal with different oscillation mode simultaneously. Indeed, by implementing several rotors (instead of only one as in the case of VSM), the MRVM can be adjusted to damp selectively low-frequency modes. Frequency-domain techniques and modal analyses approaches are used to obtain the optimal damping for the MRVM. The MRVM is validated in simulation with the three-machine infinite bus (3MIB).

5.2 Damping SSR with Grid-Forming Converters

For studying the performance of GFMC in coping with LFO, the SPC-based GFMC (SPC-GFMC) is taken into consideration. Generally, the SPC-GFMC is made up of three control loops to provide three types of grid functionalities, shown in Fig. 5.1. The current controller makes sure that the currents exchanged with the grid track their references asymptotically with minimal settling times. As required in many grid codes [119], the

current controller also needs to minimize the harmonic terms in the injected currents regardless of the grid voltage conditions. Similarly, the voltage controller, which is based on a virtual admittance, can be set to provide reactive power support [120]. The virtual admittance can be seen as the stator windings of a synchronous machine. The power controller of the SPC-GFMC usually emulates the electromechanical behaviour of a synchronous machine through the implementation of the swing equation. This controller provides most of the grid functionalities such as grid synchronization, inertia emulation, and/or power oscillation damping etc.

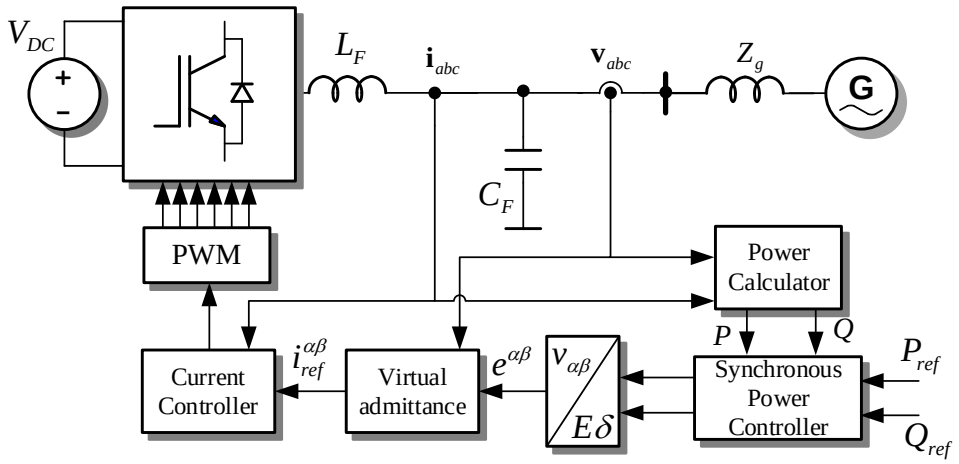

Fig. 5.1. SPC-based GFMC connected to an infinite bus.

Because these three control loops are almost dynamically decoupled from each other, the dynamics of the current and voltage control loops can be omitted when designing the power controller of the SPC-GFMC [121]. Such an assumption is valid in most cases, because LFO often ranges from 0.1 to 2Hz [122], while current and voltage dynamics belong to a much higher frequency spectrum. As suggested by [121], the SPC-GFMC can be modelled for small-signal analysis as in Fig. 5.2, where H and D demote the virtual inertia constant and virtual damping coefficient, respectively, ω_g^0 denotes the nominal grid frequency, $\Delta\delta$ is the virtual rotor angle, ΔP_e is the tracking error in the active power, and Y_v denotes the virtual admittance. Since the dynamics of the virtual admittance is considerably faster than that of the power controller, only the RMS value of the virtual admittance is taken into account for the sake of simplicity. Remake that the SPC-GFMC has 2 inputs, namely the active power reference ΔP_{ref} and the grid frequency $\Delta\omega_g$. The only output of the system is the active power exchanged with the grid ΔP.

From the small-signal model in Fig. 5.2, the closed-loop transfer functions from the inputs to the output can be obtained as in the following:

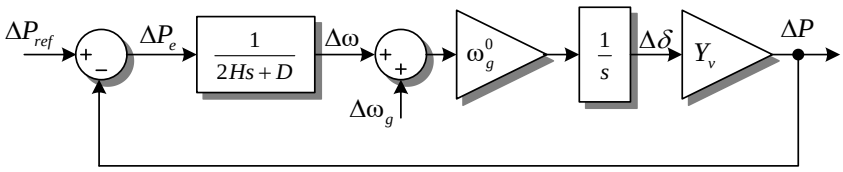

Fig. 5.2. Small-signal model of SPC-GFMC.

$$G_{P2P}(s) = \frac{Y_v \omega_g^0}{2Hs^2 + Ds + Y_v \omega_g^0}, \tag{5.1}$$

$$G_{\omega 2P}(s) = \frac{2HY_v \omega_g^0 s + DY_v \omega_g^0}{2Hs^2 + Ds + Y_v \omega_g^0}. \tag{5.2}$$

Because (5.1) and (5.2) are in the form of a second-order transfer function which is often given by the following transfer function;

$$G(s) = \frac{\omega_n^2}{s^2 + 2\zeta\omega_n s + \omega_n^2}, \tag{5.3}$$

where ζ and ω_n denotes the damping ratio and natural frequency.

In practice, the damping of the system is often specified by damping ratio ζ instead of the damping coefficient *D*. Consequently, the damping coefficient *D* can be calculated from the damping ratio ζ using (5.3) as follows:

$$D = \sqrt{8HY_v \zeta^2 \omega_g^0}. \tag{5.4}$$

Fig. 5.3 shows the frequency characteristics of the closed-loop system from grid frequency input $\Delta\omega_g$ to output active power ΔP. For achieving a well-damped dynamic response for the SPC-GFMC, the damping ratio ζ is usually chosen to be $\zeta = 0.71$. As illustrated in Fig. 5.4 which shows the step response of the SPC-GFMC according to (5.1), the step response of the active power is rather stable with negligible overshoot with the chosen value of the damping ratio. Additionally, Fig. 5.3 shows that the SPC-GFMC exhibits high gain at low frequencies i.e. below 1 Hz. This indicates that the SPC-GFMC can provide effectively damping to SSR. Such damping, however, can be insignificant to SSR whose frequencies is higher than 1 Hz because of the considerable phase difference at higher frequencies. Indeed, the phase lag reaches around 45 degrees at 1.5 Hz.

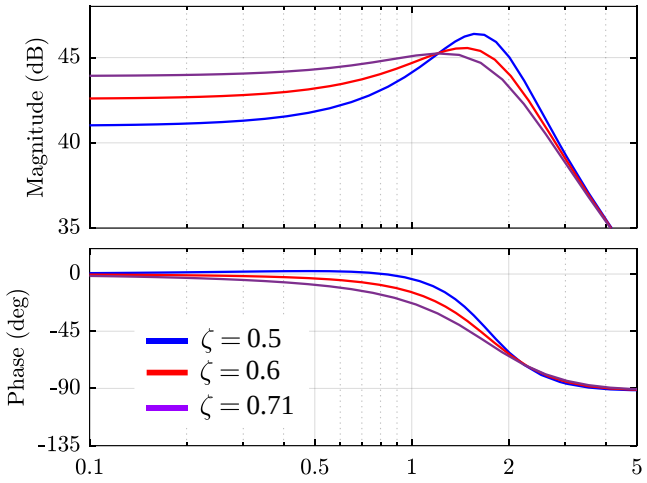

Fig. 5.3. Frequency response of SPC-GFM connverter according to (5.2).

For improving the dynamic response of the SPC-GFM converter, a tuning approach is presented in [26]. Basically, such an approach tries to decrease the phase delay by tuning the controller damping ratio ζ. As depicted in Fig. 5.3, the phase delay reduces as soon as the damping ratio becomes slower. This results in improved damping at higher frequencies, i.e. above 1 Hz. This approach might be useful in applications where damping of low-frequency oscillations is the main objective. However, it can be clearly seen from Fig. 5.4 that decreasing the damping ratio adversely affects the overall dynamic performance of the SPC-GFMC. Indeed, the lower the damping ratio the higher the overshoot of the step response. In other words, this method increases the damping capabilities by reducing the overall system stability. This is not desirable as system stability needs to be ensured at all times. Moreover, decreasing the damping ratio also reduces the gain at lower frequencies, causing the degradation of damping performance against interarea modes. Hence, this method is not suitable for dealing with multiple modes simultaneously.

On the other hand, the work in [123] demonstrated that frequency-selective damping methods might offer better performance in suppressing LFO. Motivated by such a demonstration, this chapter coins a new concept, namely MRVM, to fully exploit the virtualization paradigm in controlling GFMC. That is, instead of emulating a conventional VSM, MRVM will implement a virtual machine that consists of multiple virtual rotors to attenuate simultaneously several modes in the power system with a high degree of controllability.

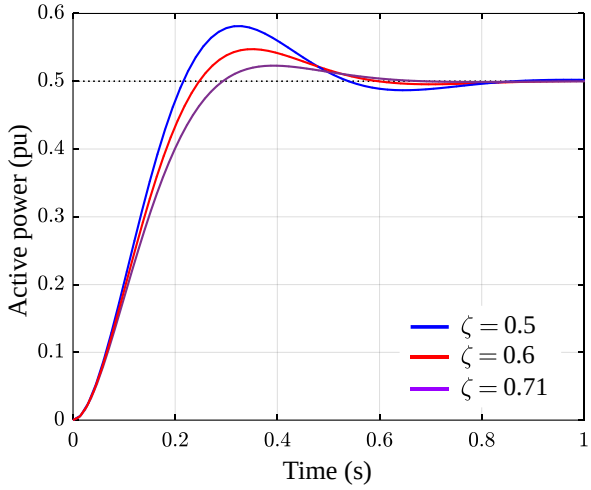

Fig. 5.4. SPC-GFM converter for a step change of 0.5 pu in active power.

Assuming that frequencies of the oscillatory modes are well-detected by using the techniques presents in [117] and [124], this chapter will be focused on analysing the operation and design of the MRVM, and not the detection of the oscillations' frequency.

5.3 Multi-Rotor Power Oscillation Damper

5.3.1 Control Structure

Fig. 5.5 shows the overall concept of the configuration of the MRVM. Like synchronous generations, the MRVM consists of two parts, namely the mechanical part and the electrical part. The latter aims to emulate the electromagnetic characteristic of an SG. For such a purpose, the electrical part implements a virtual admittance block. The dynamic behaviour of this block can be adjusted through the virtual resistance R_v and the virtual inductance L_v. Similarly, the mechanical part of the MRVM is responsible for the electromechanical behaviour of the MRMV-GFM converter.

Conventionally, a GFM algorithm tries to emulate the dynamics of an SG by implementing a swing equation of some kind. This approach is quite effective and simple for implementation. However, as pointed out in the previous section, the swing equation poses certain limitations in dealing with SSR at higher frequencies. Unlike SGs, the control system of power converters is more flexible which can realize more complex transfer functions. Motivated by this rationale, the MRVM aims to implement an electromechanical layer that is made up of several swing equations. Each of the equations can be seen as a virtual rotor that is tailored to achieve a specific objective. For instance, one of the virtual rotors is tuned to provide exclusively for synchronization and inertia response, while other

virtual rotors are parameterized to target underdamped oscillatory modes. Such design will allow not only provide multiple control functions but also give a higher level of flexibility in configuring such functions.

As can be seen from Fig. 5.5, the virtual rotor can be easily realized by using the well-known swing equation or any other transfer functions. It is worth pointing out that these virtual rotors are assumed to be operating in parallel producing synchronous frequencies. Such synchronous frequencies are combined to generate the net synchronous frequency which is used as an input for the electromagnetic layer. Due to the fact that the virtual rotors are designed for a specific frequency, it is vital to separate the input signal of each rotor such that the frequency components in the input signals of virtual rotors are not identical. Otherwise, the dynamics of the rotor might be strongly coupled resulting in a highly complex control loop that might not be easy to be parameterized.

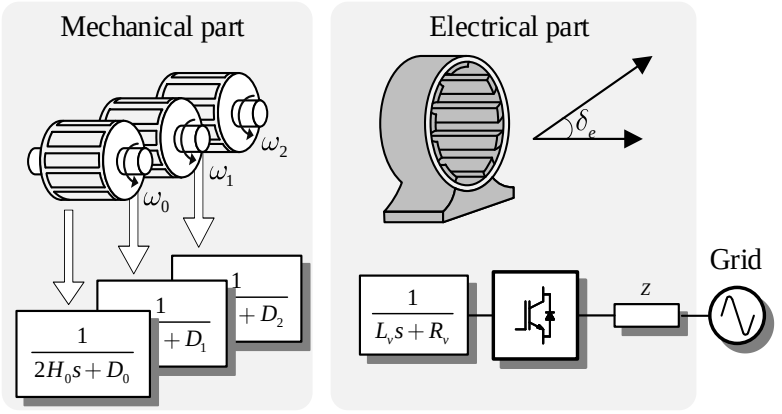

Fig. 5.5. Conceptual presentation of the proposed MRVM.

More specifically, the primary rotor, rotating at the frequency of ω_0, can be configured by selecting properly the parameter set $\{H_0, D_0\}$ to provide the synchronization and inertia response for the GFM converter. At the same time, the remaining virtual rotors, rotating at the frequencies of ω_1 and ω_2, can be adjusted with the parameter sets $\{H_1, D_1\}$ and $\{H_2, D_2\}$, respectively, to provide a controllable damping effect to different underdamped oscillatory modes. By doing so, the damping participation of MRVM-GFM converter to SSR can be maximized in a selective manner without comprising substantially the overall dynamic performance of the power converter.

The detailed realization of the MRVM-GFM converter is shown in Fig. 5.6. While the electromagnetic layer, i.e. the virtual admittance is inherent from the SPC-GFM converter, the structure of the electromechanical layer is significantly modified to cope with multiple

SSR in the power systems. Besides the additional virtual rotors for oscillatory modes, a decoupling network is also employed for providing signal filtering. The decoupling network is made of two band-pass filters and crossed feedback interconnection for the cancellation of filtered signals in the other branch to improve the overall filtering performance. The decoupling network is indeed important to decouple the dynamics among the virtual rotors. As a result, the decoupling network makes selective attenuation of the underdamped modes possible. Moreover, by separating the dynamics of the virtual rotors, the tuning of the control parameters is also significantly simplified.

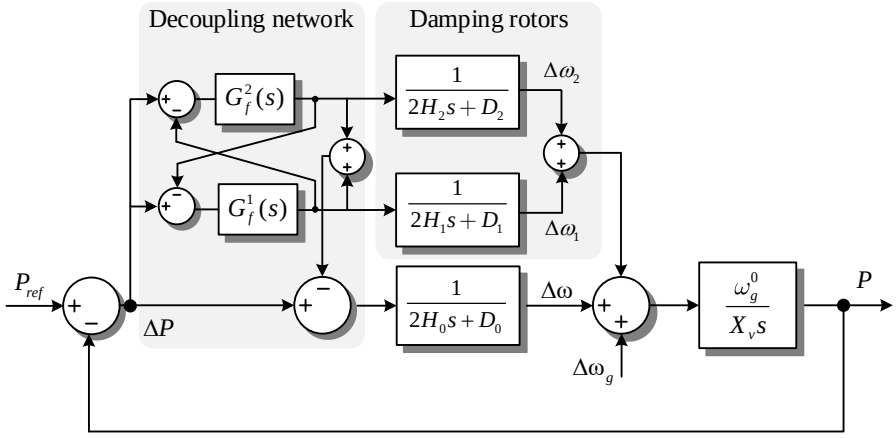

Fig. 5.6. Detailed block diagram of the proposed MRVM.

5.3.2 Parameter Tuning

In general, several underdamped modes exist in power systems. Electromechanical modes, often determined by generators' inertia, line impedances, governors, and AVRs, are in the frequency range of 0.1 to 2 Hz. According to the nature of the electromechanical interactions among the generators or the group of generators, these electromechanical modes are divided into intra-area (local) and inter-area modes. The typical oscillatory frequencies of interarea modes range from 0.1 to 0.8 Hz. Similarly, the power oscillations among generators in the same electrical normally fall into a higher range frequency e.g. from 0.7 to 2 Hz [125].

For the sake of simplicity, two electromechanical modes, local (1.25 Hz) and interarea (0.4 Hz), are considered for demonstrating the working principle of the MRVM-GFM strategy. As explained earlier, these frequencies can be estimated in real-time by a prediction algorithm and thus such frequencies are assumed to be known in this Chapter. It is obvious from Fig. 5.7 that the conventional SPC-GFM converter can only produce

significant damping to interarea mode thanks to the high gain and low phase lag at 0.4 Hz. Nevertheless, the local mode is clearly out of the scope of the SPC-GFM controller because of the significant phase displacement i.e. nearly 40 degrees.

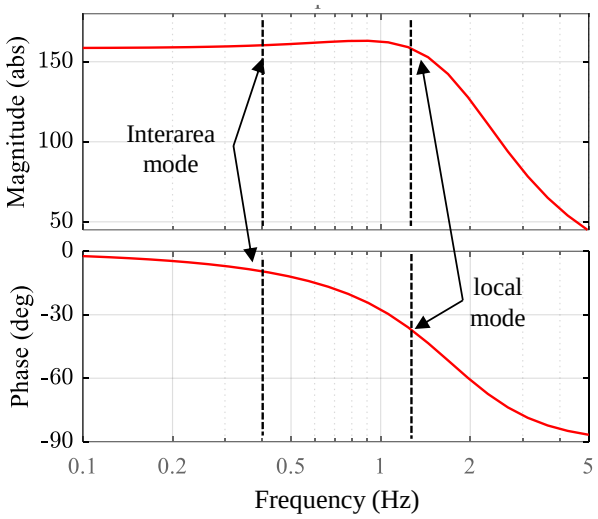

Fig. 5.7. Frequency response of an SPC-GFMC and target LFO modes.

For the sake of simplicity, the electromagnetic layer of the MRVM can be compactly rewritten as:

$$G_{ma}(s) = \frac{\omega_g^0}{X_v s}, \tag{5.5}$$

with X_v being the virtual impedance.

Similarly, the virtual rotors realizing the swing equations can be mathematically represented as:

$$G_{sw,i} = \frac{1}{2H_i s + D_i}, \tag{5.6}$$

where subscript $i = 0$, $i = 1$, and $i = 2$ indicates the parameter set for the virtual rotors targeting the overall dynamics, the interarea mode, and the local mode, respectively.

In addition to the crossed-feedback interconnection of filtered signals, the decoupling network also implements a band-pass filter for each virtual rotor. The band-pass filters are represented in terms of transfer functions as:

$$G_{bp}^{1}(s)=\frac{2\xi_1\omega_1 s}{s^2+2\xi_1\omega_1 s+\omega_1^2}, \tag{5.7}$$

$$G_{bp}^{2}(s)=\frac{2\xi_2\omega_2 s}{s^2+2\xi_2\omega_2 s+\omega_2^2}, \tag{5.8}$$

where ω_1 and ω_2 are desired frequencies, and ξ_1 and ξ_2 are the damping ratios of the filters.

To assist the controller analyses and parameter tuning, Fig. 5.6 is rearranged as in Fig. 5.8 in which the coupling interactions are replaced by transfer functions. For doing so, the decoupling network is equivalently rewritten in terms of transfer functions as in the following:

$$G_{f1}(s)=\frac{G_{bp1}-G_{bp1}G_{bp2}}{1-G_{bp1}G_{bp2}}, \tag{5.9}$$

$$G_{f2}(s)=\frac{G_{bp2}-G_{bp1}G_{bp2}}{1-G_{bp1}G_{bp2}}, \tag{5.10}$$

$$G_{f0}(s)=1-G_{f1}-G_{f2}. \tag{5.11}$$

It is worth remarking that the Laplace operator *s* is omitted on the right-hand side of (5.9), (5.10), (5.11) for a more simple presentation.

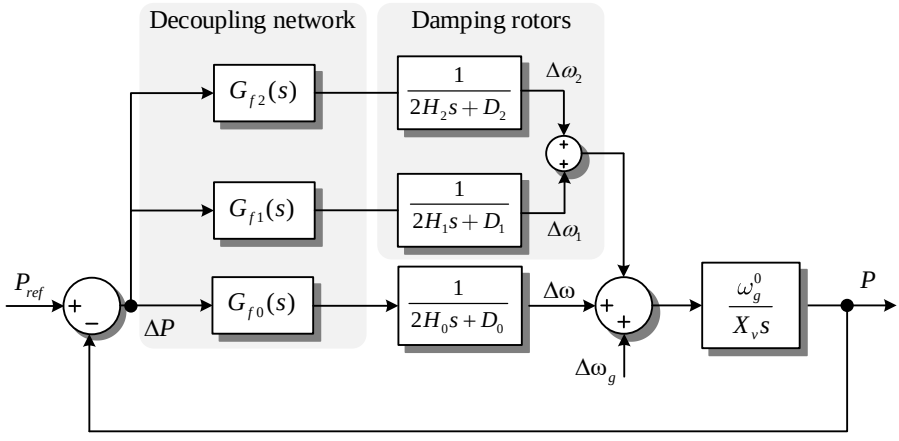

Fig. 5.8. Equivalent block diagram of the MRVM-GFM converter.

According to (5.5), (5.6), and Fig. 5.8, the closed-loop transfer functions of the MRVM-GFM controller can be obtained as:

$$G_{P2P}^{MRVM}(s)=\frac{G_{ma}(G_{f0}G_{sw0}+G_{f1}G_{sw1}+G_{f2}G_{sw2})}{1+G_{ma}(G_{f0}G_{sw0}+G_{f1}G_{sw1}+G_{f2}G_{sw2})}, \tag{5.12}$$

$$G_{\omega 2P}^{MRVM}(s)=\frac{G_{ma}}{1+G_{ma}(G_{f0}G_{sw0}+G_{f1}G_{sw1}+G_{f2}G_{sw2})}. \tag{5.13}$$

From the control diagram shown in Fig. 5.8, the control parameters can be adjusted to optimize the damping contribution of the MRVM-GFM controller. To streamline the tuning procedure for the rotors' parameters, it is convenient to select the damping ratio of the band-pass filters as the standard value of $1/\sqrt{2}$. Different from the band-pass filters which are only employed for implementing the decoupling network, the swing equation for each virtual rotor dictates the damping participation of the MRVM-GFM controller to a specific mode. Since there are three swing equations in the MRVM, it is more straightforward to tune their parameters one after another. Even though it is not mandatory, the virtual rotors for most undamped modes can be adjusted first to meet the required stability requirement. Then, one can continue to tune other virtual rotors.

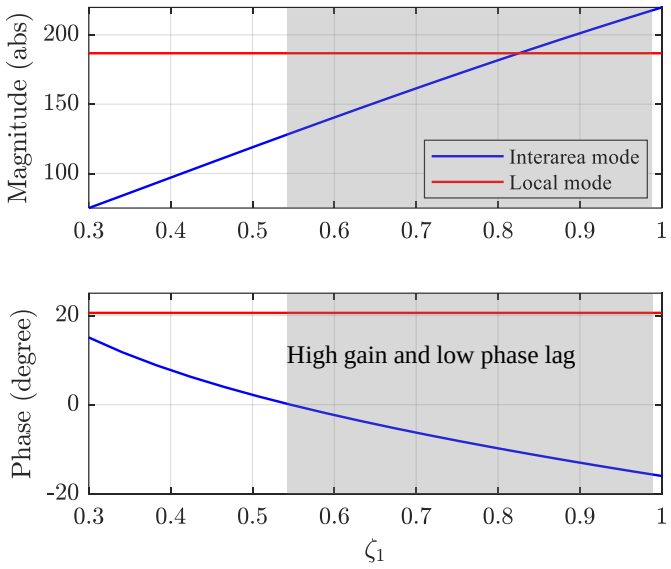

Fig. 5.9. Phase and gain at 0.4 Hz (blue) and 1.25 Hz (red) for different values of ζ_1

To demonstrate the tuning procedure, the parameter set of the VMRM-GFM are given as in Table 5.1. Remark that the final values of ζ_1 and ζ_2 are calculated at the end of the tuning process. Even though all the parameters are adjustable, only two parameters are necessary for determining the damping participation of the MRVM-GFM converter. These parameters are the damping ratios of the additional virtual rotors. From Fig. 5.8 and Table

5.1, the frequency responses of the MRVM-GFM converter obtained from the grid frequency ω_g to the output power *P* can be illustrated as in Fig. 5.9 and Fig. 5.10. The former figure shows the gain and phase displacement of the MRVM-GFM converter at targeted modes 0.4 Hz (inter-area mode) and 1.25 Hz (local mode) when the damping ratio ζ_1 is increased from 0.2 to 1. It can be easily seen that as ζ_1 varied, only the gain and phase displacement of the converter at 0.4 Hz are changed, meaning that the damping ratio ζ_1 alters mainly the dynamic responses of the VMRM-GFM converter to the oscillations at the frequency of 0.4 Hz. This is possible because of the decoupling network. Furthermore, it is obvious that the damping ratio ζ_1 is to some extent proportional to closed-loop gain and inversely proportional to phase displacement. In fact, as the damping ratio increases, the gain of the MRVM-GFM converter also increases whereas its phase displacement declines. According to [122], the damping to SSR is maximized when the phase displacement approaches zero and the gain is as high as possible. Such a requirement is roughly translated into the shadowed region in Fig. 5.9. In such a region, the gain is considerably high while the phase delay is noticeably low. Indeed, this region can be considered as a generic setting of the MRVM-GFM converter in case the details of the grid model are unknown.

Table 5.1. Parameters of the MRVM

Symbol	**Definition**	**Tuning** ζ_1	**Tuning** ζ_2	**Final value**
ω_1	Centre frequency of band-pass filter (rad/s)	0.4	0.4	0.4
ξ_1	Damping ratio of band-pass filter	0.707	0.707	0.707
ω_2	Centre frequency of band-pass filter (rad/s)	1.25	1.25	1.25
ξ_2	Damping ratio of band-pass filter	0.707	0.707	0.707
H_0	Inertia constant (s)	5	5	5
ζ_0	Damping ratio	0.707	0.707	0.707
H_1	Inertia constant (s)	5	5	5
ζ_1	Damping ratio	[0.3, 1]	0.707	0.8
H_2	Inertia constant (s)	5	5	5
ζ_2	Damping ratio	0.707	[0.2, 1]	0.31
ω_g^0	Grid nominal frequency (Hz)	60	60	60
X_v	Virtual impedance (pu)	0.3	0.3	0.3

As soon as appropriate damping for the interarea mode is determined, a similar procedure can be conducted to identify the most suitable value for the damping ratio ζ_2. Fig. 5.10 illustrates the frequency response of the VRVM-GFM converter at 0.4 Hz and 1.25 Hz for different values of the damping ratio ζ_2. Thanks to the decoupling network, the damping ratio ζ_2 affects only the gain and phase displacement of the VRMR-GFM converter at 1.25 Hz. From such frequency characteristics, one can easily determine the feasible region for the damping ratio ζ_2. Indeed, the shadowed region shown in Fig. 5.10 specifies the range of values for ζ_2 where the phase displacement is negligible, and the gain is highest. As shown in the figure, since the variation in gain is unremarkable, the overall damping participation is largely dictated by the value of the phase delay. Such a tuning procedure is not only useful to identify tentative parameter sets for the MRVM-GFM converter but also is essential for understanding the working principles of the controller.

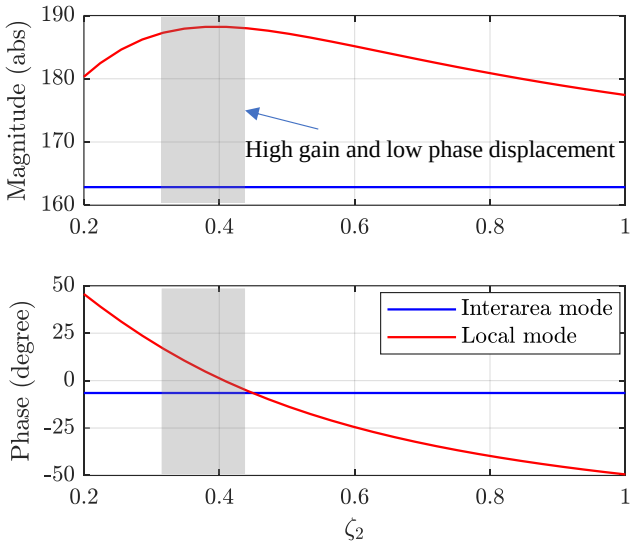

Fig. 5.10. Phase and gain at 0.4 Hz (blue) and 1.25 Hz (red) for different values of ζ_2

The aforementioned parameter tuning procedure can be summarized as follows:

Input parameters: H_0, ζ_0, X_v, ω_g^0, ω_1, and ω_2

Tuning parameters: H_1, H_2, ζ_1 or D_1, ζ_2 or D_2, ξ_1, and ξ_2

Step 1: set $\xi_1 = \xi_2 = 1/\sqrt{2}$ to have well-damped filters.

Step 2: set $H_1 = H_2 = H_0$ for simplification.

Step 3: set $\zeta_2 = \zeta_0$ and use (5.13) to find a high damping range for the damping ratio ζ_1.

Step 4: Select a value for ζ_1, then use (5.13) to high damping range for the damping ratio. ζ_2.

Step 5: If the simulation model of the target power system is available, *step* 3 and *step* 4 can be repeated with the modal analysis approach to fine-tune the values of ζ_1 and ζ_2, which will be illustrated in the following section.

It is to remark that there are in fact only two tuning parameters, ζ_1 and ζ_2, after the simplification made in *step* 1 and *step* 2.

5.3.3 Simulation-based analysis

To validate the proposed MRVM, the three-machine-infinite-bus (3MIB) system is adopted. 3MIB is an IEEE benchmark system that is commonly used to assess PSS performance when multiple modes are considered [126]. The parameters of the generators are detailed in Table 5.2. Overall, the 3MIB system is made up of three generators (G1, G2, and G3) connected to an infinite bus. Due to insufficient damping, generators G1 and G2 oscillate against generator G3, resulting in local or intra-area oscillations at 1.25 Hz. In addition, the three generators oscillate against the infinite bus at the frequency of 0.4 Hz forming an interarea mode. To represent renewable generations in the 3MIB, a grid-connected power converter of 200 MVA is connected to bus B5 through a step-up transformer T7_5. The modified 3MIB for validating the MRVM-GFM is shown in Fig. 5.11. The control parameters of the MRVM are adopted from Table 5.1 and are the same for all simulations unless otherwise specified. The entire system is modelled and simulated by using the DIgSILENT PowerFactory software to obtain the eigenvalues and time-domain results. The eigenvalue loci are obtained by running hundreds of simulations for all possible values of the damping ratios.

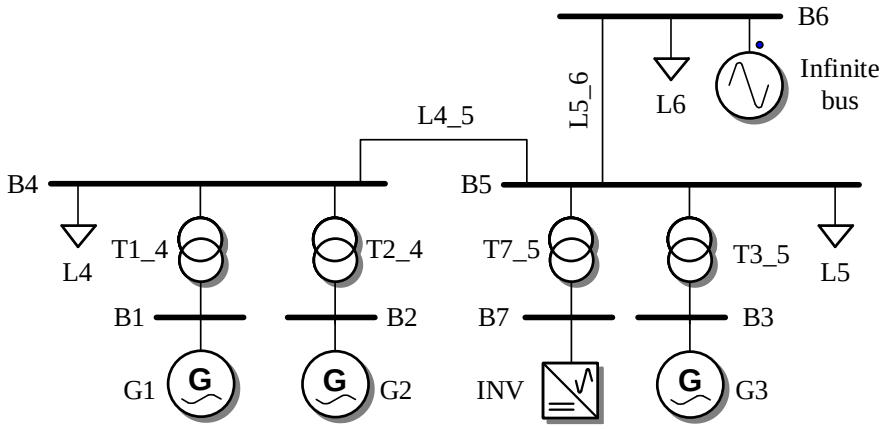

Fig. 5.11. Modified three-machine-infinite-bus system.

Fig. 5.12 shows the dominant modes of the modified 3MIB system for the two cases: (i) base case in which the power converter is equipped with a GFL controller, and (ii) when the conventional SPC-GFM controller is used for the power converter. It is clear from Fig.

5.12 that the system suffers from small-signal instability because the real part of the interarea mode has a positive value. Once the SPC-GFM controller is used, the interarea mode shifts towards the stable region resulting in a damping ratio of 8%. This improvement in damping indicates that the SPC-GFM can stabilize the interarea mode. On the contrary, the local mode is nearly unaffected by the SPC-GFM controller. This is in fact matching with the conclusion drawn in the previous section that the SPC-GFM controller is unable to dampen oscillatory modes whose frequency is higher than 1 Hz. Indeed, the SPC-GFM only moves the damping of local mode to just above 3% which is substantially lower requirements according to grid codes where at least 5% damping is required [127].

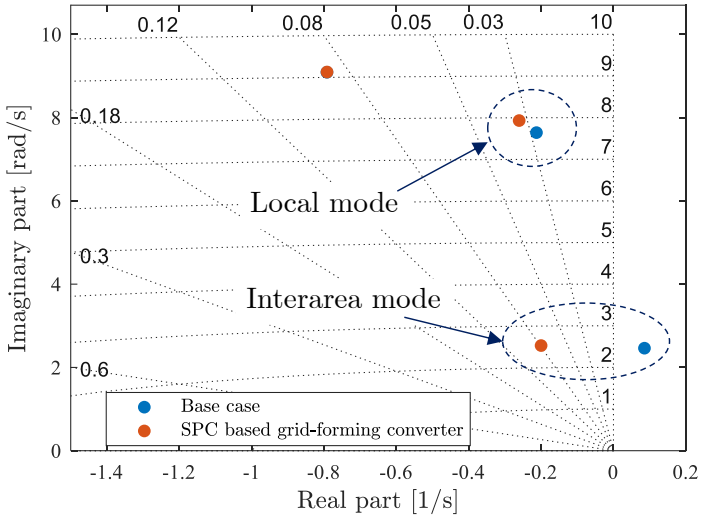

Fig. 5.12. Low-frequency modes of the modified 3MIB system.

To tune the parameters of the MRVM-GFM controller, the feasible ranges for the damping ratio in the previous section can be employed if the exact knowledge of the power system model is unavailable. However, when the system model is available, the values of the damping ratios for the MRVM-GFM controller can be further refined using the eigenvalue loci. For instance, Fig. 5.13 shows the trajectories of dominant modes when the damping ratio ζ_1 is increased from 0.4 to 1. It is clear that the damping ratio of interarea mode is improved from around 3% to approximately 11% by increasing ζ_1. As soon as the ζ_1 reach 0.9, the damping of interarea mode begins to reduce because of the increment in the phase displacement as discussed in the previous section. Thus, the damping ratio can be eventually selected as $\zeta_1 = 0.8$. Compared to the SPC-GFM controller, the damping of interarea mode is moved from 8% to 11%. This result confirms that the MRVM-GFM controller does not only help system stability but also it gives a certain degree of freedom

to achieve the desired damping. Remarkably, the characteristics of local mode are nearly untouched by varying ζ_1.

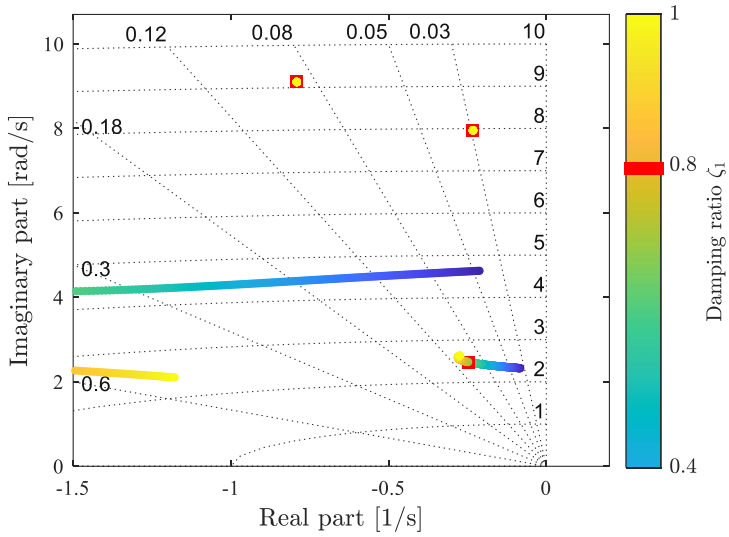

Fig. 5.13. Eigenvalue locus of the 3MIB system when MRVM is employed and ζ_1 is varied.

Provided that $\zeta_1 = 0.8$, Fig. 5.14 shows the eigenvalue trajectories of the modified 3MIB system for different settings of ζ_2. It can be observed that ζ_2 can substantially enhance the damping ratio of the local mode. That is, as the value of ζ_2 is being reduced, the damping ratio of local mode is moved from 2% to nearly 6.5% at $\zeta_2 = 0.31$. Such enhancement of the damping ratio reveals that the MRVM-GFM controller performs significantly better than the SPC-GFM controller which can only increase the damping ratio to just above 3%. Furthermore, there is a certain coupling effect between the damping ratio ζ_2 and the interarea mode even though such coupling effect is negligible. This coupling effect is, however, an advantage because it moves the interarea mode further to the stable plane, bringing the damping ratio of the interarea mode to 12%.

Fig. 5.13 and Fig. 5.14 indicates that (i) the feasible regions calculated by using the single converter infinite bus system in Fig. 5.6 encloses the optimal values for the MRVM-GFM even with an actual grid; (ii) the tuning of the control parameters is nearly independent meaning that the virtual rotors can be individually designed; (iii) MRVM-GFM controller is more effective than conventional GFM controller in dealing with SSR.

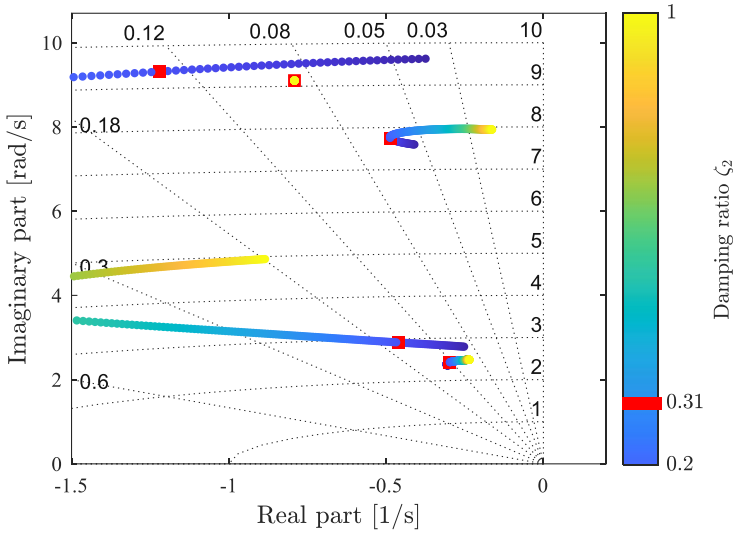

Fig. 5.14. Eigenvalue locus of the 3MIB system when MRVM is employed and ζ_2 is varied.

Table 5.2. Parameters of the generators

Parameters	Generator		
	G1	G2	G3
S [MW]	1560	1560	890
f_n [Hz]	60	60	60
X_d [pu]	0.89	0.89	1.72
X_q [pu]	0.66	0.66	1.68
X'_d [pu]	0.36	0.36	0.49
X'_q [pu]	0.36	0.36	0.8
X''_d [pu]	0.29	0.29	0.34
X''_q [pu]	0.29	0.29	0.34
X_l [pu]	0.28	0.28	0.27
R_a [pu]	0	0	0
H_s [s]	4.5	4.5	3.86
T'_{d0} [s]	5.1	5.1	5.3
T''_{d0} [s]	0.06	0.06	0.048
T''_{q0} [s]	0.094	0.094	0.066

To further validate the performance of the MRVM-GFM controller, time-domain simulations of the modified 3MIB system have been carried out. Fig. 5.15 presents the simulation results of the system considering different controllers for the grid-connected converter. The conducted test cases are: (i) GFL controller, (ii) SPC-GFM controller, (iii) MRVM-GFM controller with only one virtual rotor targeting the interarea mode, and (iv) MRVM-GFM controller with two virtual rotors targeting both interarea mode and local mode. To emulate a small-signal perturbation, a reactive load of 50 Mvar is connected to B5 at t = 1 second and then disconnected at t = 1.1 seconds.

Fig. 5.15 (a) and Fig. 5.15 (b) present the active power injected by the generators G1, G2, and G3. Similarly, Fig. 5.15 (c) shows the active power delivered by the grid-connected power converter. It is shown in the base case that the system suffers from sustained oscillations with amplified amplitudes. Such instability dynamics is attributed to the undamped mode creating weak coupling between areas. On the contrary, the SPC-GFM controller is able to stabilize the interarea mode bringing the system into a stable operation. Nevertheless, since the SPC-GFM controller is unable to increase the damping ratio of the local mode, the local SSR is maintained for an extended period of time. Such oscillations can be seen more clearly in the output power of generators G1 and G2. Similarly, minor improvement to the damping ratio of interarea mode can be observed when the MRVM-GFM controller is tuned for ω_1. When the MRVM-GFM controller tuned at ω_1 and ω_2 is activated, both local and interarea interactions are enhanced. In fact, power oscillations entirely disappear after 8 seconds instead of 15 seconds as in the case of the SPC-GFM controller. Fig. 5.15 (c) also indicates that the MRVM-GFM controller reduces the power oscillations in the injected active power of the power converter. As a result, these results validate that the MRVM-GFM controller can provide superior performance over conventional GFM controllers, especially in terms of suppressing power oscillations.

In addition to the improvement in damping ratio at critical modes, Fig. 5.16 also reveals that the MRVM-GFM controller also improves the transient performance of the power converter. That is, the peak current at the beginning of the event is much lower when the MRVM-GFM controller is used. Additionally, the power oscillations at the output of the GFMC-GFM controller also decrease faster. It is clear that the MRVM-GFM controller boosts the transient response of the grid and the converter at the same time.

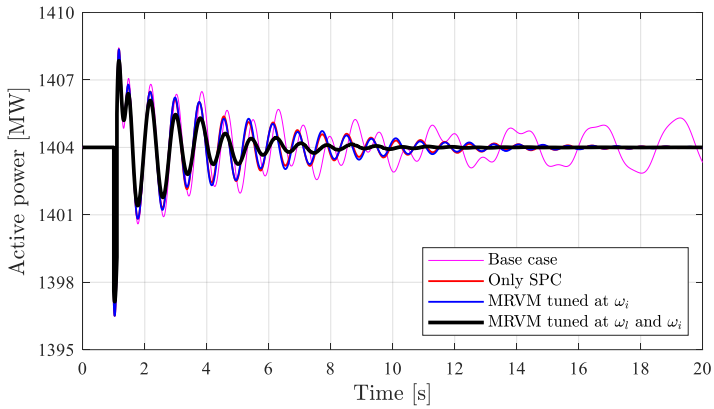

(a)

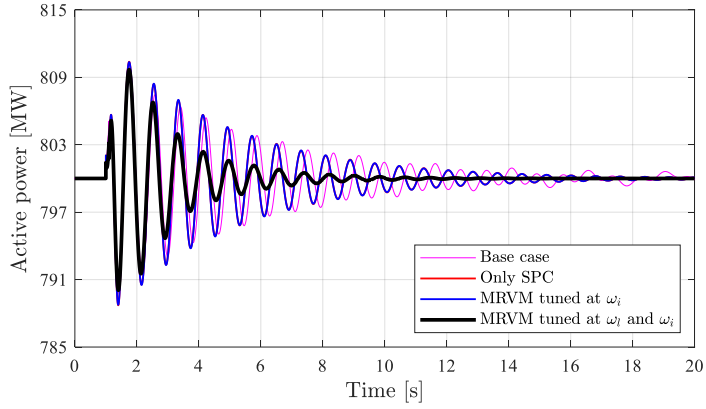

(b)

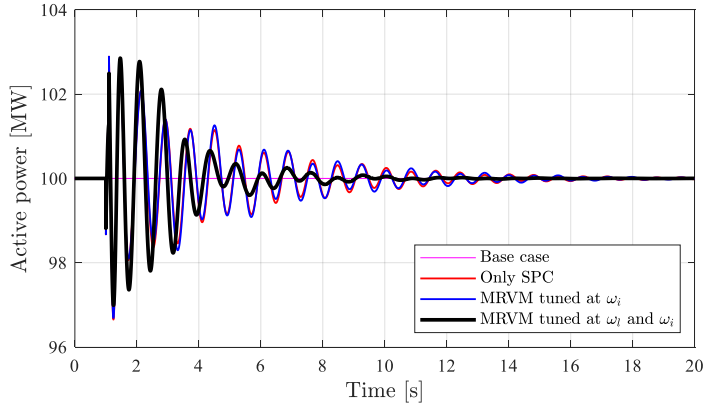

(c)

Fig. 5.15. Active power injected by the generators and the GFMC for different control strategies; (a) Active power of G1 and G2; (b) Active power of G3; (c) Active power of the converter.

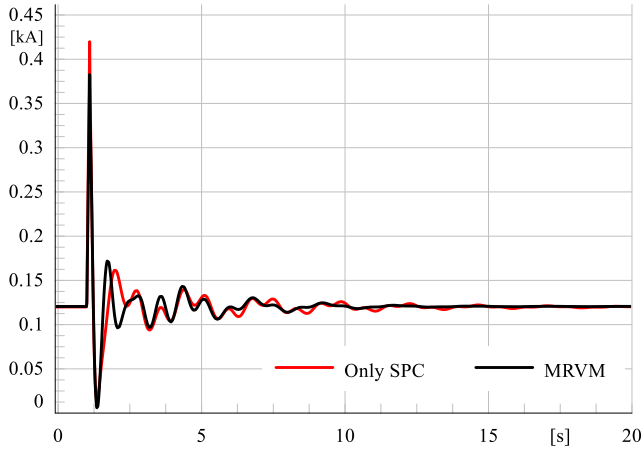

Fig. 5.16. Current injected by the GFMC with different controllers.

5.4 Conclusions

This chapter presents a multi-rotor virtual machine (MRVM) controller for boosting the damping capability of GFM converter to SSR in power systems. The MRVM-GFM controller is designed under the assumption that the electromagnetic layer e. g. voltage and current controllers are already properly tuned to cope with the abnormal operation of the electrical grid such as unbalanced and distorted voltages. The MRVM concept takes advantage of the flexibility offered by the microcontroller-based implementation of the control system to emulate a VSM with several rotors. Each virtual rotor is parameterized separately to obtain desired performance criteria such as overall electromechanical dynamics or SSR damping. Furthermore, a decoupling network for signal filtering is used to dynamically decouple the virtual rotors, aiming to not only improve the net performance but also facilitate the selection of the control parameters. Furthermore, this chapter also presents methodologies for choosing control parameters of the MRVM via frequency-domain and modal analyses. Simulation results using the IEEE 3MIB test system validate that the MRVM-GFM controller outperforms existing GFM strategies while offering a higher level of flexibility.

CHAPTER
6.

Conclusions and Future Works

6.1 Conclusions

This PhD thesis focuses on the control of power converters in modern power systems dominated by power electronics. More specifically, the main contributions of this PhD thesis are on the control and implementation of GFM converters. The research works conducted aim to extend the adaptation of the GFM concept in actual applications and to further improve the performance of GFM in supporting the grid as well as in withstanding adverse grid conditions.

Through the analyses of popular implementations for GFM converters, it is obvious that most GFM control schemes are made up of two main layers: electromechanical and electromagnetic layers. Each of these layers can be formed by one or several controllers. In fact, the control structures for these layers are usually different from one another. Yet, the functionalities provided are substantially similar across various implementations. That is, the electromechanical layer is intended to deliver system-level functions such as inertia response, power oscillation damping and frequency regulation. To meet such dynamic requirements, the electromechanical layer is usually realized through emulation of the motion equation of an SG. Depending on the GFM implementation, the swing equation can be fully or partially emulated. Though partial implementation might bring about simplicity, its practicality is questionable due to the lack of flexibility. As demonstrated in the existing works, a lead-lag controller can also be used to provide virtual inertia, damping, and frequency droop simultaneously.

On the other hand, the electromagnetic layer mainly focuses on controlling local magnitudes such as voltage and current at the PCC level. Implementation for electromagnetic layers varies significantly between GFM implementations. Early GFM strategies employ open-loop voltage control, which is simple and easy to implement.

However, the open-loop structure does not offer any means to control and limit the injected current which is an important magnitude. Indeed, overcurrent operation could easily damage the switching devices. As a result, the current controller is highly desired for a GFM converter. To facilitate parallel operation, virtual admittance has been proved to be the most suitable implementation in terms of stability and digital implementation.

The synchronization method of GFM strategies also plays an important role in the stability of power converters. Currently, the GFM strategies employ either voltage-based or power-based methods. Voltage-based methods have been employed in the grid-connected converter for a long time, and therefore is a standard for power converters. However, it is well-known that voltage-based synchronization suffers from potential instability under weak grid conditions. Consequently, power-based synchronization is more popular for GFM converters, which is evident in Chapter 2. Overall, the SPC-GFM implementation surpasses other alternatives in terms of preferable control features.

One of the main contributions of this PhD thesis is the RVSC for the electromagnetic layer of a GFM converter. The main aim of the RVSC is to ensure the stable operation of the GFM in abnormal grid conditions. Since the RVSC considers only the current control loop of the power converter, it can be equipped to any of the GFM implementations to ensure that the GFM will be able to withstand undesired grid events. The RVSC is developed by using IMP to take into account grid impedance, voltage into consideration when tuning the controller gains. In addition, the LMI technique is also used to simplify the tuning of the controller. The performance of the RVSC is validated through simulation and experiments. The results point out that the RVSC is capable of dealing with extreme grid conditions as long as such conditions are modelled and integrated into the controller.

To eliminate the need for firmware modification to implement a GFM controller, an ESC is presented in Chapter 4. As described in this Chapter, the electromagnetic and electrical layer can be partially implemented in external control hardware to avoid control firmware modification. In fact, the analyses conducted in this chapter confirm that the electromechanical layer can be implemented for most of a GFL converter that is equipped with fieldbus communications. For power converters equipped with high bandwidth communication such as EtherCAT, part of electromagnetic layer e.g. virtual admittance could be also implemented on the external control hardware to provide additional functions such as islanding operation or resynchronization. Bearing this approach in mind, Chapter 4 presents simulation and experimental results demonstrating that the ESC could achieve control performance similar to what is provided by conventional GFM implementations.

To further exploit the use of power converter in supporting the grid, Chapter 5 presented a new concept for GFM converter. Indeed, an MRVM-GFM control scheme is developed to cope with SSR in power systems. It was demonstrated that a typical GFM converter can only damp oscillations up to 1 Hz. However, as more and more conventional power plants are being retired, system inertia continuous decreases. As the result, oscillation with higher frequencies among generation units in an electrical area will become more common. It has been demonstrated in Chapter 5 that the MRVM-GFM do not only extend the frequency range for SSR damping but also allow providing the damping selectively. The performance of the MRVM is analysed in the frequency domain by using the transfer function of the controller. In addition, the simulation of the MRVM-GFM is also validated in the 3MIB system by using the DIgSILENT PowerFactory software. The time-domain simulations reveal that the MRVM-GFM outperforms SPC-GFM when it comes to damping SSR.

Overall, this PhD thesis attempted to provide solutions for improving the performance of GFM converters in supporting the grid as well as in coping with undesired grid conditions. In addition, a new concept for implementing GFM functions on external control hardware was also put forth and studied. The above concepts and designs are to some extent validated through simulation and experiments.

6.2 Future Works

Due to the limitations in time and equipment, some of the concepts presented in this PhD thesis have not been fully explored. Further research pursuit on the basics of these concepts can be summarized as in the following.

The main advantage of the RVSC scheme is robustness and cost-effectiveness since a voltage sensor is not needed. In fact, the RVSC might be tailored to behave like a VSM by incorporating the swing equation into the controller model. In such a case, the RVSC can be used as a GFM controller for low-cost applications such as microinverter.

The design technique using IMP and LMI could be also extended to tune the entire control system of a GFM converter such that dynamic performance and robustness can be achieved at the same time.

As presented in Chapter 4, any parts of a GFM controller can be theoretically implemented on the external controller hardware. However, as also pointed out in this Chapter, the performance of the GFM will be heavily dependent on the communication bandwidth. Therefore, it would be essential to derive more concrete criteria for specifying the communication bandwidth needed for each control function. For instance, it was not yet

conclusive from Chapter 4 what is the maximum allowable delay for a controller in the electromagnetic layer.

Furthermore, it is important to take into account package dropout, network congestion, and communication failure in the design of the ESC, at least for protective purposes. Similar, depending on the network architecture the reference might not able to reach target converters at the same time which might give rise to unsynchronized setpoints for the power converters. Such an issue should be further investigated when dealing with renewable power plants consisting of hundreds of converters.

Even though the MRVM-GFM showed promising results in the 3MIB system, validation with a bigger system is needed to further confirm the feasibility of the controller. In this regard, experimental works are also needed to assess the working of the controller in a real environment.

The MRVM-GFM can be roughly tuned by using the controller transfer function. Yet as shown in Chapter 5, the controller performance is much better after being fine-tuned with the grid model. As the grid configuration could even change during operation, auto-tune algorithm for MRVM-GFM controller could significantly facilitate actual deployment.

References

[1] United Nations, “Paris Agreement,” Paris, 2015.

[2] N. Hatziargyriou *et al.*, “Stability definitions and characterization of dynamic behavior in systems with high penetration of power electronic interfaced technologies,” 2020.

[3] P. Kundur, J. Paserba, and S. Vitet, “Overview on definition and classification of power system stability,” *CIGRE/IEEE PES Int. Symp. Qual. Secur. Electr. Power Deliv. Syst. CIGRE/PES 2003*, pp. 1–4, 2003.

[4] X. Wang and F. Blaabjerg, “Harmonic Stability in Power Electronic-Based Power Systems: Concept, Modeling, and Analysis,” *IEEE Trans. Smart Grid*, vol. 10, no. 3, pp. 2858–2870, 2019.

[5] M. Liserre, F. Blaabjerg, and S. Hansen, “Design and Control of an LCL-Filter-Based Three-Phase Active Rectifier,” *IEEE Trans. Ind. Appl.*, vol. 41, no. 5, pp. 1281–1291, Sep. 2005.

[6] N.-B. Lai and K.-H. Kim, “Robust Control Scheme for Three-phase Grid-connected Inverters with LCL-filter under Unbalanced and Distorted Grid Conditions,” *IEEE Trans. Energy Convers.*, vol. 8969, no. c, pp. 1–1, 2017.

[7] J. Driesen and K. Visscher, “Virtual synchronous generators,” *Power Energy Soc. Gen. Meet. Deliv. Electr. Energy 21st Century, 2008 IEEE*, pp. 1–3, 2008.

[8] N. W. Miller, M. Shao, S. Venkataraman, C. Loutan, and M. Rothleder, “Frequency response of California and WECC under high wind and solar conditions,” in *2012 IEEE Power and Energy Society General Meeting*, 2012, pp. 1–8.

[9] N. Miller, D. Lew, and R. Piwko, “Technology Capabilities for Fast Frequency Response,” 2017.

[10] D. Gautam and V. Vittal, “Impact of DFIG based wind turbine generators on transient and small signal stability of power systems,” in *2009 IEEE Power & Energy Society General Meeting*, 2009, pp. 1–6.

[11] M. J. Gibbard, P. Pourbeik, and D. J. Vowles, *Small-signal stability, control and dynamic performance of power systems*. University of Adelaide Press, 2015.

[12] “South Australian blackout costs business $367m, fears summer outages on way, lobby group says.,” *ABC NEWS*, New York, NY, USA, 2016.

[13] National Grid ESO, “Technical Report on the events of 9 August 2019,” 2019.

[14] IEA, “Renewables 2019,” Paris, 2019.

[15] REN21, “Renewables 2019 Global Status Report,” Paris: REN21 Secretariat, 2019.

[16] P. Christensen *et al.*, “High Penetration of Power Electronic Interfaced Power Sources and the Potential Contribution of Grid Forming Converters,” 2020.

[17] J. H. Eto *et al.*, “Research Roadmap on Grid-Forming Inverters.”

[18] J. Rocabert, A. Luna, F. Blaabjerg, and P. Rodríguez, “Control of Power Converters in AC Microgrids,” *IEEE Trans. Power Electron.*, vol. 27, no. 11, pp. 4734–4749, Nov. 2012.

[19] H. Han, X. Hou, J. Yang, J. Wu, M. Su, and J. M. Guerrero, “Review of power sharing control strategies for islanding operation of AC microgrids,” *IEEE Trans. Smart Grid*, vol. 7, no. 1, pp. 200–215, 2016.

[20] H.-P. Beck and R. Hesse, “Virtual synchronous machine,” in *2007 9th International Conference on Electrical Power Quality and Utilisation*, 2007, pp. 1–6.

[21] P. Rodriguez, I. Candela, and A. Luna, “Control of PV generation systems using the synchronous power controller,” *2013 IEEE Energy Convers. Congr. Expo. ECCE 2013*, pp. 993–998, 2013.

[22] H. P. Beck and R. Hesse, “Virtual synchronous machine,” in *2007 9th International Conference on Electrical Power Quality and Utilisation, EPQU*, 2007, pp. 1–6.

[23] Q.-C. Zhong and G. Weiss, “Synchronverters: Inverters That Mimic Synchronous Generators,” *IEEE Trans. Ind. Electron.*, vol. 58, no. 4, pp. 1259–1267, Apr. 2011.

[24] V. Van Thong *et al.*, “Virtual synchronous generator: Laboratory scale results and field demonstration,” *2009 IEEE Bucharest PowerTech Innov. Ideas Towar. Electr. Grid Futur.*, pp. 2–7, 2009.

[25] W. Zhang, A. M. Cantarellas, J. Rocabert, A. Luna, and P. Rodriguez, “Synchronous Power Controller With Flexible Droop Characteristics for Renewable Power Generation Systems,” *IEEE Trans. Sustain. Energy*, vol. 7, no. 4, pp. 1572–1582, Oct. 2016.

[26] M. Abdollahi, J. I. Candela, J. Rocabert, M. A. Elsaharty, and P. Rodriguez, “Novel Analytical Method for Dynamic Design of Renewable SSG SPC Unit to Mitigate Low-Frequency Electromechanical Oscillations,” *IEEE Trans. Power Electron.*, vol. 35, no. 7, pp. 7532–7544, Jul. 2020.

[27] F. Milano, F. Dorfler, G. Hug, D. J. Hill, and G. Verbic, “Foundations and Challenges of Low-Inertia Systems (Invited Paper),” in *2018 Power Systems Computation Conference (PSCC)*, 2018, pp. 1–25.

[28] N. B. Lai and K. H. Kim, “An improved current control strategy for a grid-connected inverter under distorted grid conditions,” *Energies*, vol. 9, no. 3, p. 190, Mar. 2016.

[29] N. Lai and K.-H. Kim, “Robust Control Scheme for Three-Phase Grid-Connected Inverters With LCL -Filter Under Unbalanced and Distorted Grid Conditions,”

IEEE Trans. Energy Convers., vol. 33, no. 2, pp. 506–515, 2018.

[30] J. Rocabert, A. Luna, F. Blaabjerg, and P. Rodríguez, "Control of power converters in AC microgrids," *IEEE Trans. Power Electron.*, vol. 27, no. 11, pp. 4734–4749, 2012.

[31] R. Heese, H.-P. Beck, and D. Turschner, "Conditioning device for energy supply networks," 2006.

[32] R. Hesse, D. Turschner, and H.-P. Beck, "Micro grid stabilization using the virtual synchronous machine (VISMA)," *Renew. energy \& power Qual. J.*, vol. 1, pp. 676–681, 2009.

[33] Y. Chen, R. Hesse, D. Turschner, and H. P. Beck, "Dynamic properties of the virtual synchronous machine (VISMA)," *Renew. Energy Power Qual. J.*, pp. 755–759, May 2011.

[34] Y. Chen, R. Hesse, D. Turschner, and H.-P. Beck, "Comparison of methods for implementing virtual synchronous machine on inverters," *Renew. energy \& power Qual. J.*, pp. 734–739, 2012.

[35] J. Driesen and K. Visscher, "Virtual synchronous generators," in *2008 IEEE Power and Energy Society General Meeting - Conversion and Delivery of Electrical Energy in the 21st Century*, 2008, pp. 1–3.

[36] T. Vu Van *et al.*, "Virtual synchronous generator: An element of future grids," *IEEE PES Innov. Smart Grid Technol. Conf. Eur. ISGT Eur.*, pp. 1–7, 2010.

[37] T. Loix, S. De Breucker, P. Vanassche, J. Van Den Keybus, J. Driesen, and K. Visscher, "Layout and performance of the power electronic converter platform for the VSYNC project," *2009 IEEE Bucharest PowerTech Innov. Ideas Towar. Electr. Grid Futur.*, pp. 1–8, 2009.

[38] V. Karapanos, S. W. H. De Haan, and K. H. Zwetsloot, "Testing a Virtual Synchronous Generator in a Real Time Simulated Power System," *Int. Conf. Power Syst. Transients*, vol. 31, no. 0, 2011.

[39] Q. Zhong and G. Weiss, "Synchronverters: Inverters That Mimic Synchronous Generators," *IEEE Trans. Ind. Electron.*, vol. 58, no. 4, pp. 1259–1267, Apr. 2011.

[40] Qing-Chang Zhong, "Four-quadrant operation of AC machines powered by inverters that mimic synchronous generators," in *5th IET International Conference on Power Electronics, Machines and Drives (PEMD 2010)*, 2010, pp. 335–335.

[41] Phi-Long Nguyen, Q. Zhong, F. Blaabjerg, and J. M. Guerrero, "Synchronverter-based operation of STATCOM to Mimic Synchronous Condensers," in *2012 7th IEEE Conference on Industrial Electronics and Applications (ICIEA)*, 2012, no. 2, pp. 942–947.

[42] Q. C. Zhong and P. L. Nguyen, "Sinusoid-locked loops based on the principles of synchronous machines," *Proc. 2012 24th Chinese Control Decis. Conf. CCDC 2012*, pp. 1518–1523, 2012.

[43] E. Brown and G. Weiss, "Using synchronverters for power grid stabilization," *2014*

IEEE 28th Conv. Electr. Electron. Eng. Isr. IEEEI 2014, 2014.

[44] Jin-Song Meng *et al.*, "An Improved Synchronverter Model and its Dynamic Behaviour Comparison with Synchronous Generator," *2nd IET Renew. Power Gener. Conf. (RPG 2013)*, pp. 4.13-4.13, 2013.

[45] R. Aouini, K. B. Kilani, B. Marinescu, and M. Elleuch, "Virtual Synchronous Generators dynamic performances," *2014 Int. Conf. Electr. Sci. Technol. Maghreb*, pp. 1–6, 2015.

[46] Q. Zhong, S. Member, P. Nguyen, Z. Ma, and W. Sheng, "Self-Synchronized Synchronverters : Inverters Without a Dedicated Synchronization Unit," vol. 29, no. 2, pp. 617–630, 2014.

[47] V. Natarajan and G. Weiss, "Synchronverters with Better Stability Due to Virtual Inductors, Virtual Capacitors, and Anti-Windup," *IEEE Trans. Ind. Electron.*, vol. 64, no. 7, pp. 5994–6004, 2017.

[48] S. Dong and Y. C. Chen, "Adjusting Synchronverter Dynamic Response Speed via Damping Correction Loop," *IEEE Trans. Energy Convers.*, vol. 32, no. 2, pp. 608–619, 2017.

[49] L. Zhang, L. Harnefors, and H. P. Nee, "Power-synchronization control of grid-connected voltage-source converters," *IEEE Trans. Power Syst.*, vol. 25, no. 2, pp. 809–820, May 2010.

[50] L. Zhang, H.-P. Nee, and L. Harnefors, "Analysis of Stability Limitations of a VSC-HVDC Link Using Power-Synchronization Control," *IEEE Trans. Power Syst.*, vol. 26, no. 3, pp. 1326–1337, Aug. 2011.

[51] K. M. Alawasa and Y. A.-R. I. Mohamed, "Impedance and Damping Characteristics of Grid-Connected VSCs With Power Synchronization Control Strategy," *IEEE Trans. Power Syst.*, vol. 30, no. 2, pp. 952–961, Mar. 2015.

[52] S. D'Arco, J. A. Suul, and O. B. Fosso, "Control system tuning and stability analysis of Virtual Synchronous Machines," *2013 IEEE Energy Convers. Congr. Expo. ECCE 2013*, pp. 2664–2671, 2013.

[53] S. D'Arco, J. A. Suul, and O. B. Fosso, "Small-signal modelling and parametric sensitivity of a Virtual Synchronous Machine," in *2014 Power Systems Computation Conference*, 2014, pp. 1–9.

[54] S. D'Arco, J. A. Suul, and O. B. Fosso, "A Virtual Synchronous Machine implementation for distributed control of power converters in SmartGrids," *Electr. Power Syst. Res.*, vol. 122, pp. 180–197, May 2015.

[55] P. Rodriguez and J. I. C. G. R. Remus, "Synchronous power controller for a generating system based on static power converters," vol. 2, no. 12, 2015.

[56] P. Rodriguez, I. Candela, and A. Luna, "Control of PV generation systems using the synchronous power controller," in *2013 IEEE Energy Conversion Congress and Exposition*, 2013, pp. 993–998.

[57] W. Zhang, A. Tarraso, J. Rocabert, A. Luna, J. I. Candela, and P. Rodriguez,

"Frequency Support Properties of the Synchronous Power Control for Grid-Connected Converters," *IEEE Trans. Ind. Appl.*, vol. 55, no. 5, pp. 5178–5189, Sep. 2019.

[58] W. Zhang, "PhD Thesis Control of Grid Connected Power Converters with Grid Support Functionalities Weiyi Zhang."

[59] A. Tarrasó, J. I. Candela, J. Rocabert, and P. Rodriguez, "Grid voltage harmonic damping method for SPC based power converters with multiple virtual admittance control," *2017 IEEE Energy Convers. Congr. Expo. ECCE 2017*, vol. 2017-Janua, pp. 64–68, 2017.

[60] D. Remon, A. M. Cantarellas, J. D. Nieto, Weiyi Zhang, and P. Rodriguez, "Aggregated model of a distributed PV plant using the synchronous power controller," in *2015 IEEE 24th International Symposium on Industrial Electronics (ISIE)*, 2015, pp. 654–659.

[61] E. Rakhshani, D. Remon, A. M. Cantarellas, J. M. Garcia, and P. Rodriguez, "Virtual Synchronous Power Strategy for Multiple HVDC Interconnections of Multi-Area AGC Power Systems," *IEEE Trans. Power Syst.*, vol. 32, no. 3, pp. 1665–1677, May 2017.

[62] C. Verdugo, J. I. Candela, and P. Rodriguez, "Grid support functionalities based on modular multilevel converters with synchronous power control," in *2016 IEEE International Conference on Renewable Energy Research and Applications (ICRERA)*, 2016, pp. 572–577.

[63] A. M. Bouzid, J. M. Guerrero, A. Cheriti, M. Bouhamida, P. Sicard, and M. Benghanem, "A survey on control of electric power distributed generation systems for microgrid applications," *Renew. Sustain. Energy Rev.*, vol. 44, pp. 751–766, Apr. 2015.

[64] Y. Deng, Y. Tao, G. Chen, G. Li, and X. He, "Enhanced Power Flow Control for Grid-Connected Droop-Controlled Inverters With Improved Stability," *IEEE Trans. Ind. Electron.*, vol. 64, no. 7, pp. 5919–5929, Jul. 2017.

[65] J. C. Vasquez, J. M. Guerrero, M. Savaghebi, J. Eloy-Garcia, and R. Teodorescu, "Modeling, Analysis, and Design of Stationary-Reference-Frame Droop-Controlled Parallel Three-Phase Voltage Source Inverters," *IEEE Trans. Ind. Electron.*, vol. 60, no. 4, pp. 1271–1280, Apr. 2013.

[66] J. Dannehl, F. W. Fuchs, and P. B. Thogersen, "PI State Space Current Control of Grid-Connected PWM Converters With LCL Filters," *IEEE Trans. Power Electron.*, vol. 25, no. 9, pp. 2320–2330, Sep. 2010.

[67] J. R. Massing, M. Stefanello, H. A. Grundling, and H. Pinheiro, "Adaptive Current Control for Grid-Connected Converters With LCL Filter," *IEEE Trans. Ind. Electron.*, vol. 59, no. 12, pp. 4681–4693, Dec. 2012.

[68] K. H. Ahmed, A. M. Massoud, S. J. Finney, and B. W. Williams, "A modified stationary reference frame-based predictive current control with zero steady-state error for LCL coupled inverter-based distributed generation systems," *IEEE Trans. Ind. Electron.*, vol. 58, no. 4, pp. 1359–1370, Apr. 2011.

[69] J. Dannehl, M. Liserre, and F. W. Fuchs, “Filter-based active damping of voltage source converters with LCL filter,” *IEEE Trans. Ind. Electron.*, vol. 58, no. 8, pp. 3623–3633, Aug. 2011.

[70] W. Yao, Y. Yang, X. Zhang, F. Blaabjerg, and P. C. Loh, “Design and Analysis of Robust Active Damping for LCL Filters Using Digital Notch Filters,” *IEEE Trans. Power Electron.*, vol. 32, no. 3, pp. 2360–2375, Mar. 2017.

[71] L. A. Maccari *et al.*, “LMI-Based Control for Grid-Connected Converters With LCL Filters Under Uncertain Parameters,” *IEEE Trans. Power Electron.*, vol. 29, no. 7, pp. 3776–3785, Jul. 2014.

[72] N. Panten, N. Hoffmann, and F. W. Fuchs, “Finite Control Set Model Predictive Current Control for Grid-Connected Voltage-Source Converters with LCL Filters: A Study Based on Different State Feedbacks,” *IEEE Trans. Power Electron.*, vol. 31, no. 7, pp. 5189–5200, Jul. 2016.

[73] I. J. Gabe, V. F. Montagner, and H. Pinheiro, “Design and implementation of a robust current controller for VSI connected to the grid through an LCL filter,” *IEEE Trans. Power Electron.*, vol. 24, no. 6, pp. 1444–1452, Jun. 2009.

[74] M. S. Sadabadi, A. Haddadi, H. Karimi, and A. Karimi, “A Robust Active Damping Control Strategy for an LCL-based Grid-connected DG Unit,” *IEEE Trans. Ind. Electron.*, vol. 64, no. 10, pp. 1–1, Oct. 2017.

[75] D. Perez-Estevez, J. Doval-Gandoy, A. G. Yepes, and O. Lopez, “Positive-and Negative-Sequence Current Controller with Direct Discrete-Time Pole Placement for Grid-Tied Converters with LCL Filter,” *IEEE Trans. Power Electron.*, vol. 32, no. 9, pp. 7207–7221, Sep. 2017.

[76] J. Scoltock, T. Geyer, and U. K. Madawala, “A Model Predictive Direct Current Control Strategy With Predictive References for MV Grid-Connected Converters With LCL-filters,” *IEEE Trans. Power Electron.*, vol. 30, no. 10, pp. 5926–5937, Oct. 2015.

[77] V. Miskovic, V. Blasko, T. M. Jahns, A. H. C. Smith, and C. Romenesko, “Observer-based active damping of LCL resonance in grid-connected voltage source converters,” *IEEE Trans. Ind. Appl.*, vol. 50, no. 6, pp. 3977–3985, Nov. 2014.

[78] R. Guzman, L. G. de Vicuna, M. Castilla, J. tomas Miret, and J. de la Hoz, “Variable Structure Control for Three-Phase LCL-Filtered Inverters using a Reduced Converter Model,” *IEEE Trans. Ind. Electron.*, pp. 1–1, 2017.

[79] Y. a-R. I. Mohamed, M. A-Rahman, and R. Seethapathy, “Robust Line-Voltage Sensorless Control and Synchronization of LCL -Filtered Distributed Generation Inverters for High Power Quality Grid Connection,” *IEEE Trans. Power Electron.*, vol. 27, no. 1, pp. 87–98, Jan. 2012.

[80] S. G. Jorge, J. A. Solsona, and C. A. Busada, “Control scheme for a single-phase grid-tied voltage source converter with reduced number of sensors,” *IEEE Trans. Power Electron.*, vol. 29, no. 7, pp. 3758–3765, 2014.

[81] B. Wang, Y. Xu, Z. Shen, J. Zou, C. Li, and H. Liu, "Current Control of Grid-Connected Inverter With LCL Filter Based on Extended-State Observer Estimations Using Single Sensor and Achieving Improved Robust Observation Dynamics," *IEEE Trans. Ind. Electron.*, vol. 64, no. 7, pp. 5428–5439, Jul. 2017.

[82] R. A. Fantino, C. A. Busada, and J. A. Solsona, "Observer-Based Grid-Voltage Sensorless Synchronization and Control of a VSI-LCL Tied to an Unbalanced Grid," *IEEE Trans. Ind. Electron.*, vol. 66, no. 7, pp. 4972–4981, Jul. 2019.

[83] N. F. Roslan, J. A. Suul, J. Rocabert, and P. Rodriguez, "A Comparative Study of Methods for Estimating Virtual Flux at the Point of Common Coupling in Grid-Connected Voltage Source Converters With LCL Filter," *IEEE Trans. Ind. Appl.*, vol. 53, no. 6, pp. 5795–5809, Nov. 2017.

[84] C. Johnson, "Accomodation of external disturbances in linear regulator and servomechanism problems," *IEEE Trans. Automat. Contr.*, vol. 16, no. 6, pp. 635–644, Dec. 1971.

[85] J. CHEN, R. J. PATTON, and H.-Y. ZHANG, "Design of unknown input observers and robust fault detection filters," *Int. J. Control*, vol. 63, no. 1, pp. 85–105, Jan. 1996.

[86] W.-H. Chen, J. Yang, L. Guo, and S. Li, "Disturbance-Observer-Based Control and Related Methods—An Overview," *IEEE Trans. Ind. Electron.*, vol. 63, no. 2, pp. 1083–1095, Feb. 2016.

[87] G. F. Franklin, J. D. Powell, and M. L. Workman, "Digital control of dynamic systems," p. 837, 1990.

[88] M. C. de Oliveira, J. Bernussou, and J. C. Geromel, "A new discrete-time robust stability condition," *Syst. Control Lett.*, vol. 37, no. 4, pp. 261–265, Jul. 1999.

[89] S. Golestan, J. M. Guerrero, and A. Abusorrah, "MAF-PLL With Phase-Lead Compensator," *IEEE Trans. Ind. Electron.*, vol. 62, no. 6, pp. 1–1, 2014.

[90] International Electrotechnical Commission, "IEC 61784-2:2014 Industrial communication networks - Profiles - Part 2: Additional fieldbus profiles for real-time networks based on ISO/IEC 8802-3," 2014.

[91] B. Ciftci, S. Schiessl, J. Gross, L. Harnefors, S. Norrga, and H. P. Nee, "Wireless Control of Modular Multilevel Converter Submodules," *IEEE Trans. Power Electron.*, vol. 36, no. 7, pp. 8439–8453, 2021.

[92] P. Kundur, *Power system stability and control*. New York: McGraw-Hill, 1994.

[93] J. Fang, H. Li, Y. Tang, and F. Blaabjerg, "Distributed Power System Virtual Inertia Implemented by Grid-Connected Power Converters," *IEEE Trans. Power Electron.*, vol. 33, no. 10, pp. 8488–8499, 2018.

[94] K. E. N. M. Erik Ørum, Mikko Kuivaniemi, Minna Laasonen, Alf Ivar Bruseth Erik Alexander Jansson, Anders Danell, "Nordic Report: Future System Inertia," 2018.

[95] E. Ørum *et al.*, "Future system inertia 2," 2018.

[96] P. Kundur, *Power System Stability and Control*. McGraw-Hill Education, 1994.

[97] S. K. Chung, "A phase tracking system for three phase utility interface inverters," *IEEE Trans. Power Electron.*, vol. 15, no. 3, pp. 431–438, May 2000.

[98] G. Rogers, *Power System Oscillations*. Boston, MA: Springer US, 2000.

[99] J. Paserba, J. Sanchez-Gasca, L. Wang, P. Kundur, E. Larsen, and C. Concordia, "Small-Signal Stability and Power System Oscillations," 2012, pp. 1–24.

[100] K. Prasertwong, N. Mithulananthan, and D. Thakur, "Understanding Low-Frequency Oscillation in Power Systems," *Int. J. Electr. Eng. Educ.*, vol. 47, no. 3, pp. 248–262, Jul. 2010.

[101] I. Dobson *et al.*, "Electric Power Transfer Capability: Concepts, Applications, Sensitivity, Uncertainty," New York, 2001.

[102] Z. Assi Obaid, L. M. Cipcigan, and M. T. Muhssin, "Power system oscillations and control: Classifications and PSSs' design methods: A review," *Renew. Sustain. Energy Rev.*, vol. 79, pp. 839–849, Nov. 2017.

[103] PES, "IEEE Recommended Practice for Excitation System Models for Power System Stability Studies," *IEEE Std 421.5-2005 (Revision IEEE Std 421.5-1992)*, vol. 2005, no. April, pp. 0_1-85, 2006.

[104] F. Rashidi and M. Rashidi, "Robust and Adaptive Tuning of Power System Stabilizers Using Artificial Neural Networks," in *Innovations in Applied Artificial Intelligence*, B. Orchard, C. Yang, and M. Ali, Eds. Berlin, Heidelberg: Springer Berlin Heidelberg, 2004, pp. 1023–1032.

[105] J. Fang, H. Li, Y. Tang, and F. Blaabjerg, "On the Inertia of Future More-Electronics Power Systems," *IEEE J. Emerg. Sel. Top. Power Electron.*, vol. 7, no. 4, pp. 2130–2146, 2019.

[106] G. Cao, Z. Y. Dong, Y. Wang, P. Zhang, and Y. T. Oh, "VSC based STATCOM controller for damping multi-mode oscillations," in *2008 IEEE Power and Energy Society General Meeting - Conversion and Delivery of Electrical Energy in the 21st Century*, 2008, pp. 1–8.

[107] K. M. Son and J. K. Park, "On the robust LQG control of TCSC for damping power system oscillations," *IEEE Trans. Power Syst.*, vol. 15, no. 4, pp. 1306–1312, 2000.

[108] G. S. Chawda, A. G. Shaik, O. P. Mahela, S. Padmanaban, and J. B. Holm-Nielsen, "Comprehensive Review of Distributed FACTS Control Algorithms for Power Quality Enhancement in Utility Grid With Renewable Energy Penetration," *IEEE Access*, vol. 8, pp. 107614–107634, 2020.

[109] F. H. Gandoman *et al.*, "Review of FACTS technologies and applications for power quality in smart grids with renewable energy systems," *Renew. Sustain. Energy Rev.*, vol. 82, pp. 502–514, Feb. 2018.

[110] X. Sui, Y. Tang, H. He, and J. Wen, "Energy-Storage-Based Low-Frequency Oscillation Damping Control Using Particle Swarm Optimization and Heuristic Dynamic Programming," *IEEE Trans. Power Syst.*, vol. 29, no. 5, pp. 2539–2548,

Sep. 2014.

[111] M. Li, L. Xiong, H. Chai, L. Xiu, and J. Hao, "Mechanism of PV Generation System Damping Electromechanical Oscillations," *IEEE Access*, vol. 8, pp. 135853–135865, 2020.

[112] N. B. Lai, K.-H. Kim, and P. Rodriguez, "Voltage Sensorless Control Scheme Based on Extended-State Estimator for a Grid-Connected Inverter," *IEEE Trans. Power Electron.*, vol. 35, no. 6, pp. 5873–5882, Jun. 2020.

[113] N. B. Lai, A. Tarraso, G. N. Baltas, L. Marin, and P. Rodriguez, "Inertia Emulation in Power Converters with Communication Delays," in *2020 IEEE Energy Conversion Congress and Exposition (ECCE)*, 2020, pp. 1665–1669.

[114] R. Rosso, X. Wang, M. Liserre, X. Lu, and S. Engelken, "Grid-Forming Converters: Control Approaches, Grid-Synchronization, and Future Trends—A Review," *IEEE Open J. Ind. Appl.*, vol. 2, pp. 93–109, 2021.

[115] A. Tayyebi, F. Dörfler, F. Kupzog, Z. Miletic, and W. Hribernik, "Grid-Forming Converters – Inevitability, Control Strategies and Challenges in Future Grids Application," *CIRED Work. 2018*, no. 0236, pp. 1–5, 2018.

[116] W. Zhang, "Control of grid connected power converters with grid support functionalities," Universitat Politècnica de Catalunya, 2017.

[117] G. N. Baltas, N. B. Lai, L. Marin, A. Tarraso, and P. Rodriguez, "Grid-Forming Power Converters Tuned Through Artificial Intelligence to Damp Subsynchronous Interactions in Electrical Grids," *IEEE Access*, vol. 8, pp. 93369–93379, 2020.

[118] G. N. Baltas, N. B. Lai, A. Tarraso, L. Marin, F. Blaabjerg, and P. Rodriguez, "AI-Based Damping of Electromechanical Oscillations by Using Grid-Connected Converter," *Front. Energy Res.*, vol. 9, Mar. 2021.

[119] "IEEE Standard for Interconnecting Distributed Resources with Electric Power Systems," *IEEE Std 1547-2003*, pp. 1–28, 2003.

[120] E. O. Netz, "REQUIREMENTS FOR OFFSHORE GRID CONNECTIONS IN THE E.ON NETZ NETWORK," 2008.

[121] P. Rodriguez, C. Citro, J. I. Candela, J. Rocabert, and A. Luna, "Flexible Grid Connection and Islanding of SPC-Based PV Power Converters," *IEEE Trans. Ind. Appl.*, vol. 54, no. 3, pp. 2690–2702, 2018.

[122] N. J. Kundur, P. and Balu, *Power System Stability and Control*. McGraw-Hill, 1994.

[123] M. Beza and M. Bongiorno, "An Adaptive Power Oscillation Damping Controller by STATCOM With Energy Storage," *IEEE Trans. Power Syst.*, vol. 30, no. 1, pp. 484–493, Jan. 2015.

[124] G. N. Baltas, N. B. Lai, A. Tarraso, L. Marin, F. Blaabjerg, and P. Rodriguez, "AI-Based Damping of Electromechanical Oscillations by Using Grid-Connected Converter," *Front. Energy Res.*, vol. 9, Mar. 2021.

[125] M. Klein, G. J. Rogers, and P. Kundur, "A fundamental study of inter-area

oscillations in power systems," *IEEE Trans. Power Syst.*, vol. 6, no. 3, pp. 914–921, 1991.

[126] C. Canizares *et al.*, "Benchmark Models for the Analysis and Control of Small-Signal Oscillatory Dynamics in Power Systems," *IEEE Trans. Power Syst.*, vol. 32, no. 1, pp. 715–722, Jan. 2017.

[127] S. Mendoza-Armenta and I. Dobson, "Applying a Formula for Generator Redispatch to Damp Interarea Oscillations Using Synchrophasors," *IEEE Trans. Power Syst.*, vol. 31, no. 4, pp. 3119–3128, Jul. 2016.